Technische Universität München
TUM School of Natural Sciences

Alpha particle driven Alfvénic instabilities in ITER post-disruption plasmas and their impact on runaway electron generation

Andrej Lier

Vollständiger Abdruck der von der TUM School of Natural Sciences der Technischen Universität München zur Erlangung des akademischen Grades eines

Doktors der Naturwissenschaften (Dr.rer.nat.)

genehmigten Dissertation.

Vorsitz:
Prof. Christine Papadakis, Ph.D.

Prüfer*innen der Dissertation:
1. Hon.-Prof. Dr. Sibylle Günter
2. Prof. Dr. Carlos Paz-Soldan

Die Dissertation wurde am 17.01.2023 bei der Technischen Universität München eingereicht und durch die TUM School of Natural Sciences am 04.04.2023 angenommen.

MAX-PLANCK-INSTITUT
FÜR PLASMAPHYSIK

PhD Thesis

Alpha particle driven Alfvénic instabilities in ITER post-disruption plasmas and their impact on runaway electron generation

Andrej Lier
`andrej.lier@ipp.mpg.de`

Erstbetreuer: Prof. Sibylle Günter
Zweitbetreuer: Dr. Gergely Papp

Acknowledgements

I would like to offer special thanks to my thesis mentors Gergely Papp and Philipp Lauber, who took responsibility for me and guided me through many years of hard work. They were always available and helpful when I ran into trouble and pushed me in the directions necessary. The thesis project began as their brainchild and remains interesting and challenging until this day. Also, I would like to thank Sibylle Günter for taking the time to supervise my thesis and the IPP for providing the opportunity of conducting the research.

In the end, this work would not have been possible without the numerical tools, which Konsta Särkimäki, István Pusztai, George Wilkie, Ola Embreus and Thomas Hayward-Schneider introduced me to and/or helped me understand. I am thankful to discussions with Eric Nardon, Oliver Linder, Matthias Hoelzl and Chang Liu which helped to continue my work in a meaningful direction. The same holds true for the IPP-MHD group for providing valuable feedback during rehearsals.

Having visited PPPL, my gratitude goes to Amitava Bhattacharjee for hosting the summer school, as well as Todd Elder for enriching my stay there. My travels to the Chalmers University would not have been possible without Tünde Fülöp and certainly less fun without Ola Embreus, Matthias Hoppe and Boel Brandström. Sometimes, my sanity has been only been kept up by colleagues and office mates, especially Florian Holderied, Rohan Ramasamy, Farah Atour, Verena Mitterauer, Mario Räth, Tobias Blickhahn, Thomas Hayward-Schneider and Nina Schwarz.

Contents

1 Introduction

In search of a sustainable energy source, *nuclear fusion* is under research. With the goal to control thermo-nuclear fusion and eventually provide electric energy output, the *tokamak* concept was invented in the 1950s in the Soviet Union [1] and culminates today in an international project - ITER [2] - whose machine assembly began in 2020 [3]. While this experiment is multifaceted and placed under the umbrella term "fusion research", the most fundamental understanding originates from *plasma physics*, as the fusing material is in a plasma state of matter. The challenge in fusion research is to achieve controllable, stable and economically viable operation.

As the ITER tokamak approaches first operation, the concern about a specific plasma physics phenomenon, the *runaway electron* (RE) generation, grows [4, 5]. RE generation naturally accompanies *plasma disruptions* [6], which - though sought to be avoided [7] - cannot be ruled out and *disruption mitigation systems* [8] must be integrated as a safety net. Most recent theoretical analysis suggests [9, 10], that a disruptive nuclear phase ITER plasma may generate a RE beam that cannot confidently be mitigated at current development status and bears existential risks to the device [11, 12].

The work in this thesis investigates an inherent physical mechanism, where plasma waves interact with the REs and could aid RE mitigation efforts. For this mechanism to be understood, we begin by laying out the relevant concepts of tokamaks and plasma physics.

The aspired nuclear reaction fuses the hydrogen isotopes deuterium (D) and tritium (T)

$$\mathrm{D} + \mathrm{T} \rightarrow \alpha(3.5\,\mathrm{MeV}) + \mathrm{n}(14.1\,\mathrm{MeV}),$$

distributing about 17.6 MeV of energy to a doubly charged alpha particle (α^{2+}) and a neutron. The fusion reaction takes place in an environment of low particle density ($\sim 10^{20}\,\mathrm{m}^{-3}$) and high temperature ($\sim 10^{8}\,\mathrm{K} \sim 10^{4}\,\mathrm{eV}$), where thermal motion leads to a large enough cross section for the fusion collision to happen. At temperatures that high, electrons become detached from the nucleus, creating a *plasma* with an electrically conductive property.

It is this property, that allows the fuel D-T plasma and the alpha particle to be confined within the magnetic fields generated by a tokamak (see figure 1.1), while the neutron leaves the plasma without interaction. Field coils generate an axisymmetric magnetic "cage" within a vacuum chamber, shaped to a torus. The center of the torus is referred to as *magnetic axis*, the long way around the torus is called *toroidal* direction and the short way around is the *poloidal* direction. Characteristic for a tokamak is the central transformer coil, which induces a toroidal *plasma current* and superimposes the toroidal magnetic field (from the toroidal field coils) with a poloidal component. This results in helical magnetic field lines, twisted around the magnetic axis. The field confines the charged plasma particles via the Lorentz force onto their own, infinitely looping trajectory and prevent them from hitting the chamber walls. The good confining properties of a tokamak is what allows a prolonged existence of the hot plasma in the first place, and is also what will allow future tokamaks to absorb the alpha particle energy and utilize it as an internal heating. For technical and economical reasons, present-day

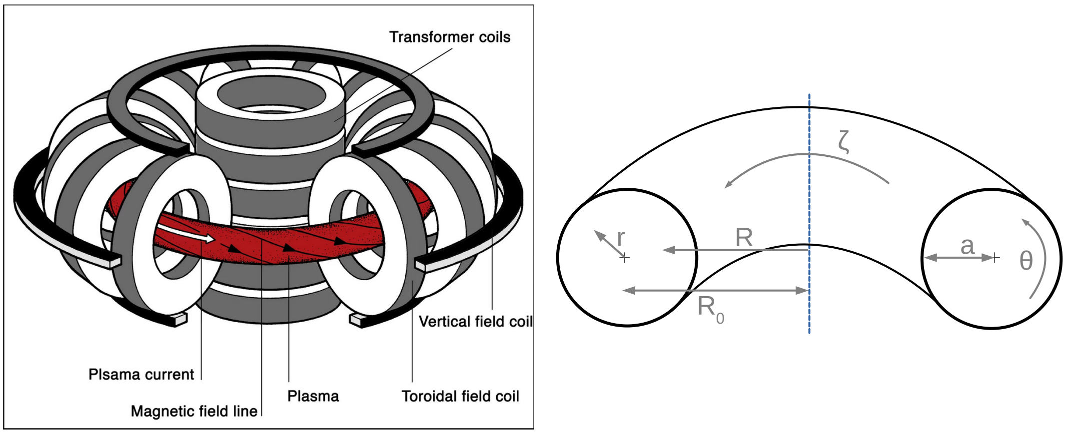

Figure 1.1: LHS: Schematic drawing of a tokamak [15]. RHS: Toroidal geometry definitions: poloidal angle (θ), toroidal angle (ζ), radius from magnetic axis (r) and radius from central axis (blue dashed line) R. The *major radius* R_0 and the *minor radius* a relate the device and plasma dimensions to magnetic axis (center of the torus).

tokamaks mostly use pure deuterium fuel (where fusion reactions are rare) as challenges of non-nuclear phase plasmas are already plenty. The occasional dedicated experiments (e.g. in JET [13] or TFTR [14]) however show that the plasma physics basics of alpha particles are well understood.

Two additional aspects about the tokamak are important to note here: The plasma current is induced by ramping up a current through the transformer coil, which cannot be done indefinitely. Tokamak operation is therefore naturally pulsed, with the pulses (of plasma) often being referred to as *discharges* or *shots*, which on current-day machines usually last a duration of the order of seconds. The plasma current is driven by the *loop voltage* and is - due to the high conductivity of a plasma - comparatively low ($\sim$ V) during normal operation. Secondly, the toroidal magnetic field strength decreases radially as $B \sim 1/R$ (distance R from central axis) and creates regions usually referred to as *high-field side* (HFS - inwards) and *low-field side* (LFS - outwards). On the other hand, the poloidal magnetic field component is a function of the current profile. The resulting twist of a field line is characterized by the so-called *safety factor* q, which counts the number of toroidal transits for every poloidal transit. The name comes from a necessity to maintain $q \gtrsim 1$ in the plasma center and $q \gtrsim 3$ at the plasma edge, in order to prevent various plasma instabilities [1, 16–18].

From the axisymmetry of the torus it can be shown [1], that following a magnetic field line will eventually map out a magnetic surface. The plasma of a tokamak is therefore often understood as consisting of radially nested *flux surfaces*. In a simplified picture, the plasma can be thought of as “frozen” onto the magnetic field $\mathbf{B}$. A static magnetic equilibrium requires force balance between confining electromagnetic forces and expanding pressure: $\mathbf{j} \times \mathbf{B} = -\nabla p$, for a current $\mathbf{j}$ and a pressure p. It follows that (1) $\mathbf{B} \times \nabla p = 0$ and (2) $\mathbf{j} \times \nabla p = 0$, meaning that (1) field lines of $\mathbf{B}$ lie on surfaces of constant pressure and (2) current lines lie on said surfaces as well. Because of such constants along flux surfaces, they can be labelled and used to describe a plasma equilibrium. Often the toroidal flux Ψ, i.e. the magnetic flux going through the poloidal cross-section of a flux surface, is used as a radial coordinate (we will often use the normalized toroidal flux $0 \leq \psi \leq 1$, where $\psi = r^2$ for a circular torus). Another example is the safety factor, which is constant along flux surfaces and the profile of which, $q(\psi)$, is often used to describe a plasma equilibrium.

The equilibrium state may be subject to perturbations in the form of plasma waves, which can be excited through interaction with *energetic particles* (EPs). The aforementioned alpha particles of the *burning*, nuclear phase plasma constitute such a population [19]. It is energetically distinct from the thermal fuel population and resides mostly in the core of the plasma, close to the magnetic axis [19]. With alpha velocities comparable to the phase velocity of a specific type of plasma modes, the *Toroidal Alfvén Eigenmode* [20] (TAE), *resonance interaction* can occur which drives the TAE unstable and develops an Alfvénic plasma wave (discussed in more detail in chapter 2).

Particle trajectories in the tokamak are not perfectly bound to the magnetic field lines and perform various kinds of periodic *orbits* [1]. If the resonance condition has to be fulfilled with the orbital motion, it is sometimes better understood in the frequency space than in velocity space. Because of the generally strong magnetic fields ($\sim$ T), the gyro-frequency $\omega_g \propto |\mathbf{B}|$ ($\sim 10^8\,\mathrm{s}^{-1}$ for ions) lies well beyond the eigenfrequency of the TAE (typically $\omega_{\mathrm{TAE}} \sim 10^6\,\mathrm{s}^{-1}$) and can be ignored.

Due to the periodicity of the tokamak, the particles perform periodic motion in poloidal and toroidal direction. A type of orbit emerges from the variation of magnetic field strengths along a particle's poloidal path, together with the adiabatic invariance of the particle magnetic moment μ:

$$\mu = \frac{mv_\perp^2}{2B}$$

where m is the particle mass, $v_\perp$ is its velocity perpendicular to the magnetic field line and $B = |\mathbf{B}|$ is the magnetic field strength. As the particle is subject to varying B along its trajectory, the conservation of energy, $E = (mv_\parallel^2)/2 + \mu B$, compensates changes to $v_\perp$ by changing the parallel velocity $v_\parallel$. If the variation in B is strong enough (relative to the initial $v_\parallel/v_\perp$), the parallel motion is reversed, or mirrored at the HFS of the tokamak. This *magnetic mirror* effect causes some particles to become *trapped* in a section of their poloidal orbit. Particles transiting the entire poloidal path are considered *passing*. While the orbit frequency differs for trapped and passing particles, it is here commonly denoted as ω_θ.

In addition to the gyro-motion, particle trajectories deviate from the magnetic field lines due to *particle drifts*, which for a general force $\mathbf{F}$ can be described by

$$\mathbf{v}_d = \frac{\mathbf{F} \times \mathbf{B}}{qB^2},$$

where $\mathbf{v}_d$ is the drift velocity and q is the particle charge. Important drifts include curvature drift and ∇B-drift, which due to the curvature and non-uniform magnetic field of the torus are ubiquitous in a tokamak. The axisymmetry of the system ensures that drifts outwards and inwards are compensated, but the particles now move along *drift-surfaces* that deviate from the magnetic surfaces. The excursion from the surfaces due to particle drifts exceeds the excursion due to the gyro-motion. Along its motion on drift-surfaces, the particle drifts to neighbouring magnetic field lines, causing a precession motion in toroidal direction with a frequency ω_{prec}.

Should either of the frequencies ω_θ or ω_{prec} match the eigenfrequency of the TAE, resonant interaction occurs by which energy is exchanged between the mode and the particles. In the case of TAEs, alpha particles generally drive the mode and increase its amplitude by which it perturbs the equilibrium. In that sense, alphas are usually in competition with the thermal ions, which draw energy away from the mode in a process called *ion Landau damping* [21]. Here, it is only the most energetic portion of the thermal ions, the Maxwellian tail, that resonates with the TAE.

During normal - *quiescent* - tokamak operation, perturbations that might grow into major instabilities are undesired. The envisioned alpha population for the ITER operation is predicted to be unable to overcome the damping of the thermal population in the quiescent phase [22]. In this work however, we aim to investigate the resonant α-TAE interaction not in the quiescent phase, but during so-called *disruptions* [6].

A disruption describes an abrupt, uncontrolled termination of a tokamak discharge, resulting in a release of its stored energy. The plasma temperature T drops by many orders of magnitude within a timescale of milliseconds. While the plasma cools, it becomes less conductive and the plasma current encounters a rising resistivity $\sigma \propto T^{-3/2}$ [1]. Self-inductive properties of the plasma induce a strong toroidal electric field in an attempt to maintain the pre-disruption plasma current.

The electric field exerts an acceleration force on charged particles and has to compete against the particle decelerating, collisional friction. Collisions in a plasma are due to Coulomb interactions, which bear a remarkable property for super-thermal particles: beyond a threshold, with rising speeds, the collisional momentum exchange decreases stronger than the increased number of collision encounters could balance out [23]. This phenomenon entails a friction force F_{C}, that decreases with the particle velocity, $F_{\mathrm{C}} \propto v^{-2}$ above a threshold v_{th}, which is the thermal velocity. Given an accelerating force that can overcome the initial friction in the first place, the super-thermal particle is sped up with increasing efficiency, it undergoes a *runaway.*

Following a tokamak disruption, the conditions are met for the induced electric field to generate a population of *runaway electrons* [24, 25] (REs). The REs form a directed beam of relativistic particles, carrying a significant portion of the initial plasma current, which could be multiple mega-amperes for ITER. This conversion occurs in post-disruption, where position control over the plasma becomes increasingly ineffective. As this beam bears the potential of damaging the device on impact [11] - esp. in a high-current device like ITER [12] - *runaway electron mitigation* is a field of active research [5, 8, 26]. *Massive Material Injection* [11, 27] (MMI) is a common method to increase the (non-localized) irradiation of plasma energy content and generally raise the friction F_{C}. Material injection however may not be sufficient in itself to solve the runaway problem [9, 10], hence additional methods are under consideration. One such idea revolves around applying magnetic perturbations to the plasma, thus diminishing its particle-confining property. Such mitigation systems mainly include *Resonant Magnetic Perturbations* [28, 29] (RMPs) and *passive helical coils* [30, 31] and will be discussed in section 2.2. Strong enough perturbations cause the magnetic field lines to behave chaotically and provoke radial transport of particles, to which the runaways are susceptible to because of their high velocity. RE transport is beneficial when it hinders the formation of the beam, but often unfavourable once the beam is fully developed.

While it is possible to apply RMPs externally, the success in causing RE losses varies [28, 29, 32]. A major obstacle was identified to be the limited penetration depth, because of which the (predominantly core-generated) REs are hard to reach [9, 33]. As it stands, these mitigation systems would benefit immensely from a plasma-inherent mechanism, that causes perturbations in the core of the plasma following disruption. Such a mechanism is studied in this work.

We consider the core-localized alpha particles of a nuclear phase ITER plasma and their behaviour in a disruption. As mentioned in the context of REs, the collisional friction of high-velocity particles is low compared to thermal particles. It will be shown, that this property allows the alphas to remain energetic for a several milliseconds into a disruption. Crucially, the alphas maintain their ability to resonantly drive TAEs. Meanwhile, the fast cooling thermal ion population loses its ability to damp the TAE. This process is a natural consequence of the disruption and provides a possibility of perturbations being driven unstable in the plasma core.

1.1 The concept of the post-disruption alpha particle drive

In this section, we provide a more detailed introduction to the novel mechanism that is under study in this thesis.

The general idea behind the project of this thesis can be motivated by multiple experimental observations on present-day tokamaks. An example [34] was found at the ASDEX-Upgrade tokamak [35, 36] (AUG). With a new experimental scenario established [37, 38], one of the goals was to research EP-driven plasma instabilities in a relatively cold plasma environment ($T \lesssim 1\,\mathrm{keV}$). The experimental data can be found in reference [39] and the scenario is further advanced in reference [40]. This unique scenario allows an accumulation of impurities in the deuterium plasma core, which keeps the temperature and pressure of the thermal population low due to strong impurity radiation. Simultaneously, neutral beam injection (NBI) systems are used to generate an additional, small population of EPs. Although the populations exchange energy via collisions, the scenario allowed both to coexist at distinct energy regions. The EP velocities are about 100 times larger than the thermal velocity, but the background pressure - because of its larger density - is comparable to the EP pressure [40]. These velocity and pressure ratios approach the theoretical predictions for future fusion devices like ITER, and gave access to previously experimentally unexplored parameter regimes [40].

During the experiment, a strong destabilization of a wide range of modes was observed [41, 42], including TAEs [43]. The physical reason is found to be the strongly temperature-dependent ion Landau damping of the thermal background plasma [44, 45], which fails to compete against the resonant EP drive, when the temperature T is sufficiently low. The collisional drag of the cold bulk plasma decelerates the EPs and reduces their ability to destabilize plasma waves. However, the reduction in damping is more severe as it is exponentially sensitive to the ion temperature [22, 46].

Although the experimental scenario described above was purposefully tailored for research, such plasma conditions can occur in regular tokamak operations. An energetic population and a cold bulk plasma can briefly coexist, when the plasma temperature drops suddenly and violently, like in a disruption. Modes occurring in post-disruption are routinely observed in present-day tokamaks [34, 47–50]. In figure 1.2 two such instances are shown for the AUG and the larger JET tokamak [51]. The frequency range in both cases is in the Alfvénic regime. Often the source of the mode drive is not obvious, as various kinds of energetic populations can be the origin and other destabilizing mechanisms exist. While a former analytical study on runaway ions [52] was inconclusive, it was later deduced [53] that runaway ions are unlikely as a driving population on the short timescales of a disruption ($\sim$ ms), through it was not ruled out during magnetic reconnection events [54]. A study [55] on the DIII-D tokamak [56] identified runaway electrons as the origin for the Compressional Alfvén Eigenmodes (or possibly Global Alfvén Eigenmodes) at much larger frequency.

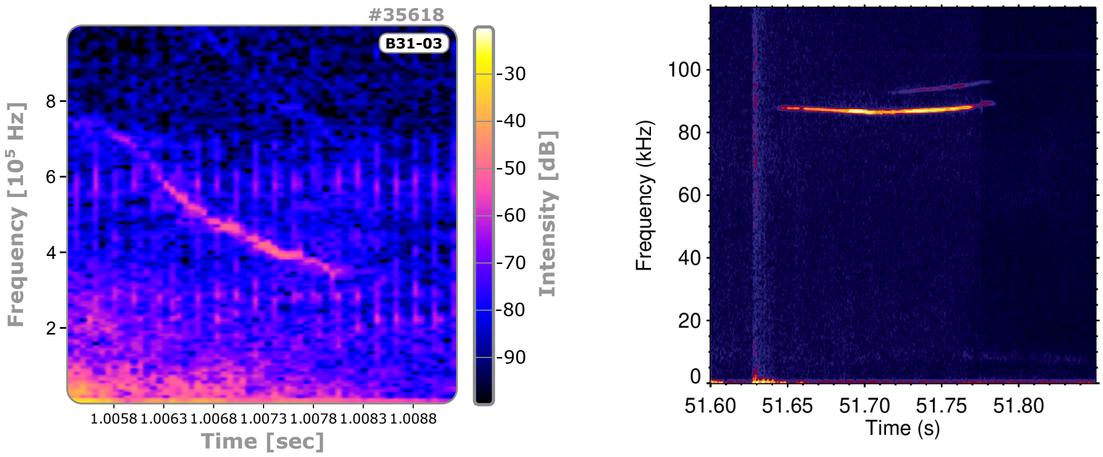

Figure 1.2: Two examples of post-disruption magnetic signals picked up by Mirnov coils in the (LHS) ASDEX Upgrade tokamak and (RHS) the JET tokamak (shot #89141). The disruption occurred at a) $\approx 1.005\,\mathrm{s}$ and b) $\approx 51.63\,\mathrm{s}$ respectively. These figures are provided courtesy of (LHS) P. Heinrich and (RHS) S. Newton, P. Pölöskei but are unpublished.

For our predictive study, energetic alpha particles born during the fusion process of a burning ITER plasma take the role of the mode-driving EPs. Theoretical analysis predicts [22, 57] the existence of marginally unstable TAEs already in the pre-disruption plasma conditions through resonances with the alpha particles and NBI-generated ions. With an ion Landau damping, which is exponentially sensitive to the temperature, we expect these modes to be destabilized shortly after a disruption.

The study focuses on TAEs and only the alpha particles, which have velocities higher than the NBI-generated ions and well above the (pre-disruption) Alfvén velocity (factor 1.8 higher). The qualitative course of events is sketched in figure 1.3. In the normally burning plasma ($T \approx 10-20\,\mathrm{keV}$) the damping is comparable to the alpha drive [22], but drops suddenly, when a disruptive event quenches the temperature of the plasma. The high alpha particle energy ($\sim$ MeV) will be shown to resist a thermalization with the cooling background for a significant amount of time ($\sim$ ms), even though the alpha production ceases. As the plasma cools down further and reaches temperatures of the order of tens of eVs, damping mechanisms of a cold plasma become significant. The question that must be answered, is whether the alpha particle drive is strong and enduring enough to destabilize TAEs in the weakly damped post-disruption plasma equilibrium.

Ultimately, the motivation behind this research is an attempt to find runaway electron mitigating effects. The interaction of runaways with plasma waves has been investigated in both theory [58–65] and through observations in multiple tokamaks [47, 48, 66–70]. Experiments at several tokamaks [71, 72] have observed a magnetic field strength B threshold, below which runaway electron formation is suppressed. While the physics behind the threshold is not certain, the suppressing effects have been correlated to increased levels of perturbation strengths $\delta B/B$ [73]. At the TEXTOR tokamak [74], the post-disruption presence of a TAE correlated with enhanced losses of runaway electrons [47]. The relative perturbation strength is higher when the magnetic field strength B in the plasma is low and has been connected [66] to the lack of REs in the plasma discharge. Other tokamaks, like COMPASS [75], have observed burst-like expulsion of runaways caused by large-scale MHD (*MagnetoHydroDynamic*, see section 2.3) instabilities [76]. Earlier studies showed, that magnetic perturbations with an amplitude of

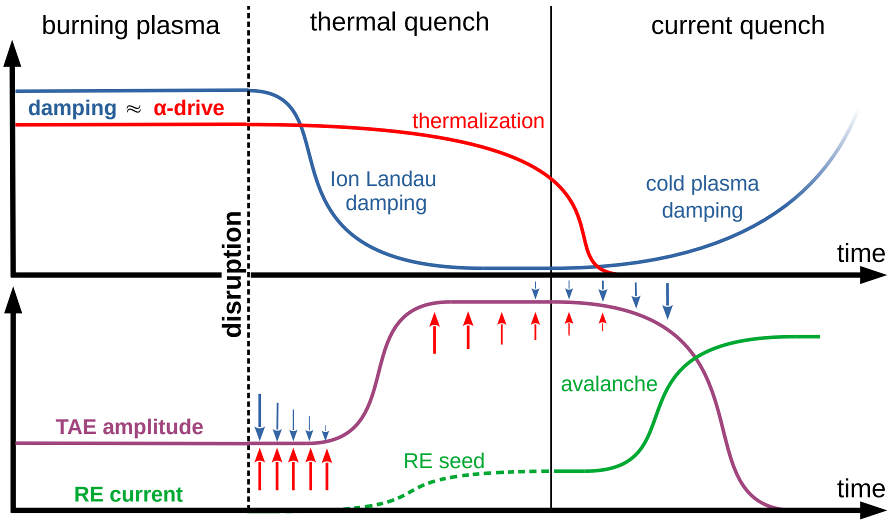

Figure 1.3: A qualitative sketch of the proposed alpha drive mechanism. The amplitude of a TAE is determined by a competition between damping and driving forces. The arrows indicate the strength of the driving force from the alpha distribution (red) and the damping from the background (blue). In a disrupting plasma, the damping temporarily loses against the alpha drive due to temperature-dependent Landau damping, and a slow thermalization of alpha particles. Ultimately, the interaction of the TAE with runaway electrons is of interest to this study. RE seeds are generated by primary mechanisms, and multiplied via avalanche, once the induced electric field arises. A reduction of the final RE current is the motivation behind this research.

about $\delta B/B \approx 0.1\%$ is sufficient to suppress runaway avalanche [33, 77], while more recent research [9] has halved this threshold.

As hypothesised in the concluding remarks of reference [45], alpha particles could serve as a drive for perturbations, that diminish the formation of a runaway electron beam. Importantly, this could provide a passive and inherent mitigation mechanism, that would aid the external mitigation systems, especially ones that rely on externally applied perturbations. The instability effects on particle confinement are especially relevant for REs, which - due to their high velocity - can be extremely susceptible to orbit losses.

1.2 Scope of the thesis

In order to study the feasibility of the mechanism shown in section 1.1, a self-consistent calculation of the alpha population, the plasma equilibrium, the wave-particle interactions and the runaway electron generation is necessary. The presence of alpha particles requires a burning plasma, which do not exist yet, but are eventually foreseen as ordinary operation in reactor-relevant tokamaks like ITER.

Chapter 2 will introduce the plasma and tokamak theory necessary for this thesis. Due to the complexity of the problem numerical tools will be applied throughout this project and are briefly outlined in chapter 3, with the required code development presented in chapter 4. In chapter 5 we study the main subject of this thesis in detail: Section 5.1 will introduce the ITER plasma scenario that is the basis of the calculations in this work.

The plasma suffers a disruption, which we model with a thermal quench and reconstruct a plasma equilibrium for this phase. The equilibrium is investigated about its TAEs and the bulk plasma damping. Section 5.2 deals with the collisional dynamics of alpha particles, during which we also derive an analytical model. In section 5.3, plasma equilibrium, alpha particles and TAEs come together in wave-particle interaction simulations, where we also use a model to account for disruption-induced alpha particle transport. These simulations yield the alpha-driven perturbation amplitudes one can expect during the thermal quench of the ITER plasma. In the final section 5.4 we will perform disruption simulations, that account for the calculated perturbations in the thermal quench, and compute its influence on runaway electron generation. The results are summerized in chapter 6.

The research conducted throughout this project and presented in this thesis is published in paper A [78] and (submitted) in paper B [79]. Paper A is a proof-of-principle study on the mechanism presented in the previous section. We found significant perturbations driven by the alphas in an unmitigated disruption and indications that these perturbations may cause RE transport. This led to the more thorough and elaborate investigation in the follow-up study in paper B. Improvements include the consideration of mitigated disruption, a model for alpha particle transport, RE electron transport calculations and a self-consistent disruption simulation with the included RE transport. The methods of paper A (see e.g. code development section 4) were chosen for a proof-of principle study, however improved/replaced for the follow-up study, and therefore put in the forefront of this thesis. This paints a more complete picture of the physical process and provides less distraction involving technicalities. A vast majority of the work presented in paper A and B was done by myself. Some code applications and derivations were done by co-authors and will be clearly stated in this thesis.

2 Theory

In plasma physics, various hierarchical theoretical frameworks exist, varying in complexity and fidelity. Depending on the problem at hand, it is convenient or even necessary to make a suitable choice. The following frameworks are presented based on the book of J. Wesson [1].

The most fundamental model, the *kinetic theory*, treats the plasma as particle distributions that evolve in the six dimensional phase-space according to the *kinetic equation* [80]. Small-scale particle interactions are considered *collisions* and an appropriate model for the Coulomb collisions in a plasma can be obtained with the *Fokker-Planck collision operator* [23], which assumes that small angle collisions dominate. For strong magnetic guiding fields, the particle gyration is averaged into a charge ring motion along the magnetic field line, yielding the *gyro-kinetic theory* [81] and reducing the dimension of the kinetic problem by one. When instead, the gyration is averaged to the movement of a point-charge (center of the charge ring), we speak of the *guiding-center* theories or *drift-kinetic* theories. Taking moments of the particle distributions allows a derivation of the *magnetohydrodynamic* (MHD) theory. Kinetic properties can be partially restored in MHD by treating *energetic particles* (EPs) with distribution functions, that are separated from the MHD-fluid in *MHD-kinetic hybrid models.*

With the reduction of the kinetic equation in section 2.1 we will introduce the Fokker-Planck equation. Discussion of the Fokker-Planck operator is a suitable introduction to the two EP species that are the main subject of this thesis, namely the *fusion-born alpha particles* (alphas) in section 2.1.1 and the *runaway electrons* (REs) in section 2.1.2. The relevance of REs for tokamak research will be made clear in section 2.2 where we talk about *plasma disruptions.* Within the MHD-framework (section 2.3) we will describe the phenomenon of a specific type of plasma waves, the so-called *Alfvén wave.* The interaction of Alfvén waves with EPs however goes beyond its basic MHD properties and eventually requires a discussion of *wave-particle interactions* in section 2.4.

2.1 The Fokker-Planck equation

Fusion plasma dynamics is dictated by the motion of charged particles due to external and self-generated fields. Analogous to thermodynamics, their collective behaviour can generally be described with a distribution function, however, it becomes necessary to include Maxwell's equations describing the effects of electromagnetic forces. The following aspects of collisional plasma physics is introduced based on the textbook by Helander and Sigmar [23].

We begin by defining the distribution function $f(t, \mathbf{x}, \mathbf{v})$ for the time t, with particle position vector $\mathbf{x}$ and particle velocity vector $\mathbf{v} \equiv \dot{\mathbf{x}}$. The function is normalized such that the momentum-space integral returns the particle density $n(t, \mathbf{x}) = \int f(t, \mathbf{x}, \mathbf{v}) \, \mathrm{d}\mathbf{v}$ and the the total integral yields the particle number $N(t) = \int n(t, \mathbf{x}) \, \mathrm{d}\mathbf{x}$. Under a conservation of particle number and an acceleration due to electromagnetic forces, the total rate of change df/dt yields the *Vlasov equation*

$$\frac{\partial f}{\partial t}+\mathbf{v}\cdot\frac{\partial f}{\partial \mathbf{x}}+\frac{q}{m}(\bar{\mathbf{E}}+\mathbf{v}\times\bar{\mathbf{B}})\cdot\frac{\partial f}{\partial \mathbf{v}}=0, \tag{2.1}$$

where q is the particle charge, m the particle mass, $\bar{\mathbf{E}}$ the electric field and $\bar{\mathbf{B}}$ the magnetic field. Outside its *Debye-length*, a plasma particle can be considered electrically neutral and it becomes convenient to separate the microscopic interactions within the Debye-length, i.e. collisions, from macroscopic forces. For the ion kinetics considered in this thesis, we can use the approximation that small-angle Coulomb collisions dominate and use the *Fokker-Planck collision operator* [23, 82, 83] $\mathcal{C}_{\mathrm{FP}}\{f\}=(\partial f/\partial t)_{\mathrm{coll}}$, transforming the Vlasov equation into the Fokker-Planck equation:

$$\frac{\partial f}{\partial t}+\mathbf{v}\cdot\frac{\partial f}{\partial \mathbf{x}}+\frac{q}{m}(\mathbf{E}+\mathbf{v}\times\mathbf{B})\cdot\frac{\partial f}{\partial \mathbf{v}}=\mathcal{C}_{\mathrm{FP}}\{f\}, \tag{2.2}$$

where $\mathbf{E}$ and $\mathbf{B}$ now only represent average, macroscopic (> Debye-length) electric and magnetic fields. The Fokker-Planck operator itself is still a complex object to study [84, 85], but simplifications can be made to solve it explicitly for alpha particles. We assume a small, energetic ion population f_a colliding with a thermal background f_b consisting of electrons and ions. The operator only affects energy and pitch. The gyration is averaged over and the remaining velocity coordinates are aligned with the $\mathbf{B}$-field in an orthogonal system (v,ξ), where $v=|\mathbf{v}|$ is the particle velocity, $\xi\equiv v_{\|}/v$ is the pitch and $v_{\|}$ is the velocity parallel to $\mathbf{B}$. The EP collision operator $\mathcal{C}_{\mathrm{EP}}\{f_a,f_b\}$ reads [23]:

$$\mathcal{C}_{\mathrm{FP}}\{f\}\rightarrow\mathcal{C}_{\mathrm{EP}}\{f_a,f_b\}=\nu_D^{ab}\mathcal{L}\{f_a\}+\frac{1}{v^2}\frac{\partial}{\partial v}\left[v^3\left(\frac{m_a}{m_a+m_b}\nu_s^{ab}f_a+\frac{\nu_{\mathrm{dif}}^{ab}}{2}v\frac{\partial f_a}{\partial v}\right)\right], \tag{2.3}$$

where m_a is the EP mass, m_b is the background particle mass and three distinct processes are identified via their respective collision frequency: the frequency of *pitch-angle scattering* ν_D^{ab}, the *slowing-down* frequency ν_s^{ab}, and the frequency of *parallel diffusion* ν_{dif}^{ab}. The latter is multiplied with the Lorentz scattering operator, defined as

$$\mathcal{L}=\frac{1}{2}\frac{\partial}{\partial\xi}\left(1-\xi^2\right)\frac{\partial}{\partial\xi}.$$

The characteristic frequencies are

$$\nu_D^{ab}(v)=\nu_{ab}\frac{\mathrm{erf}(x_b)-\mathrm{G}(x_b)}{x_a^3}, \tag{2.4}$$

$$\nu_s^{ab}(v)=\nu_{ab}\frac{2T_a}{T_b}\left(1+\frac{m_b}{m_a}\right)\frac{\mathrm{G}(x_b)}{x_a}, \tag{2.5}$$

$$\nu_{\mathrm{dif}}^{ab}(v)=2\nu_{ab}\frac{\mathrm{G}(x_b)}{x_a^3}, \tag{2.6}$$

$$\nu_{ab}=\frac{n_b q_a^2 q_b^2\ln\Lambda}{4\pi\epsilon_0^2 m_a^2 v_{th,a}^3}, \tag{2.7}$$

with a general inter-species collision frequency ν_{ab}, the Coulomb logarithm $\ln\Lambda$, the background particle density n_b, the vacuum permittivity ϵ_0, the respective species charges q_a and q_b, normalized thermal velocities $x_a\equiv v/v_{th,a}$ and $x_b\equiv v/v_{th,b}$, where the respective species thermal velocities are evaluated as $v_{th,a}=\sqrt{2T_a/m_a}$ and $v_{th,b}=$

$\sqrt{2T_b/m_b}$ for the species temperatures T_a and T_b. We have also introduced the Chandrasekar function $\mathrm{G}(x)$ and the error function $\mathrm{erf}(x)$, defined as

$$\mathrm{G}(x) \equiv \frac{\mathrm{erf}(x) - x \cdot \mathrm{erf}'(x)}{2x^2} \to \begin{cases} \frac{2x}{3\sqrt{\pi}}, & x \to 0 \\ \frac{1}{2x^2}, & x \to \infty \end{cases} \tag{2.8}$$

$$\mathrm{erf}(x) \equiv \frac{2}{\sqrt{\pi}} \int_0^x \mathrm{e}^{-y^2}\,\mathrm{d}y, \begin{cases} -1, & x \to -\infty, \\ 1, & x \to \infty \end{cases} \tag{2.9}$$

where $'$ denotes a derivative with respect to x. The collision processes urge to return the EP distribution f_a to its natural state which is the (stationary) Maxwellian distribution function:

$$f_{\mathrm{M}} = \frac{n_b}{\pi^{3/2} v_{th,b}^3} \mathrm{e}^{-(v/v_{th,b})^2},$$

With this property the Fokker-Planck operator fulfils the H-theorem [80], as it increases the entropy of the system and vanishes, once Maxwellians (of equal temperature) are obtained.

2.1.1 Fusion-born alpha particles

In the circumstance of a burning deuterium-tritium plasma alpha particles are born through nuclear fusion. In steady-state, they form a *slowing-down* distribution [86], that can be derived from the Fokker-Planck equation (eq. (2.2)) and the energetic particle collision operator (eq. (2.3)) for a small, energetic alpha species f_α, a thermal electron species f_{e} and a thermal ion species f_{i}.

Starting point is the operator $\mathcal{C}_{\mathrm{EP}}\{f_\alpha, f_{\mathrm{e,i}}\}$, whose bilinear nature[1] allows a separate treatment of alpha-electron and alpha-ion collisions. Alpha particles emerge at a kinetic birth energy of $E_{\alpha 0} = 3.5$ MeV and a corresponding velocity $v_{\alpha 0} \approx 1.3 \cdot 10^7$m/s, hence these ions are considered energetic with respect to the plasma background, which averages to a typical mean temperature of approximately 10-20 keV. The birth process is isotropic to a good approximation [87].

In a typical fusion plasma, the electron temperature T_e and the ion temperature T_i are similar, fulfilling

$$v_{th,i} \ll v_{\alpha 0} \ll v_{th,e}$$

for the respective thermal velocities $v_{th,e} \equiv \sqrt{2T_e/m_e}$ and $v_{th,i} \equiv \sqrt{2T_i/m_i}$. Although a temperature cannot be assigned directly to the non-Maxwellian distribution of alphas, the average alpha particle velocity corresponds to an energy of approximately $T_\alpha \approx$ 1 MeV. In the velocity and temperature regimes considered, pitch-angle scattering and velocity diffusion become negligible compared to the slowing-down frequency (eq. (2.5)).

The Chandrasekhar function $\mathrm{G}(x_b)$ (eq. (2.8)) for alpha drag against electrons is evaluated for $x_b = x_e \to 0$, and the result is expressed with the slowing-down time τ_s:

$$\frac{1}{\nu_s^{\alpha e}} = \tau_s = \frac{3(2\pi)^{3/2} \epsilon_0^2 m_\alpha T_e^{3/2}}{Z_\alpha^2 e^2 m_e^{1/2} n_e \ln\Lambda}, \tag{2.10}$$

with the elementary charge e, the alpha particle charge $Z_\alpha = 2e$, the alpha particle mass m_α, the electron mass m_e and the electron density n_e. For the alpha drag against ions,

---

[1] $\mathcal{C}\{f_\alpha, f_{\mathrm{e,i}}\} = \mathcal{C}\{f_\alpha, f_{\mathrm{e}}\} + \mathcal{C}\{f_\alpha, f_{\mathrm{i}}\}$.

$\mathrm{G}(x_b)$ is evaluated for $x_b = x_i \to \infty$, yielding

$$\nu_s^{\alpha \mathrm{i}} = \left(\frac{v_c}{v}\right)^3 \frac{1}{\tau_s} \frac{m_\alpha + m_i}{m_\alpha}, \tag{2.11}$$

where we defined the cross-over velocity v_c as

$$v_c \equiv \left(\frac{3\sqrt{\pi}\, m_e n_i Z_i^2}{4 n_e m_i}\right)^{1/3} v_{th,e}. \tag{2.12}$$

for the ion density n_i, the ion charge Z_i and the ion mass m_i. This crossover velocity v_c defines a threshold value, above which the alpha-electron drag dominates over the alpha-ion drag.

With $\nu_s^{\alpha(\mathrm{i,e})} = \nu_s^{\alpha \mathrm{e}} + \nu_s^{\alpha \mathrm{i}}$ and equations (2.10)-(2.12), we can explicitly state the isotropic Fokker-Planck collision operator (eq. (2.3)) for the alphas

$$\mathcal{C}_{\mathrm{EP}}\{f_\alpha, f_{\mathrm{e,i}}\} = \frac{1}{v^2 \tau_s} \frac{\partial}{\partial v} \left[(v^3 + v_c^3) f_\alpha(v)\right]. \tag{2.13}$$

We state the kinetic equation (2.2) for alpha particles:

$$\frac{\partial f_\alpha}{\partial t} + \mathbf{v} \cdot \frac{\partial f_\alpha}{\partial \mathbf{x}} + \frac{Z_\alpha e}{m_\alpha} (\mathbf{E} + \mathbf{v} \times \mathbf{B}) \cdot \frac{\partial f_\alpha}{\partial \mathbf{v}} = \mathcal{C}_{\mathrm{EP}}\{f_\alpha, f_{\mathrm{e,i}}\}, + S_\alpha \delta(v - v_{\alpha 0}), \tag{2.14}$$

where we have addressed the birth process with an additional alpha particle source S_α and the delta function $\delta(v - v_{\alpha 0})$. The alpha particles are born close to the magnetic axis, where the flux-surfaces radius is small compared to the major radius of the tokamak and the problem can be treated in the (local) large aspect ratio limit. In this limit, spatial effects across flux-surfaces can be neglected and because the plasma is strongly homogeneous along the magnetic field lines, all spatial dependencies ($\partial f_\alpha / \partial \mathbf{x}$) are dropped. For the velocity space, we perform gyro-averaging and align a coordinate system ($v, \xi = v_\parallel / v$) parallel to the magnetic field lines, for which the kinetic equation can be stated as [53]:

$$\frac{\partial f_\alpha}{\partial t} + \frac{Z_\alpha e}{m_\alpha} E_\parallel \left(\xi \frac{\partial}{\partial v} + \frac{1 - \xi^2}{v} \frac{\partial}{\partial \xi}\right) f_\alpha = \mathcal{C}_{\mathrm{EP}}\{f_\alpha, f_{\mathrm{e,i}}\}, + \frac{S_\alpha \delta(v - v_{\alpha 0})}{4\pi v_{\alpha 0}^2}, \tag{2.15}$$

where $E_\parallel$ is the parallel electric field. For a steady state solution ($\partial f_\alpha / \partial t = 0$) with negligible electric field strength, the kinetic equation is solved by the so-called *slowing-down* distribution f_0 [86]:

$$f_0 = \frac{S_\alpha \tau_s}{4\pi (v^3 + v_c^3)} \mathrm{U}(v_{\alpha 0} - v), \tag{2.16}$$

where we have introduced the unit step function $\mathrm{U}(x)$ limiting the velocity distribution to the birth velocity.

A sketch of the function is shown in figure 2.1 for typical fusion parameters. After emerging from the fusion reaction, the energetic alpha particle collides with the cooler background and creates the depicted slowing-down shape. Between thermal ion velocity, initial alpha velocity and thermal electron velocity respectively lies approximately one order of magnitude. As above the cross-over velocity v_c the electron drag dominates, a main portion of the alpha energy in a tokamak is transferred into the electrons. With its lower mass, a thermal electron is faster than an alpha particle, with $v_{th,e}/v_{\alpha 0} \approx 7.2$

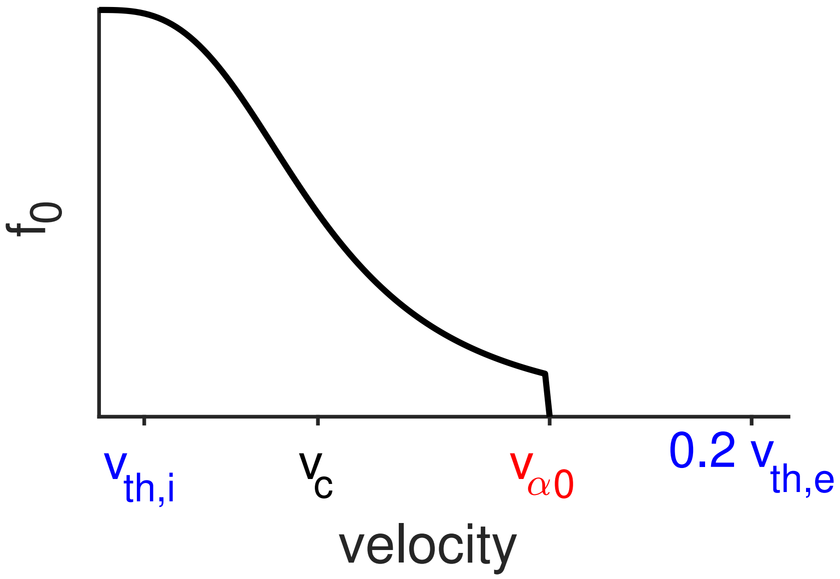

Figure 2.1: Sketch of an alpha particle slowing-down distribution f_0 for typical fusion parameters.

($T_e = 25\,\mathrm{keV}$). Because of an energy diffusion effect [88] the alpha particles have an velocity distribution around the birth velocity, which will be addressed in section 5.2.2 through an approximation of the unit-step function. The alpha particles accumulate at lower energies and effectively merge together with the background as they approach thermal ion velocities. At this point the alpha particles are usually considered Helium ash, which need to be removed from the system to balance the birth process and avoid a dilution of the fuel plasma [89]. The presence of Helium-ash has no significant impact on the mode evolution discussed later in this thesis.

2.1.2 Runaway electrons

We return to the collisions of energetic particles with a thermal background and look at the slowing-down frequency of electron-electron collisions ν_s^{ee} (eq. (2.5)). The slowing-down process on a parallel velocity $v_\parallel$ can be associated with a Coulomb friction force $F_{c,\parallel}$:

$$F_{c,\parallel} \equiv \frac{m_e \langle \Delta v_\parallel \rangle^{\mathrm{ee}}}{\Delta t} = -m_e v_\parallel \nu_s^{\mathrm{ee}} \propto G(x_e) \tag{2.17}$$

where average changes to the parallel velocity $\langle \Delta v_\parallel \rangle^{\mathrm{ee}}$ over some time Δt become proportional to the Chandrasekhar function $\mathrm{G}(x_e)$ (eq. (2.8)). The electron-electron friction force is sketched in figure 2.2 as a function of the particle velocity. Electron-ion collisions yield the same scaling as electron-electron collisions at high velocities $v_\parallel$. At high electron velocities, $\mathrm{G}(x_e)$ has to be evaluated in the large argument limit $x_e = v_\parallel / v_{th,e} \to \infty$, yielding the proportionality

$$G(x_e) \propto v_\parallel^{-2},$$

with key implications. The function peaks close to the thermal electron velocity $v_{th,e}$ and afterwards begins dropping as $v_\parallel^{-2}$: A force accelerating an already energetic electron towards higher velocities will reduce the (decelerating) friction. With some constant force $eE_\parallel > eE_c$ opposing the friction, any electron above a critical threshold - v_{crit} - will overcome the friction and is accelerated continuously - it will *run away*. The

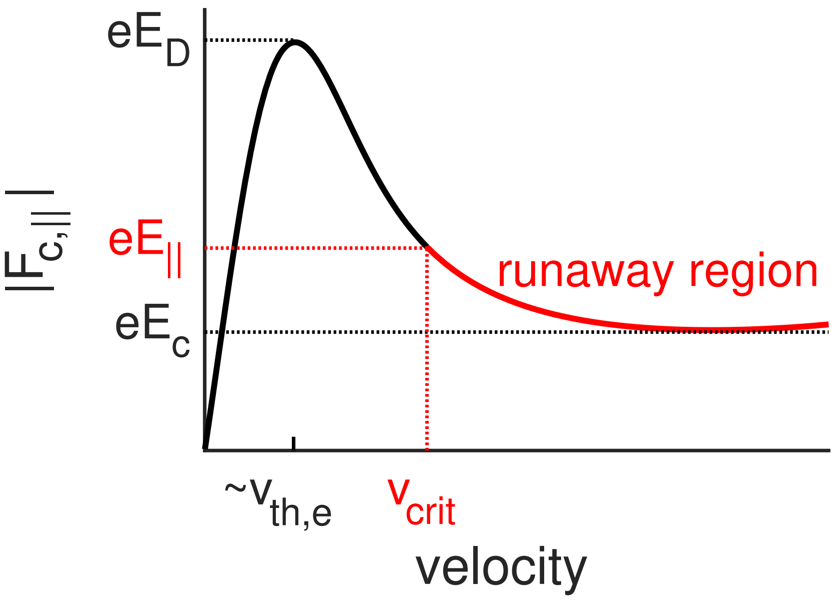

Figure 2.2: An illustration of the (parallel) electron-electron friction force $\left|F_{c,\parallel}\right|$ in a plasma as a function of electron velocity. A typical force counteracting friction in a tokamak is an electric field $E_\parallel$. If the magnitude of the electric field overcomes the friction force, electrons with $v > v_{\text{crit}}$ are accelerated into the *runaway region*.

physical reason is, that with rising electron speed, the momentum exchange in a collision decreases stronger than the increased number of collision encounters can balance out [23].

Relativistic energies ($\sim$ MeV) can be reached, where the effects of synchrotron emission (predominantly due to gyration) and Bremstrahlung due to inelastic scattering off heavier ions become important [90]. As the emission takes momentum away from the runaway electron, momentum conservation acts as an additional force opposing the electric field. This creates an enclosed *runaway region* which is also sketched in figure 2.2, though not captured by eq. (2.17).

In a tokamak plasma the relevant accelerating force is assumed by an electric field $E_\parallel$. The friction minimum in the runaway region is balanced by a critical electric field [91, 92]

$$E_c = \frac{n_e e^3 \ln \Lambda}{4\pi\epsilon_0^2 m_e c^2}, \tag{2.18}$$

where c is the speed of light. This electric field threshold specifies a value above which the runaway phenomenon can occur in the first place. Effects like pitch angle scattering change the critical field [6], as does the inclusion of partially ionized impurities [93]. Partially ionized impurities effectively increase the friction, as the electron cloud of a nucleus can be penetrated by the energetic RE [94]. As a result, the electron collides with a higher net charge of the ion and increases general collision frequency in eq. (2.7). The critical velocity v_{crit} marks the beginning of the runaway region and is often given in terms of a normalized momentum $p = \gamma v/c$, where $\gamma = 1/\sqrt{1 - v^2/c^2}$ is the relativistic Lorentz factor:

$$p_{\text{crit}} = \frac{1}{\sqrt{E/E_c - 1}}, \tag{2.19}$$

for electron motion parallel to the electric field [92]. The electric field balancing the maximum of the friction force, is the so-called *Dreicer* field [95, 96]

$$E_{\text{D}} = \frac{n_e e^3 \ln \Lambda}{4\pi\epsilon_0^2 T_e}. \tag{2.20}$$

A *slide-away* effect [97, 98] can occur for $E_{\|} \gtrapprox 0.214 E_{\mathrm{D}}$ [95], where the entire electron population becomes runaway.

For a detailed study on REs, generation processes are commonly divided into *primary* and *secondary* mechanism. The classical primary generation is the *Dreicer* generation [95], which repopulates a depleted momentum space region $p \geq p_{\mathrm{crit}}$ through collisional diffusion, providing a channel from the bulk population into the runaway region. Through evaluation of a relativistic kinetic equation, an explicit expression was found [92] for the RE number density n_{RE} growing due to the Dreicer growth rate γ_{Dreic}. For a limit $E_{\|} \gg E_c$ and fully ionized plasmas one can approximate the dominating scaling to be

$$\gamma_{\mathrm{Dreic}} \equiv \left(\frac{\partial n_{\mathrm{RE}}}{\partial t}\right)_{\mathrm{Dreic}} \propto \exp\left(-\frac{E_{\mathrm{D}}}{4E_{\|}}\right). \tag{2.21}$$

An up-to-date model for the Dreicer calculation includes the effects of partially ionized impurities [99]. The presence of partially ionized impurities generally reduces the Dreicer growth rate and especially for mitigated disruptions is foreseen to be negligible [99, 100].

Another important primary mechanism is the hot-tail generation [101–105]: The energetic tail of a cooling thermal electron population equilibrates on a slower time-scale than its bulk and can end up in the runaway electron region, which is formed by rising electric field $E_{\|}$. This mechanism is especially significant, when the cooling rate of the plasma is comparable to the collision frequency of highly energetic electrons [102]. For the nuclear phase of a plasma, the electron produced in the beta decay of tritium can become a RE when the emitted electron with an energy of 18.6 keV is energetic enough to overcome p_{crit} [106]. The neutron produced in the nuclear reaction (see introduction) activates the tokamak walls, which proceed to emit photons that can generate a RE in a Compton scattering process [106, 107]. Dreicer, hot-tail, Compton and beta-decay mechanisms create a so-called runaway electron *seed*.

Once a runaway seed is present, a secondary generation mechanism can take effect. The seed electron collides knock-on with a thermal electron and pushes it into the runaway region, while itself remaining in it. Due to its multiplicative nature, this process grows exponentially in time and is therefore suitably called *runaway avalanche* [94, 108, 109]. This avalanching cannot be captured using a Fokker-Planck collision operator (eq. (2.3)) as that assumes small-angle collisions only. The calculation requires dealing with the Boltzmann collision operator for large-angle collisions [110]. Approximate solutions were initially found [109] by treating the distribution of avalanching electrons with a source term S in the kinetic equation and obtain a growth rate

$$\gamma_{\mathrm{av}} \equiv \left(\frac{\partial n_{\mathrm{RE}}}{\partial t}\right)_{\mathrm{av}} \propto n_{\mathrm{RE}} \left(\frac{E}{E_C} - 1\right), \tag{2.22}$$

in the limit of $E \gg E_c$ (and a large aspect ratio tokamak). Because of its multiplicative nature, the avalanching mechanism can offer a significant contribution to the runaway electron generation, with typical particle energies of 10 MeV [6]. An up-to-date model includes the effects of partially ionized impurities, which may significantly **increase** the avalanche growth rate [111]. This occurs because REs penetrating the nucleus' electron clouds encounter more target electrons for avalanching, and this can not be compensated by the increased friction caused by the higher net charge of the nucleus [111].

In tokamak ramp-up phase, strong electric fields are required to form a plasma and thus runaway electrons may be generated [112, 113]. In the quiescent operation that follows runaways are not problematic, because the electric field required to drive the plasma current is weak due to the high conductivity of a hot plasma. However, a plasma disruption event (see section 2.2) strongly decreases the plasma temperature and thus reduces the conductivity, giving rise to a strong electric field $E_\parallel$. These disruption-induced electric fields usually fulfill $E_c < E_\parallel \ll E_\mathrm{D}$ and runaway generation can occur [5]. The study of runaway electrons in this work is conducted in the context of such tokamak plasma disruptions, where it is not a desirable phenomenon.

Positively charged species can also be subject to the runaway generation mechanism: Ion runaway [114] is suspected to occur during internal magnetic reconnection events [54], however, generation by the disruption-induced electric field is unlikely on disruption time-scales [52, 53] because of the larger ion mass. Since an average RE energy ($\sim 10\,\mathrm{MeV}$) far exceeds its rest mass equivalent, a pair-production process between a RE and a thermal electron can generate positrons [115–117]. Even though the time-scale of annihilation is smaller than disruption time-scales [115], a positron runaway beam is not as significant as its electron counterpart. Because a newly created positron tends to co-move with the runaway electron, i.e. predominantly anti-parallel to the electric field, it will be decelerated along the electric field direction and most likely thermalize [115].

2.2 Plasma disruptions and runaway electron mitigation attempts

Plasma disruption [8, 118] in a tokamak is an abrupt, unplanned termination of the discharge. The thermal and electromagnetic energy stored in the plasma is released, with the potential of damaging the device. Besides direct heat loads onto plasma-facing components and electromagnetic forces exerted on structures [6], runaway electron beam generation is a major concern, especially for high-current, reactor-relevant tokamaks such as ITER [4, 5, 26]. A pivotal reason is, that the number density of runaway electrons generated via avalanche (section 2.1.2) in a disruption was found to scale as $n_\mathrm{RE} \propto \exp(2.5 I_p\,[\mathrm{MA}])$ with the plasma current I_p [118]. At the currently largest tokamak JET [51] a plasma current of 2.7 MA can reached, while ITER is planned to operate at a maximum of 15 MA [2]. Avoidance of tokamak disruptions is targeted [7], but cannot fully be ensured as the maximisation of performance requires an operation close to stability limits [119]. As such, the field of runaway electron mitigation is actively being researched [5, 8, 26].

A plasma disruption is commonly divided into the thermal quench (TQ) and a consequent current quench (CQ). The TQ encompasses a plasma temperature (T) breakdown of many orders of magnitude - from tens of keVs to eVs over a timescale of milliseconds. When the plasma cools, its electrical resistivity rises $\sigma \propto T^{-3/2}$ [119] drastically. The self-induction of the plasma however, prevents the plasma current from changing on the same time-scale as the temperature. Due to Ohm's law, $E = \sigma j$, an electric field E rises in trying to maintain the current density j. The period of current decay is called CQ and follows the TQ. The induced electric field develops in toroidal direction and can be strong enough to generate runaway electrons (section 2.1.2), fulfilling $E_c < E_\parallel$. Because of the RE generation, the electric field transforms a current carried by the thermal population (Ohmic current) into a current carried by runaways (runaway current). A significant portion of the initial plasma current is expected to be carried by relativistic runaways by the end of the CQ [25, 106, 107], with the avalanche mechanism playing a major contribution [94]. A concentrated beam of runaway electrons with componentmelting capabilities [11, 12] is formed during a period where control over the plasma is gradually lost.

High effort is put into researching and designing systems that are able to mitigate the RE generation [5, 8, 26]. The obvious way is to increase the electron density n_e and raise the critical electric field threshold (eq. (2.18)). In addition, it is desired that a large fraction of the plasma energy is radiated away, as the radiation is ideally isotropic and would de-localize the heat load. As such, mitigation systems revolve around *massive material injection* (MMI), which raises plasma density and facilitates a means to increase the irradiation of the plasma energy content. Simply flooding the tokamak chamber with material and pushing the electric field threshold out of range is not viable however. It turns out [8], that the mitigation system must find a balance and distribute the energy release accordingly, so neither the heat loads or the electromagnetic stress, nor the RE beam energy can overcome a threshold that would cause damage to the device. A too fast termination could cause the plasma chamber walls to either melt from the thermal load or to deform due to electromagnetically generated torque [6]. A minimal duration of the CQ of be approximately 35 ms is suggested as an acceptable lower limit [26]. For the upper bound of the CQ time-window, a duration of approximately 150 ms [107] should not be overcome to ensure a complete radiative collapse. If the temperature drops too fast, the plasma begins to recombine (at $\approx 2\,\mathrm{eV}$ for hydrogen [107]) before the induced electric field has decayed and - as mentioned in section 2.1.2 - the partial screening effect increases avalanche generation. Because of the partial screening effect, the composition of the injected material also has to be chosen carefully [94].

Experiments with MMI systems show that a penetration of the injected material into the core of a plasma is not guaranteed [11, 27]. In order to mitigate electron generation in the plasma core, *shattered pellet injection* (SPI) systems are researched [120–122]. This method relies on cryogenically frozen pellets being scattered into the plasma for an increased penetration depth. The material composition and amount is still an open question, although a mixture of deuterium and neon is likely [107]. Despite the effort, it appears [26] that currently available mitigation technologies require further development to reliably prevent the formation of a runaway electron beam in the nuclear phase ITER plasma.

Since velocity-space effects cannot guarantee avoidance, additional spatial effects should be considered, e.g. increased transport of REs may help suppress runaway electron formation. The RE beam can be susceptible to *ergodic zones*, in which magnetic field lines behave chaotically and may cause radial transport of runaways [26]. Using *Resonant Magnetic Perturbations* (RMPs) this behaviour can be exploited by applying external magnetic fields, that perturb the plasma equilibrium field. While RMPs have been observed to suppress runaways in smaller tokamaks [28, 29], it is not reproducible at the large tokamak JET [32]. Because of the externally applied nature of the RMPs, runaways that are predominantly formed in the core of the plasma are hard to reach [9, 33, 123, 124], though mitigating effects still seem possible when applied pre-disruption [125]. *Passive helical coils* [30] (PHCs) is a similar technique, that relies on perturbation-induced de-confinement of REs and is currently in discussion as disruption mitigation aid [31, 126, 127]. With helical coils placed inside the vessel, the induced electric field of a disruption would drive currents through these coils, generating ergodic zones in the plasma. RMPs and PHCs would both benefit from a mechanism that enhances the runaway transport in the plasma core. The primary goal of this thesis is to investigate one such mechanism, which induces perturbations through plasma waves.

2.3 Plasma waves in the magnetohydrodynamic framework

Magnetohydrodynamic (MHD) theory [20] is a useful tool to model large scale plasma physics behavior. In this framework, the plasma is understood as a conductive, current-carrying fluid immersed in a magnetic field and described by moments of its particle distribution functions, i.e. density, temperature and (flow) velocity (This assumes the particle distributions to be in Maxwellian form). In the *ideal* MHD model, one assumes the plasma to have zero resistivity, zero heat conductivity and zero viscosity, effectively 'freezing' the plasma to the magnetic field lines. The model is often applied in researching the stability of plasma equilibrium configurations. We will follow references [119, 128] to derive linearized MHD equations from ideal, single-fluid MHD.

The ideal MHD equations for a single fluid read [119]

$$\frac{\mathrm{d}\rho}{\mathrm{d}t} + \rho\nabla\cdot\mathbf{v} = 0, \tag{2.23}$$

$$\rho\,\frac{\mathrm{d}\mathbf{v}}{\mathrm{d}t} = \mathbf{j}\times\mathbf{B} - \nabla p, \tag{2.24}$$

$$\frac{\mathrm{d}}{\mathrm{d}t}\left(\frac{p}{\rho^{\gamma}}\right) = 0, \tag{2.25}$$

$$\mathbf{E} + \mathbf{v}\times\mathbf{B} = 0, \tag{2.26}$$

$$\nabla\cdot\mathbf{B} = 0, \tag{2.27}$$

$$\nabla\times\mathbf{B} = \mu_0\mathbf{j}, \tag{2.28}$$

$$\nabla\times\mathbf{E} = -\,\frac{\partial\mathbf{B}}{\partial t}\,, \tag{2.29}$$

where ρ is the plasma mass density, γ an adiabatic coefficient, p the plasma pressure, $\mathbf{v}$ the plasma velocity, $\mathbf{B}$ the magnetic field, $\mathbf{E}$ the electric field and $\mathbf{j}$ the current density. In a static and time-independent assumption, we obtain the equations

$$\begin{aligned}\mathbf{j}\times\mathbf{B} &= \nabla p,\\ \nabla\times\mathbf{B} &= \mu_0\mathbf{j},\\ \nabla\cdot\mathbf{B} &= 0,\end{aligned}$$

which define the equilibrium of the magnetic field.

The above MHD equations (2.23)-(2.29) will now be linearized for the purpose of stability analysis. To all dependent variables, we introduce small, time-dependent perturbations $Q_1 \ll Q_0$ to the constant equilibrium quantities Q_0. With $Q(\mathbf{x},t) = Q_0(\mathbf{x}) + Q_1(\mathbf{x},t)$ the linearized MHD equations read

$$\frac{\partial\rho_1}{\partial t} + \nabla\cdot(\rho_0\mathbf{v}_1) = 0, \tag{2.30}$$

$$\rho_0\,\frac{\partial\mathbf{v}_1}{\partial t} = \mathbf{j}_1\times\mathbf{B}_0 + \mathbf{j}_0\times\mathbf{B}_1 - \nabla p_1, \tag{2.31}$$

$$\frac{\partial p_1}{\partial t} + \mathbf{v}_1\cdot\nabla p_0 + \frac{\gamma p_0}{\rho_0}\left(\frac{\partial\rho_1}{\partial t} + \mathbf{v}_1\cdot\nabla\rho_0\right) = 0, \tag{2.32}$$

$$\mathbf{E}_1 = -\mathbf{v}_1\times\mathbf{B}_1, \tag{2.33}$$

$$\nabla\cdot\mathbf{B}_1 = 0, \tag{2.34}$$

$$\nabla\times\mathbf{B}_1 = \mu_0\mathbf{j}_1, \tag{2.35}$$

$$\frac{\partial\mathbf{B}_1}{\partial t} = \nabla\times(\mathbf{v}_1\times\mathbf{B}_0), \tag{2.36}$$

We assume normal mode expansion, which means that perturbed quantities can be expressed in the form $Q_1(\mathbf{x},t) = Q_1(\mathbf{x})\exp(-i\omega t)$. Furthermore, we define a displacement vector $\boldsymbol{\xi}(\mathbf{x},t)$, such that $\mathbf{v}_1 \equiv \frac{\partial \boldsymbol{\xi}}{\partial t}$. With the displacement vector one can express all perturbed quantities in terms of $\boldsymbol{\xi}$, yielding the relations

$$\rho_1 = -\nabla \cdot (\rho \boldsymbol{\xi}), \tag{2.37}$$

$$p_1 = -\boldsymbol{\xi} \cdot \nabla p - \gamma p \nabla \cdot \boldsymbol{\xi}, \tag{2.38}$$

$$\mathbf{B}_1 = \nabla \times (\boldsymbol{\xi} \times \mathbf{B}), \tag{2.39}$$

$$\mu_0 \mathbf{j}_1 = \nabla \times [\nabla \times (\boldsymbol{\xi} \times \mathbf{B})], \tag{2.40}$$

where the 0 subscript for equilibrium quantities has been dropped. Inserting equations (2.37)-(2.40) into the linearized momentum equation (2.31), we obtain the equation

$$-\omega^2 \rho \boldsymbol{\xi} = \mathbf{F}(\boldsymbol{\xi}), \tag{2.41}$$

for the force-operator

$$\mathbf{F}(\boldsymbol{\xi}) = \mu_0^{-1}(\nabla \times \mathbf{B}) \times [\nabla \times (\boldsymbol{\xi} \times \mathbf{B})] + \mu_0^{-1}\{\nabla \times [\nabla \times (\boldsymbol{\xi} \times \mathbf{B})]\} \times \mathbf{B} + \nabla(\boldsymbol{\xi} \cdot \nabla p + \gamma p \nabla \cdot \boldsymbol{\xi}).$$

Equation (2.41) is a vector equation for the three components of $\boldsymbol{\xi}$ and formally an eigenvalue problem with the eigenvalue ω. $\mathbf{F}$ is a self-adjoint operator, so ω is either purely real, representing an oscillating wave, or purely imaginary, representing a wave evolving exponentially in amplitude. Applying boundary conditions and solving equation (2.41) we can analyze the linear stability of magnetic field equilibria.

2.3.1 The shear Alfvén wave

We analyze the solutions of the force-operator equation (2.41) in an infinite plasma, that is aligned with a homogeneous equilibrium magnetic field $\mathbf{B} = B\mathbf{e}_z$ in z-direction of a Cartesian coordinate system. Fourier-decomposed perturbations in the form of $\boldsymbol{\xi} = \xi \exp(i\mathbf{k} \cdot \mathbf{x})$ are introduced, where the wave vector is aligned as $\mathbf{k} = k_\perp \mathbf{y} + k_\parallel \mathbf{z}$. The force-operator equation is now stated as

$$\omega^2 \rho \boldsymbol{\xi} = \frac{B^2}{\mu_0}\{\mathbf{k} \times [\mathbf{k} \times (\boldsymbol{\xi} \times \mathbf{e}_z)]\} \times \mathbf{e}_z + \gamma p \mathbf{k}(\mathbf{k} \cdot \boldsymbol{\xi}) \tag{2.42}$$

and the three vector components of the equation rewritten into a matrix form:

$$\begin{pmatrix} \omega^2 - k_\parallel^2 v_A^2 & 0 & 0 \\ 0 & \omega^2 - k_\perp^2 v_s^2 - k^2 v_A^2 & -k_\perp k_\parallel v_s^2 \\ 0 & -k_\perp k_\parallel v_s^2 & \omega^2 - k_\parallel^2 v_s^2 \end{pmatrix} \begin{pmatrix} \xi_x \\ \xi_y \\ \xi_z \end{pmatrix} = 0 \tag{2.43}$$

with the so-called Alfvén velocity $v_A = \sqrt{B^2/\mu_0 \rho}$ and the adiabatic sound velocity $v_s = \sqrt{\gamma p/\rho}$. Note that the displacement in x-direction is decoupled from the y and z. We solve eq. (2.43) by equating the matrix determinant to zero

$$(\omega^2 - k_\parallel^2 v_A^2)\left[\omega^4 - (v_s^2 + v_A^2)k^2\omega^2 + (k k_\parallel v_s v_A)^2\right] = 0,$$

and obtain three distinct solutions for ω^2. The decoupled x-component shows the most obvious solution

$$\omega^2 = v_A^2 k_\parallel^2,$$

which is the dispersion relation for the *shear Alfvén wave* (SAW) in a homogeneous plasma. It is independent of $k_\perp$, hence propagating along the magnetic field and facilitates a purely oscillating, i.e. stable solution. Through back substitution one finds the Alfvén wave to be incompressible, $p_1 = 0$, and with transverse movement, $\mathbf{v}_1$ and $\mathbf{B}_1$ perpendicular to $\mathbf{B}_0$. Since the phase velocity $v_{\mathrm{ph}} = \omega/k_\parallel$ is constant, there is no dispersion. Physically, the Alfvén wave resembles a balance between the plasma inertia and the magnetic field line tension that acts as a restoring force.

Further solutions to the matrix equation are known as the *slow magnetosonic* and the *fast magnetosonic* wave, which represent a coupling between magnetic (Alfvénic) and fluid (sonic) compression. The magnetosonic waves are compressible, oscillating, and polarized, i.e. with both the displacement vector and magnetic perturbation having transversal and longitudinal components. The coupling parameter between the SAW and magnetosonic waves is the plasma-β:

$$\beta \equiv \frac{2\mu_0 p}{B^2},$$

which in tokamaks is of the order of percentages and therefore we neglect coupling to magnetosonic waves.

2.3.2 The toroidicity-induced Alfvén Eigenmode (TAE)

Switching from a uniform plasma to a torus has important consequences on the SAW due to periodicity, if one chooses the inverse aspect ratio $\epsilon = a/R_0$ as a smallness parameter. The wave perturbation vector $\boldsymbol{\xi}$ is Fourier-decomposed into

$$\boldsymbol{\xi}(r,\theta,\phi) = \sum_{m,n} \xi_{n,m}(r) \mathrm{e}^{i(n\zeta - m\theta - \omega t)},$$

where n is the toroidal mode number, ζ is the toroidal angle, m is the poloidal mode number and θ the poloidal angle. Due to the axisymmetry of the torus, the waves decouple in the toroidal direction, but because the magnetic field is a function of θ they couple to neighbouring poloidal harmonics $m \pm 1$. The wave vector reads

$$k_{\parallel,m}(r) = \frac{1}{R}\left(n - \frac{m}{q(r)}\right), \tag{2.44}$$

with the (approximate) safety-factor profile $q(r) = \epsilon B_\zeta / B_\theta$. $k_\parallel$ is a function of both m and r and the solutions of the Alfvénic continuum

$$\omega^2(r) = \begin{cases} +k_{\parallel,m}(r)^2 v_A(r)^2, \\ -k_{\parallel,m}(r)^2 v_A(r)^2, \end{cases} \tag{2.45}$$

can intersect for different m. The location of the intersection is obtained by equating $k_{\parallel,m}$ and $k_{\parallel,m+1}$ and can be expressed in terms of the safety factor

$$q(r_{\mathrm{TAE}}) = \frac{m + 1/2}{n}.$$

The toroidicity-induced degeneracy of the intersection is resolved by the system by producing gaps in the frequency spectrum, giving rise to so-called *Toroidicity-induced Alfvén Eigenmodes* [46] (TAEs). An example of an Alfvén continuum is shown in figure 2.3. The radial extent of the frequency gaps can be global, with a gap width approximated by [22]

$$\Delta_{\mathrm{TAE}} \approx r_{\mathrm{TAE}}/m \tag{2.46}$$

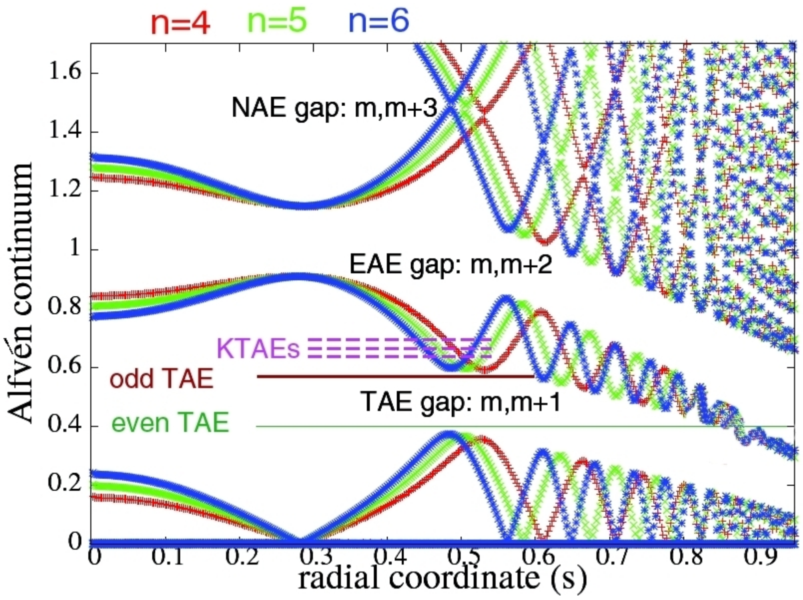

Figure 2.3: The Alfvén continuum ($(\omega/\omega_{\mathrm{TAE}})^2$) calculated for the ASDEX Upgrade discharge #21067 at 2.99 s for $n = 4-6$. One can see the gaps produced by symmetries which - depending on their order - create continuum gaps for TAEs, EAEs and NAEs. KTAEs are kinetic TAEs [129] not considered in this work. Figure taken from the thesis of P. Lauber [130].

Depending on the relative phase of the coupling harmonics, the TAE is considered *even* ($(m, m+1)$ in phase) or *odd* ($(m, m+1)$ opposite phase). Even TAEs have frequencies at the lower gap boundary, while odd TAEs have frequencies at the upper gap boundary [46].

Contrary to the uniform plasma case, the Alfvén modes of a toroidal plasma are not dispersionless due to the dispersion relation (eq. (2.45)) being a function of radius. With $\omega(r) = k_{\|}(r)v_A(r)$, a wave packet in an inhomogeneous plasma will disperse in an effect called phase mixing [131], which damps the wave very effectively with a damping strength proportional to the radial gradient $\gamma \propto \mathrm{d}/\mathrm{d}r(k_{\|}v_A)$. This is usually referred to as *continuum damping*. However, in the toriodicity-induced frequency gaps, this continuum damping is lacking and the TAE is considered a weakly damped mode.

Although the TAE is arguably the most studied Alfvén mode, an entire zoo of various other Alfvénic modes exist, of which a review can be found e.g. in a review paper by W. Heidbrink [129]. These can be produced for example by asymmetries of a higher order, such as ellipticity (EAE) and triangularity (NAE), which create a coupling between $(m, m+2)$ and $(m, m+3)$ poloidal harmonics respectively (see figure 2.3). Other types of Alfvénic modes can occur due to an extremum in the q-profile, e.g. the Reversed-shear AE (RSAE) or the Beta-induced AE (BAE).

In this work however, we will focus on the TAE, due to its weakly damped nature and because it has a characteristically low frequency, $\omega_{\mathrm{TAE}} = v_A/(2qR_0) \sim 100\,\mathrm{kHz}$. As we will discuss in section 2.4 this allows effective resonance with energetic particles in a tokamak. Additionally, flat q-profiles allow a significant radial extent of TAEs and are commonly found in tokamaks. These reasons open up the possibility of global modes [132, 133], which can be driven to large amplitudes by either passing or trapped energetic ions [46] through resonant interaction. As the modes presented here are oscillatory (ω real) in the ideal MHD framework, calculating the drive/damping requires a kinetic theory (e.g. drift- or gyrokinetic models). This constitutes the resonant wave-particle interaction explained in section 2.4.

2.4 The mechanism of resonant wave-particle interaction

Interaction between plasma waves and particles is possible through resonant wave-particle interaction. The phase velocity of Alfvénic modes v_A is generally super-thermal in a tokamak plasma, so it becomes convenient to divide the particle distributions into a thermal component and an energetic part. The thermal background consists of the majority of the plasma, its bulk, and can be appropriately described by the MHD approach. Often it will generally act to damp Alfvénic modes, while energetic particles exert a driving, destabilizing force. The rapid gyro motion averages to a net zero energy transfer, because the gyrofrequency (for both ions and electrons) is generally well above than the mode eigenfrequency ω. As such we follow the derivation of references [129, 134], which are written for a drift-kinetic model.

In a tokamak, the resonance condition for a particle in a tokamak equilibrium perturbed by a wave with eigenfrequency ω, toroidal mode number n and poloidal mode number m can be stated as [134]

$$v_{\|} = \frac{qR_0\omega}{nq - m - l},$$

where $v_{\|}$ is the parallel particle velocity and l originates from a Fourier expansion of the particle drift orbit in an orbital harmonic.

As stated in the previous section, the location of a TAE in the safety-factor profile is $q(r_{\mathrm{TAE}}) = (m + 1/2)/n$ (eq. (2.3.2)), which is where global modes can form and avoid continuum damping. Plugging the TAE location into the resonance condition yields

$$v_{\|} = \frac{v_A}{|2l - 1|},$$

where $l = 0$ describes the primary resonance $v_{\|} = v_A$ and higher values of l correspond to higher harmonics at lower velocities. Importantly, the alpha particle birth velocity (see section 2.1.1) fulfills $v_\alpha \approx 1.8 v_A$ for a typical ITER plasma, which allows a resonance with all harmonics of a TAE, the most fundamental being the $v_{\|} = v_A$ $(l = 1)$ and $v_{\|} = v_A/3$ $(l = 2)$ harmonic [129]. This is generally not true for other energetic ions in the tokamak, which for example emerge from external heating mechanisms like NBI (Neutral Beam Injection) [2]. An optimum of energy transfer between particle and wave is achieved, when the drift orbit width is comparable to the mode width. Due to the smaller finite orbit width of the resonant alpha particles, the toroidal mode numbers for ITER are expected to be high compared to present-day tokamak observations [22]. TAEs are often considered dominant modes with regards to the amount of particle transport they can cause. The reason for that is their comparatively low eigenfrequency, hence higher (potential) particle displacement per wave-particle energy transfer [135].

We need to consider distributions of energetic particles and how they themselves are affected by the interaction with the wave. A critical value is the slope of the distribution function. We consider a distribution function f with a monotonically decreasing velocity distribution $\partial f/\partial v$ as well as a monotonically decreasing radial distribution $\partial f/\partial r$. Such distributions are typical for energetic ions like fusion-product alpha particles.

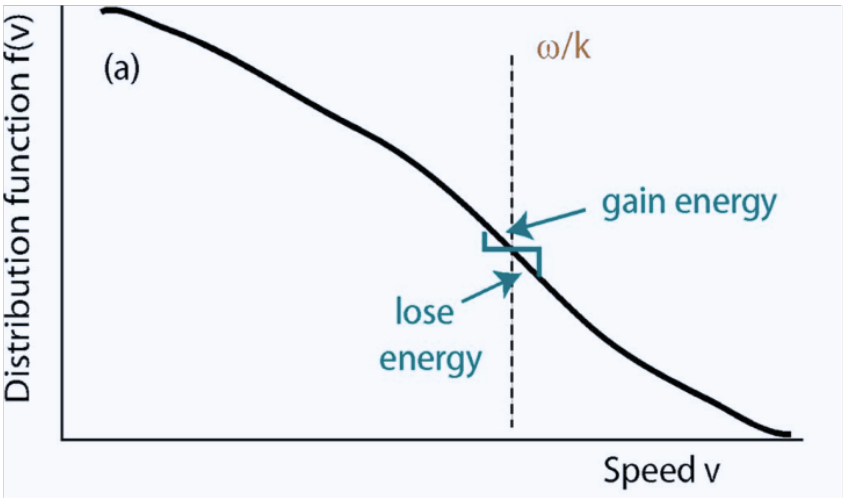

Figure 2.4: A sketch of the velocity distribution function $f(v)$ resonating with a mode with phase velocity ω/k. The amount of particles below the resonance velocity is larger and will be accelerated by the wave, which effectively causes a damping of the wave. The figure is taken and slightly modified from reference [129].

In figure 2.4 we see the energy distribution $f(v)$ in the presence of a mode with matching phase velocity. Particles with a velocity above the resonance lose part of their energy through the interaction and are slowed down towards the resonance velocity. The contrary is true for particles whose velocity is above the phase velocity ω/k. In a monotonically decreasing velocity distribution more particles are on the gaining side and the wave experiences a net energy loss, hence is damped. The driving force usually comes from a spatial gradient and can be understood from a similar consideration about the particle toroidal momentum p_ζ: This momentum is connected to the radial flux coordinate ψ via $p_\zeta \propto -\psi$. Hence, a particle resonating with a wave and delivering its toroidal momentum to it will transport the particle onto a flux surface that is radially further outwards. A resonance that draws energy from the wave to increase a particle's toroidal momentum will force the particle to move inwards. In a monotonically decreasing spatial distribution, there will always be more particles moving outwards, and these are the particles that provide energy to the wave. In general, the energy transfer can be shown to be proportional to

$$\gamma \propto \omega \frac{\partial f}{\partial v} + n \frac{\partial f}{\partial p_\zeta}.$$

Due to this redistribution, the resonance mechanism can not only drive modes unstable, but is also able to cause particle losses [136, 137] and has been observed in the past during various tokamak experiments [138, 139].

Particles in a toroidally confining plasma can pursue complicated orbits. As stated in the introduction, particles may be considered trapped or passing due to the poloidal variation of the magnetic field strength. Ubiquitous drifts can force particles to traverse complicated orbits, which is especially true for energetic particles as those can deviate strongly from the confining flux surfaces. The axisymmetry of a tokamak however, forces the drifting trajectories to eventually close in on them selves, which provides the confining property in the first place. When talking about resonating particles, it is the particle orbital motion in the tokamak that is pivotal to the interaction. The resonance occurs between the wave frequency and ω_θ and ω_{prec}, which are the poloidal bounce and the toroidal precession frequency respectively (see introduction). The requirement of needing to resolve particle orbits, together with the non-linear nature of the problem, often means that sophisticated numerical codes must be relied upon. Such a code used during this thesis is HAGIS (section 3.5).

2.4.1 Wave damping effects

While energetic particle species can act as a driving force onto plasma waves, the thermal plasma background generally opposes this driving force and acts to damp the wave. We briefly outline damping mechanisms that are important to the Alfvénic wave, most of which rely on a resonant absorption of the wave energy.

Landau damping Alfvén waves propagate along the magnetic field lines with the Alfvén velocity v_A, therefore a resonance interaction requires $v_{\|} = v_A = \omega k_{\|}$, for a parallel particle velocity $v_{\|}$. When a resonance condition between wave and particle is fulfilled, it is the slope of the velocity distribution function, that decides in which direction the energy transfer occurs. A negative slope $\partial f / \partial v < 0$ carries energy away from the wave and is known as Landau damping [21], see figure 2.4. A bump-on-tail distribution with locally positive slopes can lead to a linearly unstable system and is known as "inverse" Landau damping.

Ions: For typical tokamak plasmas, $v_{i,\|} \ll v_A$ holds, where $v_{i,\|}$ is the thermal ion velocity, hence only a small fraction of the ions are able to resonate with Alfvén modes. However, the magnetic field geometry alters the resonance condition by including both the toroidal and poloidal drift motion into the equation, resulting in an additional resonance at $v_{i,\|} = v_A/3$ [129]. It is expected [22, 134] to be the most significant damping mechanism for burning tokamak plasmas. Due to the resonance with the Maxwellian tail, it is exponentially sensitive to the ion temperature [22, 45, 46]. This is especially relevant for this work, since the ion temperature drops quickly in a tokamak disruption event 2.2.

Electrons: For typical tokamak electrons, $v_{e,\|} \gg v_A$ holds, where $v_{e,\|}$ is the thermal electron velocity. Only a small portion $v_{e,\|}/v_{e,\perp} \ll 1$ of the electron distribution can fulfil $\omega = k_{\|} v_A$ and partake in electron Landau damping [140]. However, at rational surfaces, i.e. at $q = m/n$, the Alfvén wave vector $k_{\|}$ (eq. (2.44)) becomes very small, allowing resonance with higher velocities $v_{e,\|}$. This resonance effect however occurs not at the exact location of the TAE gap ($q = m+1/2/n$), thus only radially extended TAEs are affected by this mechanism. Because electrons fulfilling $v_{e,\|}/v_{e,\perp} \ll 1$ are trapped, the collisions of trapped electrons with passing electrons and ions affect the damping, resulting in a mechanism called *trapped electron collisional damping* [141]. It relies on high collision rates of plasmas, i.e. which are cold or of high density. In this work the wave-particle interaction calculation takes place during the thermal quench of a plasma at temperature well above 1 keV. It will be addressed in section 5.1 and found generally negligible.

Radiative damping: With the inclusion of finite Larmor radius effects, the TAE is able to couple to a kinetic Alfvén wave (KAW). As the radially moving KAW carries energy away from the TAE, this effect is called radiative damping [142].

3 Numerical tools

In chapter 2 we introduced a multitude of complicated theories that would be necessary to carry out the work in this thesis. Due to the generally complex nature of the phenomena, analytical solutions are generally not feasible and hence one needs to rely on simulation tools to solve the problems numerically.

This chapter is concerned with the numerical tools that are applied throughout the thesis. References to more detailed and complete descriptions will be given at the beginning of each section. The order in which they are discussed corresponds to the order of their application in chapter 5.

Depicted in figure 3.1, is an overview of the numerical tools used throughout this thesis, with its respective physical purpose (purple), the input/output (red) and programming language (blue). The codes HELENA [143] and CHEASE [144] are only used as auxiliary codes for coordinate transformation of the VMEC-generated plasma equilibrium and hence not described in this thesis. ASCOT and DREAM were only used in paper B.

The role of each code in solving the problem laid out in section 1.1 is as follows: CODION (section 3.1) it utilized to calculate how the alpha particle species evolves in a disruption, which requires modeling the disruption (section 2.2), as well as solving the ion kinetic equation (eq. (2.15)). The disruption itself is accompanied by the induction of an electric field, which we calculate using the code GO (section 3.2) and use it as an input to solve the ion kinetic equation. The kinetic pressure and current density of the

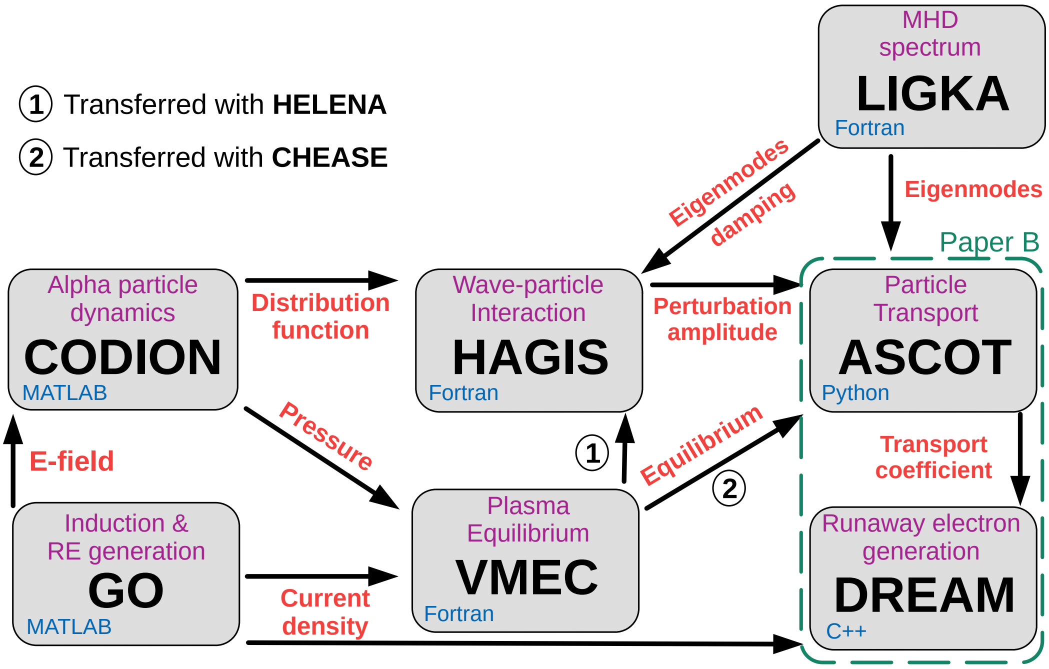

Figure 3.1: An overview of the numerical tools and their purpose.

plasma is used to reconstruct the plasma equilibrium with VMEC (section 3.3). The plasma equilibrium is examined with the LIGKA (section 3.4) code about its support of TAEs (section 2.3.2) and damping rates (section 2.4.1). The wave-particle interaction (section 2.4) of alphas with TAEs is calculated by the tool HAGIS (section 3.5), yielding the perturbation evolution of TAEs. With ASCOT (section 3.6), the runaway electron transport in the perturbed equilibrium is estimated. Under the influence of this RE transport, the runaway electron generation (section 2.1.2) is analyzed with the code DREAM (section 3.7).

3.1 CODION - calculation of the alpha particle distribution

CODION [53] (COllisional Distribution of IONs) is a non-relativistic, linearized Fokker-Planck solver developed to conduct calculations for ion runaway studies. In section 4.1 this code is adapted to calculations with fusion-born alpha particles during plasma thermal quenches. It is originally built upon previously existing analytical models [54] and is generally valid for the cases of fusion-relevant electric field strengths and trace impurities.

The CODION tool solves for an ion distribution function, whose evolution is dictated by an electric field and by small-angle Coulomb collisions with background Maxwellian distributions. It is written for an infinite, homogeneous plasma with straight field line geometry and averages over the particle gyro-motion. The coordinate system is spanned by (v, ξ) which are defined such, that the parallel particle velocity $v_\parallel$ aligns with the magnetic field lines and the pitch is $\xi \equiv v_\parallel / v$ with the particle velocity $v = |\mathbf{v}|$. The strength of the parallel electric field ($E_\parallel \parallel v_\parallel$) can vary in time. Collisions are treated with a linearized collision operator, which is valid for an ion species, whose density is sufficiently small compared to the plasma background. The kinetic equation that CODION solves is written in the Fokker-Planck approximation (section 2.1) and yields for the evolution of an ion distribution f_i:

$$\frac{\partial f_\mathrm{i}}{\partial t} + \frac{Z_i e}{m_i} E^* \left(\xi \frac{\partial}{\partial v} + \frac{1 - \xi^2}{v} \frac{\partial}{\partial \xi} \right) f_\mathrm{i} = \sum_b \mathcal{C}_\mathrm{FP}\{f_\mathrm{i}, f_b\}, \tag{3.1}$$

with an effective electric field E^* (see below) and the Fokker-Planck collision operator $\mathcal{C}_\mathrm{FP}$ describing collisions with a multitude of background species b. The collision operator contains the energetic particle operator $\mathcal{C}_\mathrm{EP}$ (eq. (2.3)), as well as an operator for ion-electron collisions and ion-ion collisions. Self-collisions can be included, but are generally not important for the small density populations.

The electric field $E_\parallel$ is defined such that electrons are accelerated in negative velocity direction and ions in positive velocity direction. Because of the mass ratio, electrons are accelerated faster than the ions, which allows the assumption that the electron population is perpetually in steady state and has a distribution part that is drifting from its thermal equilibrium due to being accelerated. The interaction of the drifting electron population and the ions f_i can (due to the quasi steady-state assumption) be written in terms of a friction and absorbed into the electric field, yielding the effective electric field $E^* = (1 - Z_i/Z_\mathrm{eff})E_\parallel$. When the plasma is pure ($Z_i = Z_\mathrm{eff}$) no net acceleration on the ions occurs, as the electron friction cancels perfectly. The presence of neutrals and impurities causes a finite effective electric field to remain and, depending on Z_i, light impurities ($Z_i < Z_\mathrm{eff}$) get accelerated in positive direction, while heavy impurities are accelerated towards negative direction, i.e. with the electrons [53]. Effects of Bremsstrahlung and synchrotron emission losses of the alphas are neglected and justified by the non-relativistic approach.

The distribution function $f_\mathrm{i}(v,\xi)$ is discretized in velocity and expanded in Legendre polynomials [53] for the pitch-angle variable. Time integration is performed with a first order implicit scheme which allows a time-variation of electric field and background plasma parameters. Details about boundary conditions and implementation can be found in reference [53], while convergence tests are found in the thesis of O. Embreus [145].

Using CODION, we will be able to calculate an alpha particle distribution undergoing a thermal quench for the ITER tokamak (section 5.2.1 and section 4.1) and use it as the particle species in the wave-particle interaction process, as has been done in paper A [78]. For paper B [79] an analytical alpha particle model was developed and validated against CODION, the details of which will be discussed in section 4.1.

3.2 GO - computation of the current density and electric field evolution

GO [107, 146, 147] was developed for calculations of plasma cooling, runaway current and electric field evolution. It is a 1D spatial model, capable of self-consistently calculating the temperature evolution of each species through an energy balance equation, that includes the effects of Ohmic heating, line radiation, bremsstrahlung, ionization/recombination rates and collisional energy exchange. A conducting plasma vessel [146, 148] is part of the model, however magnetic coils are not included. Every species calculation is advanced separately due to the different collision time scales. The evolution of the electric field E is obtained by solving the induction equation in 1D with a term for radial diffusion of the E-field

$$\frac{1}{r}\frac{\partial}{\partial r}\left(r\frac{\partial E}{\partial r}\right)=\mu_0\frac{\partial}{\partial t}\underbrace{(\sigma_{\|}E+n_{\mathrm{RE}}ec)}_{j}, \tag{3.2}$$

where j is the current density, r is the radial coordinate, c the speed of light, e the electron charge, μ_0 the magnetic vacuum permittivity, $\sigma_{\|}$ the parallel (Spitzer) conductivity with neoclassical corrections [1] and n_{RE} the runaway electron number density. This model inherently assumes E to act only parallel to the magnetic field and also that every runaway electron that is generated, instantly travels at the speed of light. For a GO application on plasma disruptions, the electric field mainly evolves due to changes of the conductivity $\sigma_{\|}\propto T_e^{3/2}$. The electric field then may generate runaway electrons through primary mechanisms (Dreicer, hot-tail) [1] and the secondary mechanism (avalanche), evolving the radial density profile $n_{\mathrm{RE}}(r)$ of the REs. The current density is found on the RHS of equation (3.2) and separated into the Ohmic current and the runaway current.

GO is used in this thesis to calculate the current density profile $j(r)$ (section 5.1) and the induced electric field evolution (section 5.2.1) during an ITER disruption. The GO code has been superseded by the recently developed and higher-fidelity code DREAM (section 3.7), but at the beginning of this project, DREAM was not yet available.

---

[1] The tool is now implemented with tritium beta decay and inverse Compton scattering sources, but not in the version used for this thesis.

3.3 VMEC - determining the plasma equilibrium

VMEC [149, 150] (Variational Moments Equilibrium Code) is a tool widely used to obtain plasma equilibria for fusion devices. It is formulated in the MHD framework and seeks a solution to a magnetic field $\mathbf{B}$, that fulfills the force balance equation

$$-\mathbf{j} \times \mathbf{B} + \nabla \mathbf{p} = 0,$$

while simultaneously obeying Ampere's law $\nabla \times \mathbf{B} = \mu_0 \mathbf{j}$ and Gauss's law $\nabla \cdot \mathbf{B} = 0$ for a current $\mathbf{j}$ and a pressure $\mathbf{p}$. The solution is found via an energy principle, where the total (magnetic and thermal) energy E_p of the system is minimized for a toroidal domain Σ:

$$E_p = \int_\Sigma \left(\frac{1}{2} |\mathbf{B}|^2 + |\mathbf{p}| \right) \mathrm{d}V.$$

The minimization of the energy E_p is approached through the steepest-descent method while conserving a (prescribed) magnetic flux (or toroidal current). For an application onto tokamaks, the main required input consists of a current density profile, a pressure profile and an initial guess for the location of the magnetic axis. The result is cast in flux coordinates (ψ, θ, ζ), where ψ is the flux coordinate corresponding to a radius, θ the poloidal and ζ the toroidal angle (see figure 1.1). The surfaces are described via Fourier harmonics in the angles. Two boundary conditions for Ψ are required to obtain a unique solution. The inner boundary condition is fixed through a specification of Fourier components, which requires the poloidal harmonics at the magnetic axis, $\Psi = 0$, to vanish and the toroidal Fourier components are required to be 2π-periodic. A second boundary condition on Ψ must be imposed on the plasma edge and can be chosen to be free or fixed. The free boundary is treated with the inclusion of a vacuum magnetic field which must be obtained through the external coil configurations. The fixed boundary condition used for the application in this thesis assumes normal vectors to vanish on the last closing flux surface and provides thus a specification of Fourier components.

3.4 LIGKA - obtaining mode structures and mode damping rates

LIGKA [151, 152] (LInear GyroKinetic shear Alfvén physics) was developed to calculate the kinetic effects of energetic particles on MHD modes. It is based around the gyrokinetic model found in reference [153] and specified to the shear Alfvén frequency regime (see section 2.3.1), i.e. frequencies well below the ion cyclotron frequency. LIGKA solves a system of linearized gyrokinetic equations and obtains the eigenvalues (frequency and damping) as well as the eigenfunctions (mode structures) of the system. Being a gyrokinetic model, it provides a background plasma description with the inclusion of finite Larmor radius and orbit width effects. A condensed introduction and discussion of the current state of the code is provided in reference [154] and will be followed here, while exact details about mentioned quantities and the numerical implementation is found in references [130, 155].

The system of equations is invoked from the parallel Ampere's law $[\nabla \times (\nabla \times \mathbf{A})]_\parallel = \mu_0 j_\parallel$ and the quasi-neutrality condition $\sum_b Z_b n_b = 0$ for particle species $b = \mathrm{e}, \mathrm{i}$, which includes electrons e and ions i. The guiding center distribution functions $f_b = f_{\mathrm{eq},b} + \delta f_b$ are perturbed, causing fluctuations in the number densities δn_b and current densities

δj_b, allowing to state the quasi-neutrality condition of gyrokinetics:

$$\sum_b Z_b \int \mathrm{d}^2 v \{J_0 \delta f\}_b + \sum_{\mathrm{i}} \left(m_i \nabla_\perp \cdot \frac{n_i \nabla_\perp \delta\phi}{B^2} + \frac{3P_{i\perp}}{4B^2\Omega_i^2} \nabla_\perp^4 \delta\phi \right) = 0 \tag{3.3}$$

with the gyro-average operator J_0, $\delta\phi$ is the perturbed electrostatic potential and Ω is the gyrofrequency. Similarly, the gyrokinetic momentum equation can be stated from Ampere's law:

$$\begin{aligned}
&-\frac{\partial}{\partial t}\left[\nabla \cdot \frac{\nabla_\perp \delta\phi}{v_A^2}\right] + \mathbf{B} \cdot \nabla \frac{\nabla \times (\nabla \times \delta A_\| \mathbf{b})}{B} + (\mathbf{b} \times \nabla \delta A_\|) \cdot \nabla \frac{\mu_0 j_\|}{B} = \\
&-\sum_b \mu_0 \int \mathrm{d}^2 v Z_b \{\mathbf{v}_d \cdot \nabla J_0 \delta f\}_b + \sum_i \left[\mathbf{b} \times \nabla \left(\frac{\beta_{i\perp}}{2\Omega_i}\right)\right] \cdot \nabla \nabla_\perp^2 \delta\phi + \\
&\sum_i \frac{3\beta_{i\perp}}{8\Omega_b^2} \nabla_\perp^4 \frac{\partial \delta\phi}{\partial t} + \mathbf{B} \cdot \nabla \frac{1}{B} \sum_i \frac{\beta_b}{4} \nabla_\perp^4 \delta A_\|,
\end{aligned} \tag{3.4}$$

where $\beta_{b\perp}$ is the plasma beta for the perpendicular pressure component and $\mathbf{b}$ is a unity vector in the direction of the magnetic field $\mathbf{B}$. Using the linear gyrokinetic equation

$$\begin{aligned}
\frac{\partial \delta h}{\partial t} + (v_\| \mathbf{b} + \hat{\mathbf{v}}_d) \cdot \nabla \delta h = &\left[\frac{\mathbf{b} \times \nabla f_{\mathrm{eq}}}{eB} \cdot \nabla - \frac{\partial f_{\mathrm{eq}}}{\partial E} \frac{\partial}{\partial t}\right] \\
&\times J_0 \left[\delta\phi - \left(1 - \frac{\hat{\mathbf{v}}_d \cdot \nabla}{i\omega}\right) \delta\phi\right],
\end{aligned} \tag{3.5}$$

with the drift velocity $\hat{\mathbf{v}}_d = -\mathbf{b}/(eB) \times \left(m v_\|^2 (\mathbf{b} \cdot \nabla)\mathbf{b} + \mu \nabla B\right)$, the perturbed part of the guiding center distribution functions evolve as

$$\delta f_b = \delta h_b + \frac{\partial f_{\mathrm{eq},b}}{\partial E} Z_b J_0(\rho k_\perp) \left[\delta\phi - \delta\psi - \frac{v_\| k_\|}{\omega} \delta\psi\right] + \frac{\nabla f_{\mathrm{eq},b}}{i\omega B} \cdot (\mathbf{b} \times \nabla) J_0 \delta\psi. \tag{3.6}$$

where h is the non-adiabatic part of the distribution function. Solving equations (3.3)-(3.6) yields the eigenvalues and the eigenfunctions of the perturbed electrostatic potential $\delta\phi(\mathbf{x})$ and the perturbed magnetic potential $\partial_t \delta A_\|(\mathbf{x}) = -\mathbf{b} \cdot \nabla \delta\phi(\mathbf{x})$. These solutions account for the mode structures as well as the mode damping, which includes electron and ion Landau damping, continuum damping and radiative damping (see section 2.4.1).

The real space vector $\mathbf{x}$ is discretized into finite radial elements and Fourier-decomposed into toroidal harmonics n and poloidal harmonics m. While LIGKA can be coupled to HAGIS (see next section) to numerically calculate particle orbits, it is often feasible to use the analytical "fast-circulating" approximation [130], which neglects the effects of trapped particles. This underestimates electron Landau damping effects in regions that are distant from rational surfaces and can be partially addressed with the inclusion of *trapped electron collisional damping*, of which analytical formulae exist [141].

The influence of energetic particles on eigenvalues and eigenfunctions can enter via the pressure tensor P_i. However, workflows with the HAGIS code (see next section) have been established (see e.g. the thesis of T. W. Hayward-Schneider [128] or the thesis of M. Schneller [156]), where the EPs are treated with a drift-kinetic model. LIGKA is also part of the ITER Integrated Modelling and Analysis Suite (IMAS [157]), designed to provide a standardized workflow and database for ITER research and operation.

3.5 HAGIS - calculation of the wave-particle interaction

The HAGIS code [158] was developed to calculate the interactions between an ensemble of energetic particles and a spectrum of MHD waves specific to toroidal plasmas. Its model constitutes a non-linear, drift-kinetic, perturbative, particle-in-cell description. It has already been applied to research of alpha-particle driven Alfvénic modes in the quiescent ITER plasma [22]. Here, the code's model is briefly introduced, closely following the descriptions of S. Pinches [134] and T. W Hayward-Schneider [128], where exact details can be found.

The original idea of HAGIS is to derive the wave evolution by variation of the system Lagrangian

$$\mathcal{L}_{\mathrm{sys}} = \mathcal{L}_{\mathrm{EP}} + \mathcal{L}_{\mathrm{int}} + \mathcal{L}_{\mathrm{w}}, \tag{3.7}$$

where $\mathcal{L}_{\mathrm{EP}}$ describes the equilibrium energetic particle energy, $\mathcal{L}_{\mathrm{int}}$ the energy exchange between the waves and the particles and $\mathcal{L}_{\mathrm{w}}$ the electromagnetic energy component of the waves supported by the background plasma[2]. Through the interaction Lagrangian $\mathcal{L}_{\mathrm{int}}$ a wave-particle non-linearity is maintained.

The guiding centre Lagrangian of a gyrating particle [159] reads

$$\begin{aligned}\mathcal{L}_{\mathrm{EP}} &= e\mathbf{A}^* \cdot \dot{\mathbf{x}} + \frac{m\mu}{e}\dot{\xi} - \mathcal{H},\\ \mathcal{H} &= \frac{1}{2}mv_{\|}^2 + \mu B + e\phi\end{aligned}$$

with the modified vector potential $\mathbf{A}^*$, the guiding-center velocity $\dot{\mathbf{x}}$, the magnetic moment μ, the gyro-phase ξ, the particle Hamiltonian $\mathcal{H}$ and the electrostatic potential $\phi(\mathbf{x}, t)$. The electromagnetic potential is perturbed by $\tilde{\mathbf{A}}$ and the equations are cast in the Boozer coordinate system [160] (ψ, θ, ζ). The following canonical variables are identified:

$$\begin{aligned}P_\theta &= \rho_{\|} I + \Psi + \tilde{A}_\theta,\\ P_\zeta &= \rho_{\|} g - \psi + \tilde{A}_\zeta,\\ P_\xi &= \mu,\end{aligned}$$

where $\rho_{\|} = v_{\|}/\omega_g$ is a parallel ion gyro-radius, I the toroidal curent, Ψ the toroidal flux and g the poloidal current. From the canonical variables, the EP guiding center equations of motion in an electromagnetic potential can be derived. With the assumption that the electromagnetic potential is perturbed by a shear Alfvénic wave, the perturbed vector potential $\tilde{\mathbf{A}}$ can be simplified with $\delta B_{\|} = 0$ and $E_{\|} = 0$, though the latter restriction is lifted in reference [156], but not used in this thesis. A set of 4 first order differential equations $(\dot{\psi}, \dot{\theta}, \dot{\zeta}, \dot{\rho}_{\|})$ for each particle emerges. For the code to be feasible, particles are replaced by weighted markers representing distinct phase space volumes of energetic particle distributions.

In HAGIS, the plasma is in a (force) equilibrium to which the Alfvénic wave structures are understood as a perturbative superposition $\tilde{\phi}$. The spatial structure of each wave k is Fourier-decomposed into poloidal m and toroidal n harmonics

$$\tilde{\phi}_k(t) = A_k(t)\mathrm{e}^{-i\sigma_k(t)} \sum_m \tilde{\phi}_{km}(\psi)\mathrm{e}^{i(n_k\zeta - m\theta - \omega_k t)}, \tag{3.8}$$

---

[2] More precisely, the wave Lagrangian is $\mathcal{L}_{\mathrm{w}} = \mathcal{L}_{\mathrm{bulk}} + \mathcal{L}_{\mathrm{em}}$, where the bulk plasma influence on the waves $\mathcal{L}_{\mathrm{bulk}}$ and electromagnetic contribution $\mathcal{L}_{\mathrm{em}}$ is treated separately, but here glanced over for simplicity.

where A_k is the perturbation amplitude, σ_k is the mode phase, ω_k is the mode eigenfrequency and $\tilde{\phi}_{km}$ is a fixed linear eigenfunction, e.g. obtained through LIGKA (section 3.4). Since LIGKA is written in straight field line coordinates (PEST coordinates [161]) and HAGIS in the Boozer coordinate system, a transformation takes place that is handled by HAGIS itself. Only $A_k(t)\mathrm{e}^{-i\sigma_k(t)}$ is allowed to evolve in time and can only change slowly compared to the wave eigenfrequency. For a total number of waves N_w the wave Lagrangian reads

$$\mathcal{L}_\mathrm{w} = \sum_{k=1}^{N_w} \frac{E_k}{\omega_k} \left[A_k^2 \dot{\sigma}_k \right], \tag{3.9}$$

with the wave energy

$$E_k = \frac{1}{2\mu_0} \int_V |\nabla_\perp \tilde{\phi}_k|^2 / v_A^2 \mathrm{d}^3 x.$$

The last Lagrangian required for eq. (3.7) is the interaction Lagrangian $\mathcal{L}_\mathrm{int}$. For a number of markers N_p with velocities $\mathbf{v}$ it can be stated as

$$\mathcal{L}_\mathrm{int} = \sum_{j=1}^{N_p} \left(\tilde{\mathbf{A}}_j \cdot \mathbf{v}_j - \tilde{\phi}_j \right), \tag{3.10}$$

where the subscript j describes the quantities to be evaluated at the spatial location of the particle j. The subscript k for $\tilde{\mathbf{A}}$ and $\tilde{\phi}$ is dropped, as the contributions from each wave present along the particle trajectory must be included.

It is useful to reformulate the perturbation amplitude in terms of its real and imaginary parts

$$A_k(t)\mathrm{e}^{-i\sigma_k(t)} = \mathcal{X}_k(t) - i\mathcal{Y}_k(t). \tag{3.11}$$

For a total of N_w waves, the perturbed potential at the jth particle position becomes

$$\tilde{\phi}_j(t) = \sum_{k=1}^{N_w} \sum_m \left[\mathcal{X}_k(t) C_{jkm} + \mathcal{Y}_k(t) S_{jkm} \right], \tag{3.12}$$

where

$$C_{jkm} \equiv \mathrm{Re} \left[\tilde{\phi}_{km}(\psi_j) \mathrm{e}^{i\Theta_{jkm}} \right],$$
$$S_{jkm} \equiv \mathrm{Im} \left[\tilde{\phi}_{km}(\psi_j) \mathrm{e}^{i\Theta_{jkm}} \right],$$

with $\Theta_{jkm} = n_k \zeta_j - m\theta_j - \omega_k t$. With this formulation, the interaction Lagrangian can be rewritten as

$$\mathcal{L}_\mathrm{int} = \sum_{j=1}^{N_p} \sum_{k=1}^{N_w} \frac{1}{\omega_k} \sum_m (k_{\|m} v_{\|j} - \omega_k) \left[\mathcal{X}_k C_{jkm} + \mathcal{Y}_k S_{jkm} \right], \tag{3.13}$$

where only the parallel velocity $v_\|$ of the particle is relevant reflecting on the shear nature of Alfvénic waves.

Finally, varying $\mathcal{L}_\mathrm{int} + \mathcal{L}_\mathrm{w}$ with respect to $\mathcal{X}$ and $\mathcal{Y}$ one can obtain the wave equations

$$\dot{\mathcal{X}}_k = \frac{1}{2E_k} \sum_{j=1}^{N_p} \sum_m (k_{\|m} v_{\|j} - \omega_k) S_{jkm}, \tag{3.14}$$

$$\dot{\mathcal{Y}}_k = -\frac{1}{2E_k} \sum_{j=1}^{N_p} \sum_m (k_{\|m} v_{\|j} - \omega_k) C_{jkm}. \tag{3.15}$$

where the resonance condition is illustrated by the term $(k_{\|m} v_{\|j} - \omega_k)$.

HAGIS solves equations 3.14 and 3.15 with the particle information provided, that is initialized by the user and evolved by the EP equations of motion. Only particle nonlinearities are retained as the EP description enters and is evolved via a drift-kinetic model, but the waves enter the model as pre-calculated modes, whose structure (and damping) cannot be evolved.

3.6 ASCOT5 - computation of the alpha particle transport

ASCOT5 [162, 163] is an orbit-following code that performs Monte-Carlo simulations on test-particles inside a perturbed plasma equilibrium. It is able to calculate particle transport effects caused by magnetic perturbations and was purposed to study fast ion losses for ITER [164].

The Fokker-Planck equation is not solved directly, but with a statistical approach revolving around a *test-particle orbit-following Monte Carlo method* [165, 166]. Within the test-particle model, the test-particles do not affect the enclosing systems and as such the collision operator is linear. The method of orbit-following approximates a particle distribution function f with a distribution of markers, whose equations of motion are described by the Langevin equation. With the Langevin equation a stochastic element (via the *Wiener process*) enters and a Monte Carlo method [165, 166] is used to solve the stochastic differential equation. For a reduction of complexity, the guiding center motion can be solved for instead of the full orbit particle motion.

ASCOT5 is a multi-purpose tool which is able to calculate impurity migration, fast ion losses and runaway electron transport in realistic magnetic confinement devices (tokamak and stellerator) [126, 127, 167]. In this work, it will only see a brief appearance, with the purpose of estimating the transport of runaway electrons caused by magnetic perturbations. For this, the particle position $\mathbf{x}$ of each marker is tracked and from it a diffusion coefficient is calculated as $D = \text{var}[(\Delta\mathbf{x})]/2t$ via the position variance var over time t.

3.7 DREAM - self-consistent simulation of a plasma disruption and runaway electron generation

The Disruption Runaway Electron Analysis Model (DREAM [105, 168, 169]) is a high fidelity code developed for self-consistent calculations of the plasma evolution during a disruption event in axisymmetric geometry. Changes to global plasma parameters are coupled to the generation and transport of RE particles. The bulk of the plasma is treated with a combination of fluid models. These capture the evolution of electron and ion temperatures, the toroidal electric field, the particle densities and charge stages and the poloidal flux, which sets the current density. For an accurate description of the REs, a kinetic treatment can be employed. Alternatively, the REs can be treated as a fluid species, which is characterized solely by their current density. Advection-diffusion coefficients can be prescribed to the equations governing the runaway electron motion. We will use this feature to determine RE growth in the presence of transport caused by TAEs.

DREAM supports analytically prescribed, static 2D magnetic field geometries in the Miller parametrization [170]. It assumes nested flux surfaces, that can be fully parametrized by the major radius of the magnetic axis, elongation, Shafranov shift, triangularity and a poloidal flux profile. Except for the major radius, all quantities can be given as a function of radius.

The kinetic equation for the electron distribution f_e in phase space is of the form of a general advection-diffusion equation

$$\frac{\partial f_e}{\partial t} = \frac{\partial}{\partial \mathbf{z}} \cdot \left(-\mathbf{A} f_e + D \cdot \frac{\partial f_e}{\partial \mathbf{z}} \right) + S(\mathbf{z}), \tag{3.16}$$

where $\mathbf{z}$ are (1D+2P) phase-space coordinates, $\mathbf{A}$ is the advection vector, D is the diffusion and S is a source and sink term. The phase space advection

$$\mathbf{A} = \mathbf{A}_E + \mathbf{A}_C + \mathbf{A}_B + \mathbf{A}_S + \mathbf{A}_T$$

describes the effects of electric field acceleration ($\mathbf{A}_E$), collisional friction ($\mathbf{A}_C$), bremsstrahlung radiation reaction forces ($\mathbf{A}_B$), synchrotron ($\mathbf{A}_S$) radiation reaction forces and radial transport ($\mathbf{A}_T$). Similarly, the diffusion

$$D = D_C + D_T$$

captures the effects of collisional momentum-space diffusion (D_C) and radial diffusion (D_T). The source

$$S = S_{\text{ava}} + S_p$$

describes the runaway avalanche process (S_{ava}) and additional particle sources (S_p) for electron density variations, originating e.g. due to ionization-recombination processes. The collisional terms D_C and $\mathbf{A}_C$ encompass a fully relativistic, Fokker-Planck electron-electron test-particle collision operator. Collisions with ions assume stationary targets of infinite mass and follow a model presented in reference [171], which takes into account the effects of partial ionization. Orbit effects in tokamaks are captured via *bounce-averaging* [168], which accounts for the qualitatively different behavior of particles that are passing and particles that are trapped. Explicit forms of $\mathbf{A}$ and D, as well as their bounce-averaged components can be found in the original reference [168].

While DREAM can evolve the fully kinetic equation (3.16), it also supports the solution of simplified equations, which often provide adequate results but at significantly reduced computational costs. One such approximation treats the thermal populations and the runaway electrons as a fluid, similar to GO (section 3.2). Here, the energy spectrum of the runaway tail is not resolved and the focus lies on the RE generation rate.

In the fully fluid mode, the thermal electron population is defined via their density n_e, temperature T_e and Ohmic current j_Ω, calculated via

$$\frac{j_\Omega}{B} = \sigma \frac{\langle \mathbf{E} \cdot \mathbf{B} \rangle}{\langle B^2 \rangle},$$

where $\langle \cdot \rangle$ denotes a spatial flux average and σ is the parallel electric conductivity that is implemented from the Sauter-Redl model [172], accounting for neoclassical effects at arbitrary collisionality. The runaway electron fluid is characterized by its number density n_{re} and runaway current density j_{re}. The former evolves as [168]

$$\frac{\partial \langle n_{re} \rangle}{\partial t} = \left(\frac{\partial \langle n_{re} \rangle}{\partial t} \right)_{\text{fluid}} + \frac{1}{V'} \frac{\partial}{\partial r} \left[V' \left(A_{\text{re}} \langle n_{\text{re}} \rangle + D_{\text{re}} \frac{\partial \langle n_{re} \rangle}{\partial r} \right) \right], \tag{3.17}$$

where $(\cdot)_{\text{fluid}}$ is the fluid-model runaway generation rate, V' is the spatial Jacobian and A_{re} and D_{re} are the transport coefficients, that can be prescribed as functions of time, radius and momentum. Note that for the application of momentum-dependent transport coefficients, one has to assume some momentum-space distribution function ($f(p)$) for the REs (even in fluid mode) and this will be done in section 5.4.

The runaway generation rate of the fluid model includes the following types of generation mechanism (see section 2.1.2):

$$\left(\frac{\partial\langle n_{\text{re}}\rangle}{\partial t}\right)_{\text{fluid}} = \left(\frac{\partial\langle n_{re}\rangle}{\partial t}\right)_{\text{S}} + \left(\frac{\partial\langle n_{\text{re}}\rangle}{\partial t}\right)_{\text{dreic}} + \left(\frac{\partial\langle n_{\text{re}}\rangle}{\partial t}\right)_{\text{HT}},$$

with $(\cdot)_{\text{dreic}}$ the Dreicer rate (using a neural network trained on full kinetic calculations [99]), $(\cdot)_{\text{HT}}$ the hot-tail seed calculated with a model presented in references [105, 168] and $(\cdot)_{\text{S}}$ is used to account for avalanching, Compton scattering and tritium decay sources. The rate is given as [168]

$$\left(\frac{\partial\langle n_{re}\rangle}{\partial t}\right)_{\text{S}} = 4\pi\int_0^\infty p^2\langle S\rangle_\xi(p)\text{H}(p-p_{\text{crit}})$$

where $\langle\cdot\rangle_\xi$ denotes the combined flux surfaces and pitch average, S is the particle source and $\text{H}(x)$ is the Heaviside step function, birthing particles at the critical momentum p_{crit} (see section 2.1.2). The source function for Compton and tritium decay seed sources is modelled as in references [106, 107] and the avalanche source function [168] accounts for particle screening effects. The runaway electrons generated contribute to the runaway current density via

$$\frac{j_{\text{re}}}{B} = \frac{ec\langle n_{\text{re}}\rangle}{\langle B\rangle},$$

where we assume that every runaway electron travels at the speed of light c.

The background fluid species is defined by a density n_i^j for each species i and charge state j. Equations for their spatial evolution can be written with a one-dimensional transport equation that is structurally similar to the kinetic equation (3.16), but only evolves in time t and radial coordinate r (missing the momentum variables). The charge stages are evolved self-consistently with ionization and recombination rate coefficients extracted from the OpenADAS database [173] and accounting for Lyman opacity effects upon recombination [10].

4 Code development

For paper A [78], code development had to be conducted on CODION (section 3.1) and HAGIS (section 3.5) and is presented in this chapter. The purpose of paper A was to conduct a proof-of principle study on post-disruption TAEs driven by alpha particles. This requires an answer to the questions about (1) the alpha particle evolution in a disruption, (2) the support of post-disruption modes (TAEs) by the equilibrium, (3) the wave-particle interaction between alphas and TAEs and finally (4), the question if runaway electron transport can actually be caused by the TAEs. For simplicity, we used and adjusted built-in modules and diagnostics, which this chapter is about. Paper A eventually found question (4) to be positively answered, hence an extended follow-up study was launched, resulting in paper B [79] and constituting the contents of chapter 5. This chapter describes the tool development necessary for the project, while chapter 5 focuses more on the results.

CODION is equipped with a fusion source [78] to self-consistently calculate alpha particle distributions in a burning tokamak plasma (section 4.1). Two instances of HAGIS application are conducted: (1) the calculation of the TAE mode drive caused by fusion-born alphas (section 4.2.1) and (2) the transport of runaway electrons caused by TAEs (section 4.2.2). Application (1) requires the import of CODION-calculated alpha distributions and (2) required a relativistic extension of the equation of motions. The relativistic extension is presented in paper A, which was originally derived by S. Braun and thus not presented in this thesis.

4.1 Alpha particle distribution calculation with CODION

The Fokker-Planck solver CODION was originally developed for the purpose of ion runaway studies and introduced as such in section 3.1. For the treatment of alpha particles as the fast ion species, it has been implemented with a fusion source S_α and used throughout paper A [78].

The Fokker-Planck equation (3.1) was adjusted for a distribution of fusion-born alpha particles f_α, yielding

$$\frac{\partial f_\alpha}{\partial t} + \frac{Z_\alpha e}{m_\alpha} E^* \left(\xi \frac{\partial}{\partial v} + \frac{1-\xi^2}{v} \frac{\partial}{\partial \xi} \right) f_\alpha = \sum_b \mathcal{C}_{\mathrm{FP}}\{f_\alpha, f_b\} + S_\alpha. \tag{4.1}$$

The alpha source S_α can be described [88] as a Gaussian distribution in energy and reads

$$S_\alpha(E) = S_0 \exp\left(-\frac{5}{16} \frac{(E - E_{\alpha 0})^2}{T_i E} \right), \tag{4.2}$$

with the ion temperature T_i, the alpha particle birth energy $E_{\alpha 0} = 3.5\,\mathrm{MeV}$, the source strength S_0 and the factor 5/16 accounts for a transformation from the fusion reaction center-of-mass frame to the lab frame according to H. Brysk [88]. The source strength is defined as

$$S_0 = n_\mathrm{D} n_\mathrm{T} \langle \sigma v \rangle,$$

describing the fusion of deuterium and tritium with a respective particle density of n_{D} and n_{T} and with $\langle\sigma v\rangle$, where σ is the cross-section. It can be approximated as [174]:

$$\langle\sigma v\rangle = 3.68 \cdot 10^{-18}\, T_i^{-2/3} \exp\{-19.94\, T_i^{-1/3}\} \ \mathrm{m}^{-3}\mathrm{s}^{-1}.$$

Because the source is isotropic and because the distribution is resolved in pitch by a Legendre mode decomposition, the fusion source is implemented to only act on the lowest Legendre mode.

CODION is built around a linearized Fokker-Planck collision operator $\mathcal{C}_{\mathrm{FP}}$ and the total distribution function f_α is treated as a superposition of a Maxwellian $f_{\alpha,\mathrm{M}}$ and an energetic part $f_{\alpha,\mathrm{EP}}$. A non-monotonic grid is implemented, that maps the velocity grid variable v onto a new grid $y = v^2 + gv$, with a small grid parameter variable $g \sim \mathcal{O}(10^{-3})$. This way, the more densely populated bulk and the sparsely populated energetic tail can be resolved efficiently.

Figure 4.1a) shows the CODION computation of alpha particles being created and distributed in velocity space for representative tokamak plasma conditions. Initially, only $f_{\alpha,\mathrm{M}}$ is present, as is necessary for the linearized collision operator. The width of its Maxwellian distribution corresponds to the background plasma temperature of 10 keV, which is equal for ions and electrons. From $t = 0$ on the fusion term S_α is initiated, producing energetic alpha particles, that emerge isotropically at $v = \pm v_{\alpha 0} = \pm\sqrt{2E_\alpha/m_\alpha}$ and begin slowing-down due to Coulomb collisions with the background plasma (self-collisions are neglected). The analytical steady-state solution f_0 (eq. (2.16)) is approached by the energetic tail and matched after approximately one second to a good degree. The temperature of the plasma steers not only the rate at which the alpha particles are born, but also the collision process and changes the shape of the (energetic) distribution via τ_s (eq. (2.10)) and v_c (eq. (2.12)). The effect of velocity spreading at the birth velocity $v_{\alpha 0}$, that is described in CODION by eq. (4.2) is not captured by the unit step-function in the analytical solution, but will be addressed further down in this section as well as in the analytical model in section 5.2.2. Since CODION does not include a particle sink, the alphas, that slow down, begin piling up at the origin and progressively increase the number density $n_\alpha = 4\pi \int f_{\alpha,\mathrm{M}} \mathrm{d}v$. Since this would dilute the fuel plasma density $n_{\mathrm{D}} + n_{\mathrm{T}}$ indefinitely (quasi-neutrality requirement) and reduce the source strength, we assume the fuel density to remain constant and the alpha density is generally not taken into account for the computation of S_0. In a tokamak, the removal of cold alpha particles - the Helium ash problem [89] - will be addressed for the same reason, which is to avoid dilution. As we will see later, we are only interested in the energetic tail of the distribution hence neglect an accurate treatment of the Maxwellian.

Shown in figure 4.1b) is an alpha distribution function $f_\alpha(v, \xi)$ that is accelerated in positive velocity direction through a constant electric field $\mathbf{E} \parallel v_\parallel$ of the magnitude $E = 3\,\mathrm{V/m}$. In addition to collisional slowing-down and electric field acceleration, one can see the effects of the pitch-angle scattering process, which seeks to restore the isotropy of the system. CODION is ultimately applied onto disruption simulations. Although electric fields during disruptions can reach magnitudes at the order of hundreds of V/m, anisotropic alpha distributions are unlikely to occur. Similar to a research on runaway ions [53], it was concluded during this study, that the disruption timescale is too short for significant alpha acceleration. The distribution function is found largely independent of pitch, which will be discussed in detail in section 5.2.3.

CODION is used throughout paper A [78] to calculate alpha particle distributions during various scenarios of disrupting ITER plasmas. The plasma is represented by a radial grid (101 points) and each point is populated with an alpha distribution according

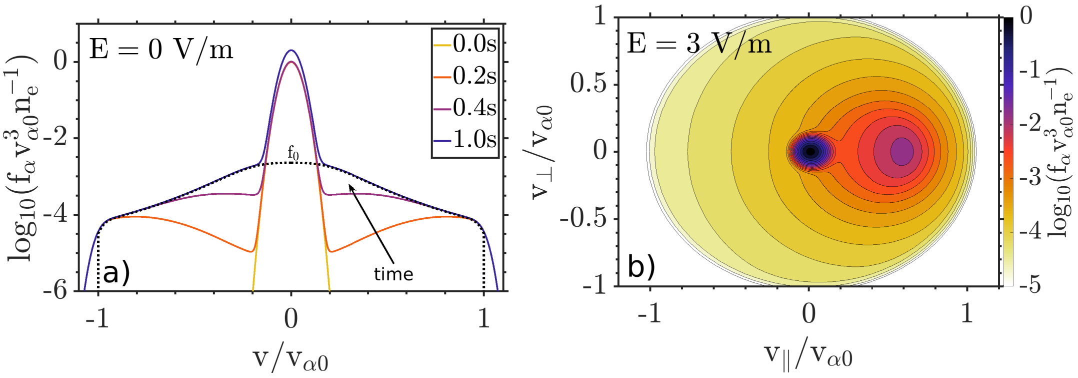

Figure 4.1: a) Time-evolution of an isotropic alpha distribution $f_\alpha(v,t)$ where the fusion is initiated at $t > 0$. The 50%-50% D-T bulk plasma has a temperature of $T_e = T_i = 10$ keV and an electron density of $n_e = n_\mathrm{D} + n_\mathrm{T} = 10^{20}\,\mathrm{m}^{-3}$. Colors indicate time. The analytical slowing-down distribution f_0 is added to the picture (black, dotted). Resolution parameters are 2000 velocity grid points, two Legendre polynomials (due to isotropy) and 20 time-points. b) A 2D-velocity representation of $f_\alpha(v,\xi)$ that was under the influence of a constant electric field $E_\parallel = 3\,\mathrm{V/m}$ for 1 s. The fusion process happened under the same plasma conditions as in a).

to the respective plasma parameters. With the ultimate aim to calculate wave-particle interactions (section 2.4), the focus lies on energetic particles, i.e. the tail of the distribution function $f_{\alpha,\mathrm{EP}}$. We require that the energetic tail of the distribution has reached its steady-state $f_{\alpha,\mathrm{EP}} \simeq f_0$ before the disruption initiates. Two methods are implemented, the first one requires the density in a small velocity space region around $v = 0$ to start growing, while the second method prescribes a specific total density that has to be reached. The density profile of the alpha particles in a burning ITER plasma has been estimated and widely used in literature [19] and is generally matched well by the first method. Once the initial distribution is obtained, the fusion source S_α is disabled and an exponential decay in temperature on a millisecond timescale is simulated modeling a thermal quench, that begins at $t = 0$. The slowing-down of the alpha particles following the plasma disruption is tracked with CODION. For further usage, a way of transferring the energetic part of the distribution functions $f_{\alpha,\mathrm{EP}}$ from CODION to HAGIS had to be implemented. HAGIS already contains the means to include analytic alpha distribution functions in the slowing-down form of f_0 (eq. (2.16)). we exploit this by fitting the CODION distributions with a similar form.

A script was written, that performs a fit on the CODION-obtained distributions with a function f_fit and separates the function into Maxwellian and energetic part:

$$f_\alpha \approx f_\mathrm{fit} = f_\mathrm{fit,M} + f_\mathrm{fit,EP} = p_1 \exp^{-x^2/p_2} + \frac{p_3}{x^3 + p_4^3} \mathrm{Erfc}\left(\frac{x - p_5}{p_6}\right),$$

where $x \equiv v/v_{\alpha,0}$ is the normalized velocity space and p_{1-6} are six fit-parameters. The fit-parameters are generally a function of time t and radius r, as every alpha distribution $f_\alpha(r,t)$ is evolved in time. The total form of the function f_fit represents a Maxwellian plus a slowing-down form f_0. In order to avoid further numerical issues, the unit-step function $\mathrm{U}(x)$, that normally limits the energetic tail, is approximated with the complementary error function $\mathrm{Erfc}(x)$:

$$\mathrm{U}(1 - x) \longrightarrow \frac{1}{2}\mathrm{Erfc}\left(\frac{x - p_5}{p_6}\right).$$

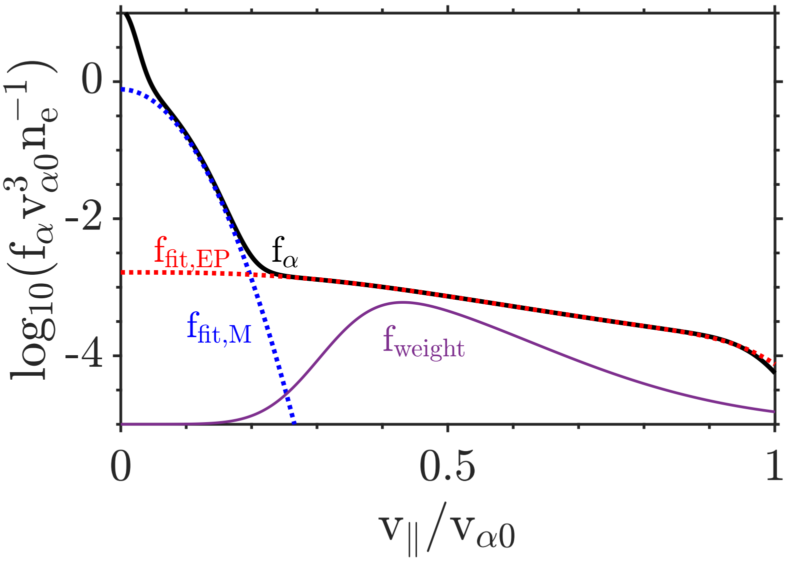

Figure 4.2: Example fit of the CODION-data (black) with the Maxwellian (blue, dotted) and the energetic (red, dotted) part of the fitting function f_{fit}. Note that the weight-function f_{weight} has been shifted by -5 on the y-axis for the purpose of visibility.

where p_6 represents a finite width at the (now variable) cut-off velocity p_5. From comparisons with the analytic formulae, that are valid for steady-state, one can obtain good initial values for the fit parameters. Initially, the parameter p_1 corresponds to the bulk alpha density, p_2 to the background temperature, p_3 to the tail density and p_4 corresponds to $v_c/v_{\alpha 0}$. In the error function, initially $p_5 = 1$ holds, while p_6 - representing the velocity width at birth - can be calculated from equation (4.2). For each consecutive time-step during the time evolution, the p-values from the previous time-step are used as new initial guess and bound to only change by ±25% per step in time. This way, a robust set of evolving energetic alpha particle distributions

$$f_{\alpha,EP} \simeq f_{\text{fit},EP} = \frac{p_3}{x^3 + p_4^3} \text{Erfc}\left(\frac{x - p_5}{p_6}\right) \tag{4.3}$$

are obtained via the fit parameters p_{3-6}. In the application, the fit parameters p_{3-6} are a function of both time t and radius r, representing the entire plasma evolving.

Due to the many orders of magnitudes covered by the distribution function f_α, the fitting is performed in logarithmic space. In order to put more focus on the energetic tail, f_{fit} is multiplied with a weight-function, that is a skewed and shifted normal distribution of the form

$$f_{\text{weight}} = \exp^{-5(x-w_1)^2} \cdot \Big(1 + \text{Erf}\left(w_2(x - w_1)\right)\Big)$$

with two additional parameters $w_1 = 0.2$, $w_2 = 10$ and the Error function $\text{Erf}(x)$. The fitting itself is performed in MATLAB with the build-in `lsqnonlin` function, that is a non-linear least-squares data-fitter. In figure 4.2 an example is shown. At $t = 0.7\,\text{ms} > 0$ the steady-state situation is already left and the Maxwellian form is distorted by the temperature decay. It is this distortion, that generally impedes a straightforward Maxwellian fit and subsequently affects $f_{\text{fit,EP}}$. A proper result is only obtained with the usage of f_{weight} and slowly evolving fitting parameters p. The latter benefits from a higher temporal resolution in the CODION simulation.

With the CODION module presented in this section, we were able to calculate a self-consistent evolution of fusion-born alpha particles undergoing various thermal quench scenarios in an ITER plasma [78]. With the distribution functions obtained, we can compute the EP-drive during the thermal quench with the method presented in section 4.2.1.

4.2 Code development in HAGIS

4.2.1 Import of CODION-calculated alpha particle distributions

HAGIS has already been used multiple times to calculate energetic particle drive (including alphas) in ITER plasmas [57, 128, 158], and as such it is benchmarked for ITER dimensions and alpha particle energies. The code is written in flux coordinates, hence the assumption $r/a \approx s$ (a minor plasma radius) is being made when transferring radial distributions from CODION.

Isotropic alpha populations can be provided to HAGIS as a product of the radial distribution $f(s)$ and the velocity distribution $f(v)$

$$f(s, v) = Cf(v)f(s),$$

where C can be determined by the number ratio of alpha particles to background ions $n_\alpha/(n_D + n_T)$ on the magnetic axis $s = 0$. With the fitted distributions in CODION, that are defined by $p_{3-6}(r)$, this corresponds to

$$\begin{aligned}
f(s) &= p_3(r)/p_3(0),\\
f(v) &= \frac{v_{\alpha 0}^3}{v^3 + (p_4 v_{\alpha 0})^3}\mathrm{Erfc}\left(\frac{v - p_5 v_{\alpha 0}}{p_6 v_{\alpha 0}}\right),\\
C = \frac{n_\alpha}{n_D + n_T} &= \frac{4\pi}{n_D + n_T}\int_0^1 \frac{1}{x^3 + p_4^3}\mathrm{Erfc}\left(\frac{x - p_5}{p_6}\right)\,\mathrm{d}x,
\end{aligned}$$

where the alpha particle density on axis is calculated with the isotropic, gyro-averaged velocity moment of the distribution. From its creation, the code had the option to provide alpha velocity distributions $f(v)$ with the analytical equation of the form of f_0 (eq. (2.16)). This input case was expanded, where the original variables of the slowing-down formula are replaced with the corresponding fit-parameters that could simply be read-in from a text file provided through CODION and the fitting procedures.

Shown in figure 4.3 is a small comparative simulation for the purpose of validation. It shows the mode evolution of an $n = 8$ TAE in an ITER plasma, driven by alpha particles. For equal plasma parameters, the velocity distribution $f(v)$ is prescribed by (1) the original HAGIS implementation and (2) by CODION simulations and the transfer into HAGIS using fitting parameters. The radial distribution $f(s)$ and EP density on axis C are the same in both cases. The linear growth rate is approximately $\gamma/\omega \approx 1.3\%$, where $\omega = 4.85 \cdot 10^5$ rad/s is the eigenfrequency of the mode (calculated by LIGKA).

With the possibility to import CODION-calculated alpha distribution functions, we are able to calculate the resonant wave-particle interaction between self-consistently evolved alpha particles and modes in a plasma equilibrium. Workflows already exist between HAGIS and LIGKA (section 3.4), which can provide the mode information required.

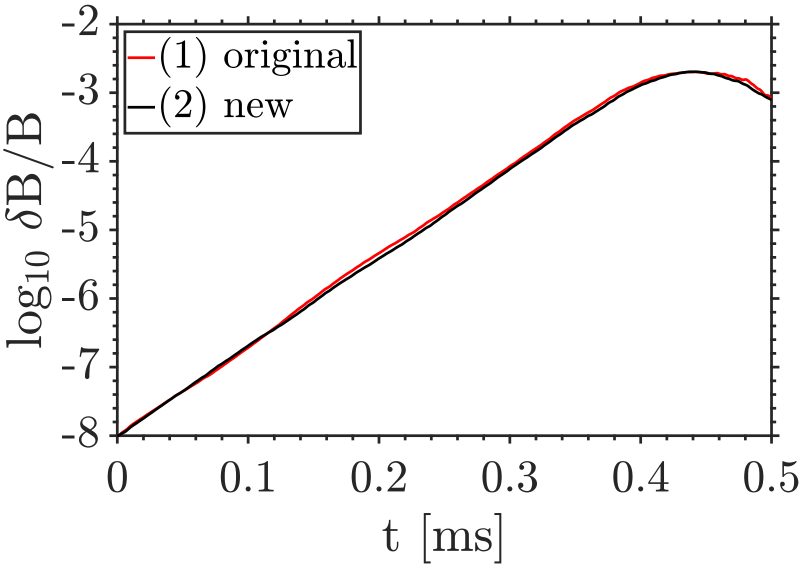

Figure 4.3: Validation simulation: perturbation amplitudes of a $n = 8$ TAE in HAGIS driven by the original implementation of a slowing-down distribution and the newly implemented one, which ultimately inputs CODION-calculated distributions. The plasma parameters are: electron temperature 25 keV, ion temperature, 21 keV, electron density $n_e = 10^{20}\,\mathrm{m}^{-3}$, $n_e = n_D + n_T$. The plasma equilibrium and TAE (structure and damping) is taken from the ITER simulations, which will be discussed in chapter 5. The spatial profile $f(s)$ is the expected alpha density profile for a burning ITER plasma.

4.2.2 Estimation of runaway electron transport caused by TAEs

Once the amplitude evolution for the excited TAEs is known, we apply HAGIS to estimate the TAE impact on runaway electrons. Due to the multi MeV energies that they can reach, REs require a relativistic treatment. Derived in the appendix of the paper A [78] (by co-author S. Braun) are the relativistic equations of motion for runaway electrons in the Boozer coordinate system, that is used in HAGIS. It follows the original derivation in the PhD thesis of S. Pinches [134], adding a relativistic extension to it. A verification of the numerical implementation into HAGIS can be found in reference [66], where comparisons with the ANTS code [123, 175, 176] have been made by tracking the same test particle ensembles in the same ITER plasma equilibrium.

Crucial for the application is the derived and implemented canonical toroidal angular momentum of a runaway electron

$$P_\varphi \propto p_\parallel - \psi$$

that is proportional to the relativistic parallel momentum $p_\parallel$ and the radial flux coordinate ψ. Due to their high energy and a lack of suitable resonances, runaways are not expected to have a back-reaction on the wave-evolution. Hence HAGIS is run in its “passive” mode, where only the effect of the presence of the TAEs is evaluated on runaway electron test particles. Ensembles of 10^4 test particles are initiated, on a phase-space grid in energy, pitch and radial position. With energies ranging from 10 keV to 30 MeV the test particles are representative of REs. The parallel velocity of the lowest energy electron (for purely parallel motion) is $v_\parallel \approx 6 \cdot 10^7\,\mathrm{m/s} \approx 8 v_A$, therefore resonances with the TAEs are unlikely. With the TAE amplitude held constant and the lack of resonances, changes to P_φ are dominated by changes to the radial coordinate ψ. Should a resonance still occur, it is calculated by HAGIS, but then changes to P_φ can also be due to changes in $p_\parallel$. Using this method in paper A [78], calculations about P_φ showed the possibility of radial transport of runaway electrons. However, for the follow-up study [79], this method of calculating P_ϕ was superseded, by the transport coefficient calculations with the ASCOT5 (section 3.6).

5 Study on post-disruption TAEs driven by alpha particles and its influence on runaway electron generation

This chapter is concerned with a detailed examination of the post-disruption concept proposed in section 1.1 and summarized in figure 1.3. For a D-T ITER plasma, that suffered a disruption, we establish the TAEs supported by the equilibrium and the damping of the cooling bulk plasma in section 5.1. The population of fusion-born alpha particles is subject of section 5.2, while their interaction with the TAEs is treated in section 5.3.

As we will discuss in detail later, we can focus a majority of the study on the TQ time scale, and will also consider a simple model for the MMI. Possible scenarios are further expanded through varying thermal quench time-scales and possible alpha particle transport (section 5.3.2). To gain quick access to the parameter space, we present an analytical velocity space model for the alpha particles in section 5.2.2.

Finally, in section 5.4 we gather the knowledge from the previous sections and conduct a disruption simulation, aimed to establish the influence of the alpha-driven TAEs on runaway electron generation. The results are discussed and contextualized in chapter 6.

5.1 Spectrum of weakly damped Alfvénic modes in the ITER post-disruption plasma equilibrium

We introduce the ITER plasma scenario, which will be the subject of study in the next sections. Necessary is a calculation of the plasma equilibrium and Alfvénic mode spectrum, that can be expected in a thermal quench following a disruption. The pre-disruption state of the plasma will be determined from a predictive operational scenario called "scenario #2" [19, 177], which is commonly used for simulations. Main plasma parameters and their notation are summarized in table 5.1 and depicted in figure 5.1. This scenario is used as an initial state and consecutively evolved with GO (section 3.2.

The plasma scenario we reside in corresponds to a maximum performance ITER operation, with a total plasma current of 15 MA and an active nuclear phase, where the hydrogen isotopes deuterium and tritium undergo fusion. This scenario foresees a (mostly) flat electron density profile $n_{e0}(r)$. Due to the quasi-neutrality requirement of the plasma, the electron density has to fulfill $n_e = \sum_j Z_j n_j$, where j is an ion species with charge Z_j and density n_j. The species in question are singly ionized deuterium and tritium of equal densities $n_{D0} = n_{T0} \equiv n_{DT0}$, as well as an alpha particle species with charge $Z_\alpha = 2$ and density $n_{\alpha 0}$. D-T fusion generates the alpha particles, hence the alpha density profile is similar in shape to the ion temperature T_{i0}, peaking in the core at less than one percent of the electron density and therefore are classified as a minority species. Other minor impurities like beryllium or tungsten are neglected. The electron temperature T_{e0} is slightly higher than the ion temperature, because the most energetic

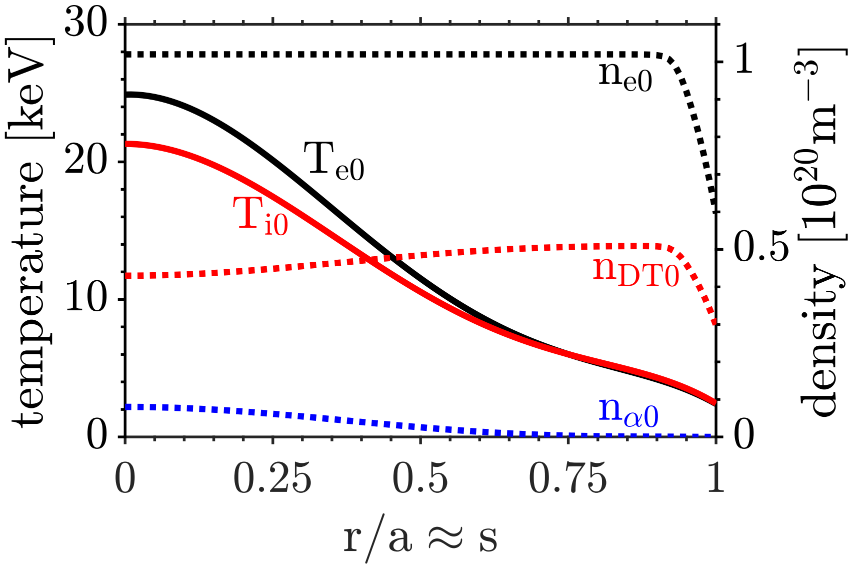

Figure 5.1: Profiles of particle densities (dashed) and temperatures (solid) of a burning ITER plasma.

alpha particles mainly collide with electrons (see section 2.1.1). In turn, the electrons heat the bulk ions and help sustain the fusion.

The profiles of temperature and density (figure 5.1) will initially be set up in the one dimensional, homogeneous plasma code GO (section 3.2), hence the profiles are cast in the normalized radius r/a. Subsequently applied codes, like HAGIS (section 3.5) or LIGKA (section 3.4) however are written in flux coordinates, hence the approximation $r/a \simeq s$ is made, where $s \equiv \sqrt{\Psi(r)/\Psi(a)}$ is the normalized poloidal flux coordinate.

A plasma disruption initiates a global thermal energy loss, which we model as an exponential temperature decay

$$T_1(r,t) = T_f + \left[T_{e0}(r) - T_f\right] \exp(-t/t_{\mathrm{TQ}}), \tag{5.1}$$

with a thermal quench time t_{TQ}, a final temperature $T_f = 10\,\mathrm{eV}$ (if not stated otherwise) and where we from now on assume equal temperatures for electrons and ions T_1. We

Parameter name	Notation	Value
Major radius	R_0	6.195 m
Minor radius	a	2.06 m
Effective charge	Z_{eff}	1.0
Normalised flux	ψ	$\Psi(r)/\Psi(a)$
Normalised radius	r/a	$r/a \simeq \sqrt{\psi} \equiv s$
Plasma current	I_{p0}	15 MA
Magnetic field on axis	$B(s=0)$	5.26 T
Electron density on axis	$n_{e0}(s=0)$	10^{20} m^{-3}
Ion density on axis	$n_{i0}(s=0)$	10^{20} m^{-3}
Electron temperature on axis	$T_{e0}(s=0)$	24.7 keV
Ion temperature on axis	$T_{i0}(s=0)$	21.2 keV

Table 5.1: The main plasma parameters of the 15 MA ITER scenario. Subscript 0 refers to variables of the initial, pre-disruption state.

also introduce the normalized disruption time-scale $t_N \equiv t/t_{\mathrm{TQ}}$, which serves as a metric of temperature independent of t_{TQ}. In order to model disruption mitigation systems, injections of deuterium and/or neon are allowed to elevate the plasma density. The amount injected is represented by the post-disruption electron density n_{e1} fulfilling the quasi-neutrality requirement:

$$n_{e0} \leq n_{e1} = n_{\mathrm{e0}} + n_{\mathrm{D1}} + n_{\mathrm{NE1}}, \tag{5.2}$$

where n_{D1} is the injected deuterium density and n_{NE1} the injected (singly ionized) neon density. The injected material is assumed to be singly ionized and deposited instantly at $t = 0$ and across the entire plasma. In reality, the injection of material and the evolution of temperature is not independent of each other, but determining the correlation is outside the scope of this work. Instead, parameter scans for the densities and the quench pace t_{TQ} will be conducted. The exponential decay in temperature assumes the global energy loss to be dominated by MHD-induced losses, which scale as $\sim T^{5/2}$ [178], but can be assumed approximately exponential [104]. Due to the strong temperature scaling, this assumption is especially valid in the initial phase of the thermal quench, after which the temperature evolution is increasingly determined by effects like line radiation from impurities, Ohmic heating, Bremsstrahlung and ionization of the impurities. Our disruption calculation tools (GO and DREAM) are equipped with energy balance equations, that would self-consistently evolve the temperature including the above mentioned effects. However, we will mostly be interested in the initial phase of the thermal quench, with plasma temperatures down to the order of hundreds of eVs, allowing us to omit the energy balance equation.

The equilibrium state of a plasma is shaped by a balance of confining Lorentz forces and the plasma pressure seeking expansion, $\mathbf{j} \times \mathbf{B} = \nabla p$. A disruption disturbs this equilibrium, however, the re-establishment of a force balance occurs on the Alfvénic time-scale $R_0/v_A \sim \mu$s, which is many orders of magnitudes faster than the typical disruption time-scale ($t_{\mathrm{TQ}} \sim$ ms). The healing of the flux surfaces will be addressed in discussed in detail at the end of section 5.3. We evolve the plasma pressure $p(r,t)$ and current density $j(r,t)$ with GO (section 3.2) and use these profiles to reconstruct the plasma equilibrium using VMEC (section 3.3).

Beginning with the pressure calculations, the deuterium and tritium species are treated as background pressure p_{b1} and separated from the energetic alpha particle pressure $p_{\alpha 1}$. Typical thermal collision timescales are of the order of microseconds, allowing one to assume the bulk of the plasma to remain perpetually in a thermal equilibrium during the temperature quench. Therefore, we calculate the pressure of the background populations using the ideal gas equation, $p_{b1} = 2eT_1 n_{e0}$, where we used the equal post-disruption temperatures and densities of ions and electrons. Instead of following the complicated temperature evolution of injected material, we assume one temperature for simplicity and to avoid blowing up the dimensionality of the scans. The exact temperature of the impurities is not really important from the alpha-drive point of view and is unlikely to play a role in the damping either. The injected material is therefore modelled with a Maxwellian of 10 eV and as a singly ionized species and does not partake in the background pressure.

Although the alpha particles are a minority species in the plasma ($n_{\alpha 0} < 10^{-2} n_{e0}$), their energetic nature allows them to exert a significant amount of pressure, which cannot be calculated appropriately using the ideal gas equation. Instead, we use CODION with the alpha particle module (section 4.1) to calculate distribution functions $f_\alpha(r,v,t)$. The distribution functions are initiated (with the plasma parameter profiles in figure 5.1) on a radial grid r/a consisting of 101 points. $f_\alpha(r,v,t)$ are then evolved in the thermal

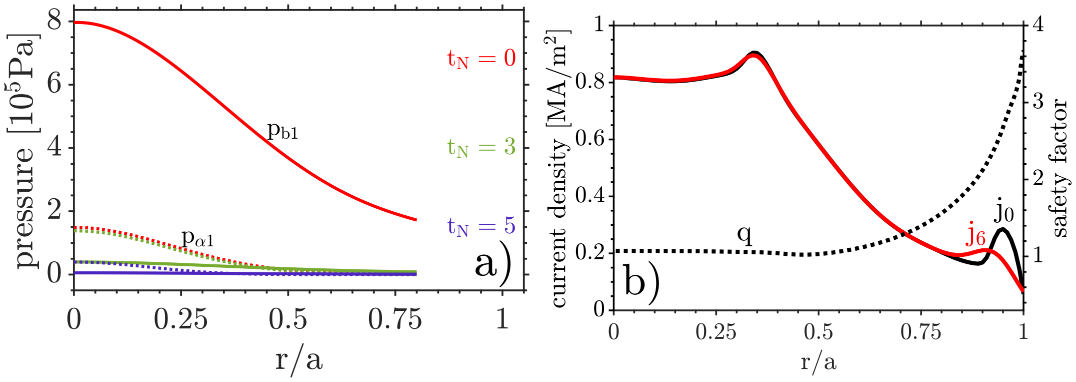

Figure 5.2: a) The time-evolution of pressure for the background plasma p_{b1} (solid) and the alpha distribution $p_{\alpha 1}$ (dashed) as a function of the normalized time $t_N = t/t_{\text{TQ}}$ indicated by color. The plasma is initialized via the plasma parameter profiles in figure 5.1, followed by an (unmitigated) disruption defined by $t_{\text{TQ}} = 1\,\text{ms}$, $n_{e1} = n_{e0}$ and $Z_1 = 5/3$ (pure D-T plasma). The profiles are shown only up to $r = 0.8a$. b) Graph of current density $j(r)$ (solid) in a 15 MA ITER plasma for the time-points $t_N = 0$ (j_0) and $t_N = 6$ (j_6) after the exponential thermal quench. In addition we show the safety factor profile q (dashed).

quench according to the temperature eq. (5.1) and their pressure is computed using the second velocity moment of their distribution function f_α:

$$p_{\alpha 1}(r,t) = \frac{4\pi m_\alpha}{3}\int_0^{v_{\alpha 0}} v^2 f_\alpha(r,v,t)\mathrm{d}v, \tag{5.3}$$

where we assume isotropy and applied gyro-averaging in the velocity space. While CODION was used for the reconstruction of the equilibrium used in paper A and paper B, an analytical model (section 5.2.2) for f_α was derived in the work of paper B. For the illustrations of the pressure in this chapter we use the analytical model.

The evolution of $p_{\alpha 1}$ is governed by the thermalization process of the alpha particles, as prescribed by the changes of densities and temperature profile. In figure 5.2a), $p_{\alpha 1}$ and p_{b1} are depicted separately for an unmitigated disruption case. In pre-thermal quench, the alpha pressure in the plasma center accounts for roughly 15% of the total plasma pressure, matching theoretical predictions [19]. As will be discussed in section 5.2, the energetic tail is able to resist the deceleration for a significant amount of time, while the background pressure shrinks according to the exponential temperature drop. This delay allows the alphas to briefly dominate the (core) pressure at around $t_N = 3$, albeit at a magnitude that is low compared to the pre-thermal condition. Even though the injection of (cold) material into the plasma does not significantly contribute to the pressure itself, it enhances the deceleration of the alpha particles. As such, the pressure of the unmitigated case sets an upper limit to the pressure profile used for equilibrium reconstruction.

Calculations of the current density $j(r)$ are conducted with the GO code (section 3.2). Shown in figure 5.2b) is the current density $j(r)$ in an unmitigated ITER disruption ($n_{e1} = n_{e0}$) with $t_{\text{TQ}} = 1\,\text{ms}$ for the time-points $t_N = 0$ (j_0) and $t_N = 6$ (j_6) . The plasma carries a majority of the current in the hot, highly conductive core. Because of the large magnitude of the plasma current, it cannot change on the same timescale as the temperature/pressure and therefore, even after $t_N = 6$, the current density is barely evolved. Our assumption that T_1 and n_{e1} are not correlated therefore also means, that the material injection will not affect the current density profile. This comes down to

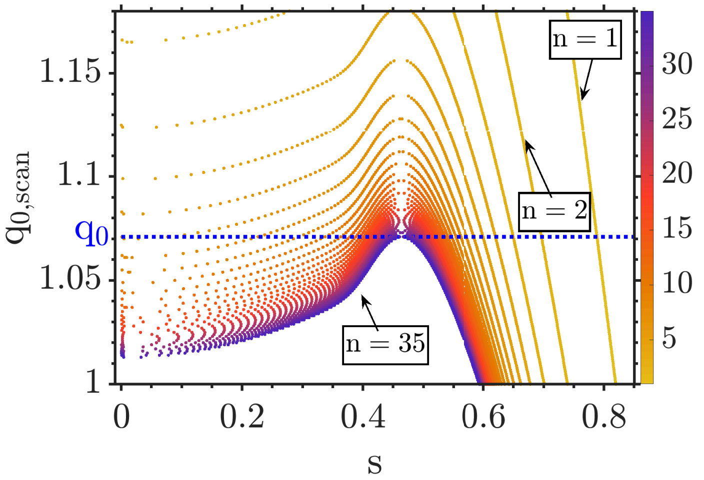

Figure 5.3: Shape-preserving q-profile scan showing the radial location of the TAE frequency gaps as allowed by the ITER post-disruption equilibrium. Depicted in color are TAEs of toroidal mode number n. The on-axis q-value eventually opted for further analysis is $q_0 = 1.071$ and is shown with a blue dotted line.

the conductivity being a strong function of temperature, but only a weak function of density through the Coulomb logarithm.

With both pressure $p_1 = p_{b1} + p_{\alpha 1}$ and current density j obtained, the required input for a VMEC calculation of a tokamak plasma equilibrium is available. We will be focusing on the thermal quench and desire a post-disruption equilibrium, that is valid for (at least) the lifetime of energetic alphas, which will later be calculated to be $< t_N = 6$ (section 5.2.3). With a current density profile close to its pre-disruption condition and the thermal pressure exponentially decaying, the dominating factor in determining the plasma equilibrium for the TQ is $j_0 \simeq j_6$. With the geometry and magnetic field parameters of ITER, as well as a total current of 15 MA, the current density j_0 and the pressure $p_1(t_N = 3)$ is employed for the VMEC calculation.

The current density and pressure profile allows one to solve the Grad-Shafranov equation, i.e. obtain flux surfaces with constant pressure, that define the plasma equilibrium [1]. In figure 5.2b I show the q-profile output of the plasma equilibrium determined by VMEC. Since the current density j generates the poloidal magnetic field, it is responsible for the shape of the q-profile. A slightly pronounced local minimum in q can be found at $r \lesssim 0.5a$, and is caused by the maximum of j at around the same radius. Moving towards the edge of the plasma, q rises until it reaches an edge value of $q_{\text{edge}} > 3.5$. In order to account for the pressure variations and/or to the disruption scenario itself, a sensitivity scan will be conducted. The sensitivity measure will be the spatial location and the number density of Alfvénic modes, that this equilibrium supports under a shape-preserving scan over the q-profile elevation and is an approach similar to reference [179].

With the help of the code LIGKA (section 3.4), we investigate the plasma equilibrium by calculating the toroidicity-induced frequency gaps in the ideal MHD spectrum. This reveals Toroidal Alfvén Eigenmodes (TAEs), that lie outside the frequency continuum and therefore are weakly damped. The TAEs are represented by a Fourier decomposition in the poloidal and toroidal direction and are located around the radial position r_{TAE},

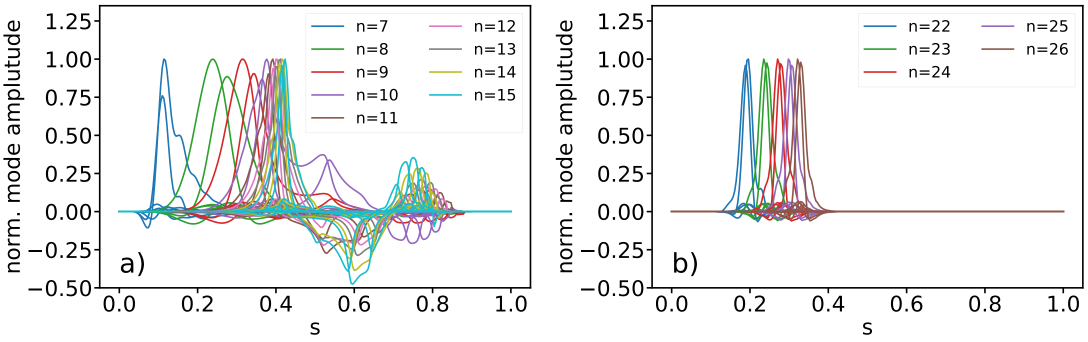

Figure 5.4: Normalized eigenfunctions of the post-disruption ITER TAEs in the a) low-n branch and the b) high-n branch showing all the individual poloidal harmonics of the electrostatic potential. The eigenmodes shown are of even parity, as seen by the equal sign of the dominating poloidal harmonics.

where (see section 2.3.2)

$$q(r_{\mathrm{TAE}}) = \frac{m + 1/2}{n} \tag{5.4}$$

holds for the toroidal mode number n and poloidal mode number m. The LIGKA scans are conducted as a function of q-profile elevation on axis $q_{0,\mathrm{scan}}$, with results of the TAE locations shown in figure 5.3. The results show, that irrespective of $q_{0,\mathrm{scan}}$, there is a robust set of weakly damped TAEs with toroidal mode numbers $1 < n < 35$ in this post-disruption ITER equilibrium. Another type of Alfvénic modes, the Beta-induced Alfvén Eigenmodes (BAEs [180]), is found by LIGKA in the steep pressure region of the pre-disruption phase, but neglected for this work. In addition to EP drive, BAE-drive requires a high thermal ion pressure (beta), that is not given in the thermal quench. The solutions that are shown here are from the even TAE branch. These are modes, which are located near the bottom of the frequency gap and the poloidal harmonics of their electrostatic potential have the same sign. Such modes are often referred to as "ballooning" modes, because the poloidal harmonics interfere constructively on the low-field side (LFS, outboards) of the tokamak. These even-parity TAEs have generally been found to be the most unstable AE branch [22]. Their frequencies (in this unmitigated simulation) range from $\omega = v_A/(4\pi q(s)R_0) \propto 1/q(s)\sqrt{n_i} \approx 74\,\mathrm{kHz} - 83\,\mathrm{kHz}$ and vary mainly due to the q-profile, as the ion density profile we consider is flat. TAEs of odd parity can be found near the top of the frequency gap and the constructive interference occurs on the high-field side (HFS) of the tokamak, as neighbouring poloidal harmonics of their electrostatic potential have opposite signs (see section 2.3.2). While this uneven branch can be weakly damped as well [128], its usually higher eigenfrequency $\omega > 100\,\mathrm{kHz}$ leads to a weaker EP drive. Nonetheless, the odd branch will later be included in wave-particle interactions (section 5.3) for completeness, however not considered further in this section. Ultimately, the TAEs are going to interact with the energetic alpha particles in the plasma and draw energy from their spatial pressure gradient (see figure 5.2a)). We choose an on-axis safety-factor value of $q_0 = 1.071$ and determine the TAEs, that are found in the region of strong alpha particle pressure, $0 < s < 0.5$. The global mode structures are also computed by LIGKA and shown in figure 5.4. Dominant poloidal harmonics of TAEs are often $(m = n, m = n + 1)$, but for higher q other pairs of (m, n) can be found that fulfill equation (5.4). Due to the flatness of the q-profile in the inner half of the plasma, a high density of neighbouring TAEs is present. This allows a spatial overlap of modes, that leads to resonance overlap in the phase-space with the potential to cause particle transport [57]. A high-n $(n = 22 - 26)$ branch and a low-n branch

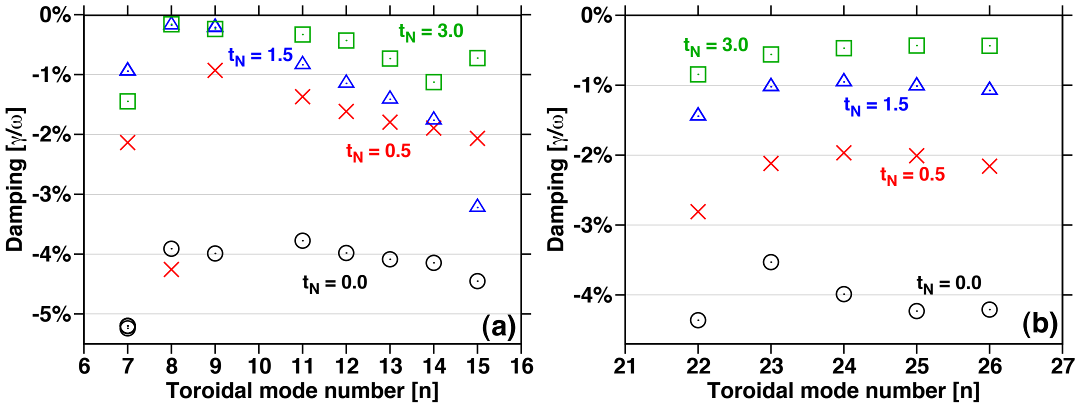

Figure 5.5: The sum of electron Landau damping, ion Landau damping, continuum damping and radiative damping on the M_1 set of TAEs. The damping γ is normalized to the TAE eigenfrequency ω and displayed as a function of normalized time t_N, where the temperature decay $T_1 \simeq T_{e0}\exp(-t_N)$ represents a plasma thermal quench. a) shows the low-n branch and b) the high-n branch of M_1.

($n = 7 - 15$) is identified, with up to 13 poloidal harmonics used to represent each mode in Fourier space. The width of the mode can be approximated with $\Delta_{\text{TAE}} \simeq r_{\text{TAE}}/m$ and becomes narrower for higher mode numbers $n \sim m$.

The TAE modes of the plasma are considered as perturbations to the plasma equilibrium. The perturbation growth is a competing process between a driving force and damping. While the energetic alpha particles will eventually serve as instability drive, the thermal background generally stabilizes the TAEs through various types of damping (see section 2.4.1). The magnitudes of ion Landau damping, electron Landau damping, radiative damping and continuum damping are calculated for each mode individually, with special focus on the behaviour during mitigated quenches, i.e. as a function of temperature and plasma densities. Collisional damping on trapped electrons is addressed with an analytical formula [141] and damping of the resistive plasma is included with a numerical resistive MHD tool CASTOR (Complex Alfvén Spectrum of TORoidal plasmas) [181]. We find the latter two damping mechanisms to be insignificant in the thermal quench.

During the LIGKA application described above, the calculation of modes was restricted to the inner half of the plasma, $0 < s < 0.5$, which is roughly the radial extent of the alpha particles (see figure 5.2a)). This restriction yields a set of modes that we will denote with M_1 and that generally has the low-n and high-n branches of even TAEs mentioned above. This set of modes is used in this section, while the last section 5.4 will lift said restriction and include odd-parity TAEs for a complete disruption simulation.

LIGKA is used to calculate the electron and ion Landau damping, the radiative damping and the continuum damping during the thermal quench of a disrupting ITER plasma, that can be mitigated through material influx. Its initial state is described by the scenario profiles (figure 5.1), the evolution of temperature T_1 by equation (5.1) and the changes in density are represented by n_{e1} (eq. (5.2)). For these damping calculations, the presence of alpha particles is neglected and later retained when we calculate their drive.

With the unmitigated case, ($n_{e1} = n_{e0}$), we isolate the effects of the evolving temperature and display the total of damping values in figure 5.5, which shows, that the

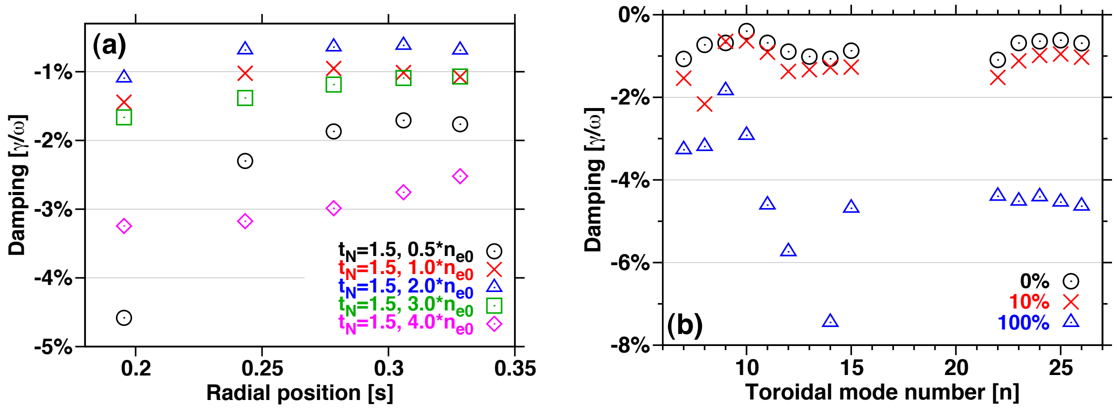

Figure 5.6: a) The damping strengths on the high-n TAE branch of M_1, as a function of electron density at a fixed temperature profile $T_1(t_N = 1.5)$. The electron density is elevated from n_{e0} by an addition of singly ionized deuterium. b) The damping on M_1 in case of elevated density $n_{e1} = 2n_{e0}$, where the legend displays the amount of neon used in the injection. The case of 0% corresponds to the $2n_{e0}$ values in a), but includes the low-n branch as well.

damping decreases as a function of t_N. At the initial stage $t_N = 0$, for the respective electron and ion thermal velocities $v_{th,e}/v_A = 6.1$ and $v_{th,i}/v_A = 0.09$ holds, where the ion thermal velocity is calculated for an "average" D-T ion with mass $m = 2.5m_p$, where m_p is the proton mass. The D-T ions provide a significant contribution through their Maxwell tail and higher side-band resonances with the Alfvén velocity (section 2.4.1). During the TQ, the thermal populations cool down and the ion tail becomes no longer efficiently damping. The electron Landau damping is known to evolve proportional to the electron pressure $\beta_e \propto T_e$ [140] and therefore decays as well. Due to the TAEs residing in continuum gaps, the continuum damping is essentially zero and unaffected by the temperature. The radiative damping is based around finite Larmor radius effects. Because the Larmor radius of thermal particles shrinks during the thermal quench, this effect loses effectiveness as well.

We now fix the temperature to $T_1(t_N = 1.5)$ and repeat the previous calculation for various density changes to the pre-disruption plasma, representing an injection of material. The injection is modeled as a Maxwellian distribution at 10 eV. Figure 5.6a) shows this density scan affecting the damping on the high-n branch with a pure deuterium injection. The material deposition increases the plasma mass, and thereby decreases the Alfvén velocity v_A, shifting it relative to the thermal velocities. With a reduction to half the electron density instead (though difficult with material injection), the electron Landau damping increases, as v_A approaches $v_{th,e}$. We see a damping minimum at $n_{e1} = 2n_{e0}$, but with further increase, the ion Landau damping becomes stronger and again comes close to pre-disruption conditions at $n_{e1} = 4n_{e0}$. Additionally, we run LIGKA simulations, where the injected material is composed of 0%, 10% and 100% singly ionized neon, rest deuterium. The high mass of the neon has a significant effect on the damping strength as shown in figure 5.6b).

For the collisional damping on trapped electrons, analytical formulae specific to TAEs exist and are found in a more detailed discussion around eq. (26) in reference [22]. The damping strength becomes more relevant as the collision frequency grows in a cooling plasma. For a TAE representative of our MHD spectrum, $n = 10$, $m = 10$, $q = 1$, $\omega = 80\,\text{kHz}$, the damping strength γ_e/ω overcomes 1% at $t_N \approx 5.5$, but is insignificant before that.

Resistive MHD fluid effects can be included with use of the resistive MHD code CASTOR [181]. From the simulation we learn, that this damping is $\gamma_{\mathrm{res}}/\omega < 1\%$ ($\omega = 80\,\mathrm{kHz}$) up to a resistivity of $\approx 0.56 \cdot 10^{-4}\,\Omega\mathrm{m}$, which corresponds to a background temperature of $\approx 6\,\mathrm{eV}$. Such low temperatures will not be reached in our simulations and for the wave-particle interactions we swill remain well within $[1.5t_N, 5.5t_N]$, therefore both the resistive damping and the collisional damping on trapped electrons is neglected.

5.2 Alpha particle slowing-down distributions in an ITER thermal quench

Operation of the ITER [2] tokamak eventually foresees deuterium-tritium (D-T) plasma, producing alpha particles at a kinetic energy of $E_\alpha = 3.5$ MeV. One goal of ITER is to showcase self heating, i.e. that these energetic alphas allow the tokamak to sustain its high temperature and maintain the fusion process for a considerable duration (> 1000 s). The energetic alphas serve as an inner plasma heating, but once thermalized, they need to be removed from the plasma to avoid dilution of the fuel [89]. Through a balance of particle birth and sink, a steady-state distribution (section 2.1.1) is established of which detailed theoretical analysis exist [22, 182]. In the event of a plasma disruption the fusion and birth process ceases, global plasma parameters suddenly change and this steady-state situation is forcefully left. Studies about the dynamic evolution of the alpha distribution that follows used to lack in literature but now can be found in paper A [78] and paper B [79]. Although these alphas remain a minority species in the tokamak plasma, their energetic nature allows for interesting interactions with plasma waves, even during the dynamic process of the thermalization. For an accurate calculation of these processes, the distribution function of the alpha particles needs to be resolved.

In the following, the collisional thermalization of alpha particles undergoing a collapse of plasma temperature is studied. An accurate computation of an energetic population requires a kinetic treatment and a focus on particle distribution functions. In section 5.2.1, we will begin with a numerical treatment and present the results, that eventually lead to a new analytical model (section 5.2.2).

5.2.1 Numerical calculation of the thermalizing alpha particles

With an alpha particle fusion source implemented (section 4.1), CODION is used to calculate the spatio-temporal evolution of alpha particles in a disrupting ITER plasma. The initial plasma conditions resemble that of "scenario #2" introduced in section 5.1. The global plasma parameters of this scenario can be found in figure 5.1 and are used for an initialization of the alpha distributions. Similar to section 5.1, the plasma disruptive event is modeled with a thermal quench described by an exponential decay in temperature. The numerical treatment of the alpha particles presented here is covered in paper A [78].

We define the plasma on a radial grid r/a, spanning 101 points with the temperature and density values taken from the scenario data (figure 5.1). Each point is populated with an initial alpha particle distribution $f_\alpha(r, v, t)$ in CODION according to equation (4.1). We initiate thermal quenches (eq. (5.1)) at $t = 0$, with a total of 150 scenarios with $t_{\mathrm{TQ}} = [0.1 - 1]\,\mathrm{ms}$ and $T_f = [1 - 15]\,\mathrm{eV}$. The plasma density is held constant. The kinetic simulation with CODION is supported by a fluid disruption simulation with GO, whose purpose it is to calculate the electric field, that is induced during the disruption (see figure 3.1). A small electric field ($\sim 0.01\,\mathrm{V/m}$) is required in the quiescent phase in order to maintain the plasma current I_{p0}, but is neglected for the CODION simulation.

The disruption-induced electric field is depicted in figure 5.7c) for a case of $t_{\mathrm{TQ}} = 1\,\mathrm{ms}$, $T_f = 15\,\mathrm{eV}$ and a plasma density held constant. For other thermal quench scenarios, the picture is qualitatively the same, but with higher maximum electric field values for shorter quenches, and a radially more outwards localization of the maximum for lower final temperatures. The induction of the electric field opposes any changes to the plasma current. As shown in a previous simulation (figure 5.2b)), the current (density) can be assumed approximately constant for $t_N < 6$; this is also seen here in the electric field, that is of low magnitude for $t_N < 6$.

In figure 5.7 we show the CODION-calculated evolution of $f_\alpha(r, v, t)$ at two spatial points $r/a = 0$ (figure 5.7a)) and $r/a = 0.8$ (figure 5.7b)), both with and without E-field input. One can see the slowing-down process and the thermalization with the background plasma, that occurs on a ms timescale. Importantly, we also see that the electric field, that accelerates the ions in positive velocity direction, has a negligible effect on the distribution function. Once the E-field begins reaching significant values ($\gtrsim 6t_N$), the alpha population is near its thermalized state and the collisional slowing-down outweighs the acceleration, even at $t = 8t_N$. Throughout the entire simulation, the kinetic pressure of the distribution is altered by the electric field on a sub-percentage level compared to a simulation without E-field. Even with a prolonged CODION simulation ($t = 20t_N$), the electric field is not able to drag out an energetic tail of alphas, which prohibits a generation of runaway alpha particles after the thermalization and coincides with previous findings on runaway ions [53]. Note that in previous figure 4.1 the inclusion of an $E = 3\,\mathrm{V/m}$ electric field seems significant to the alpha distributions, however, such a significance is only obtained for the steady-state distribution, which may take significantly longer to set than the disruption timescale allows.

Because of the negligible impact of the electric field, the alpha distribution remains fully isotropic, even under the presence of a disruption-induced electric field. The isotropy assumption enables the derivation of an analytical alpha particle model in the next section 5.2.2. Here we only explicitly showed the isotropy to be valid for one thermal quench scenario, but this will be re-evaluated for different thermal quench scenarios (t_{TQ}, T_f) and for mitigated cases ($n_{e1} > n_{e0}$) in section 5.2.3, with the help of the analytical model.

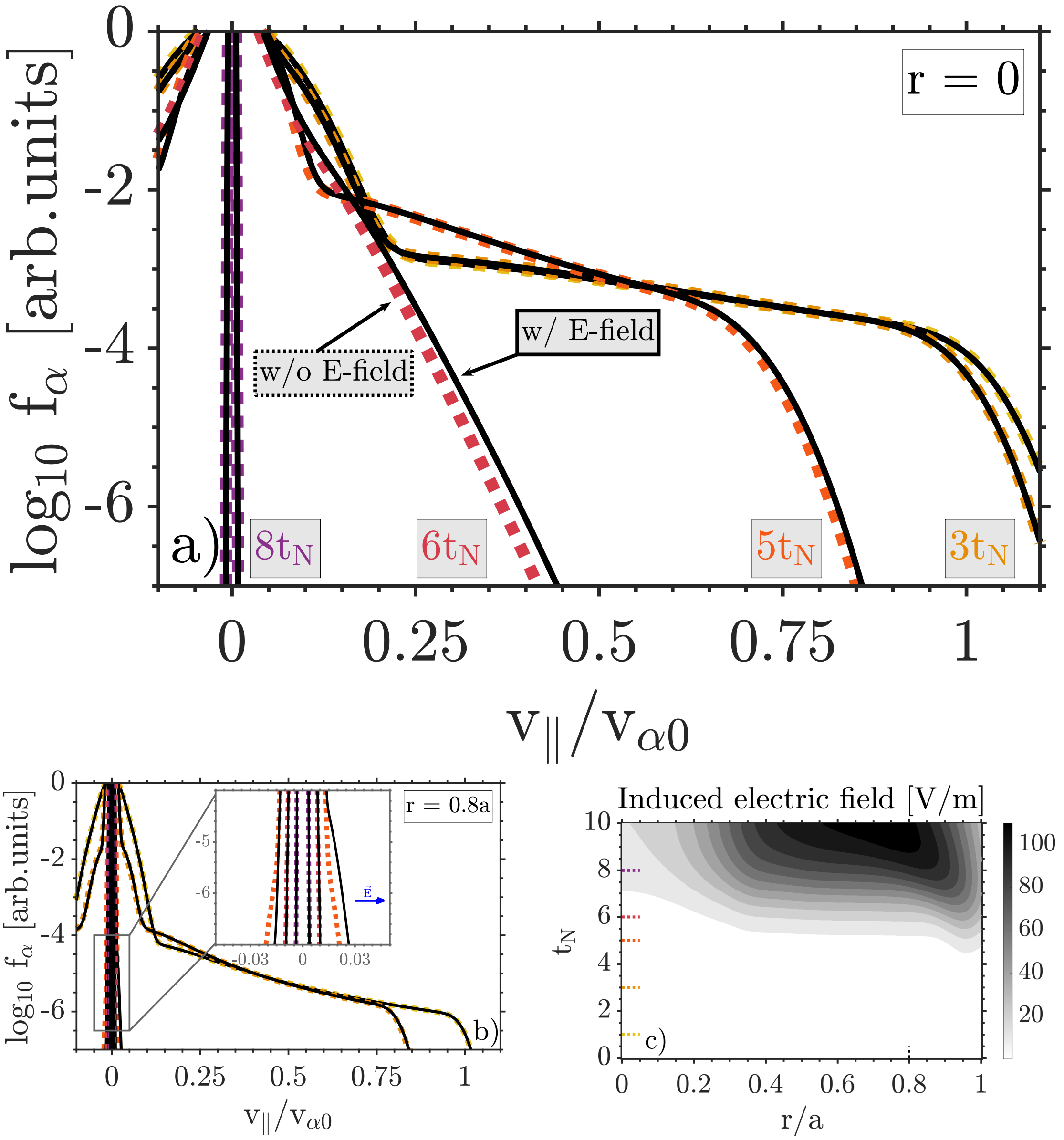

Figure 5.7: a) The alpha distribution function f_α at the ITER plasma centre during a thermal quench, evolving without (dashed, color) and with (solid, black) electric field input. b) The same simulation as in a) but at $r/a = 0.8$. The colors indicate the time-steps and are the same as in a). Resolution parameters are: Velocity grid points $N_x = 2000$, number of Legendre modes $N_L = 35$ for b) and $N_L = 2$ for a) and number of time-steps for the entire simulation $N_t = 10000$. c) The induced electric field that is used as input for a) and b). The dashed lines mark the time-points (color) and radial position (black) used in a) and b).

5.2.2 Analytical alpha particle velocity space model

In this section, we derive an analytical model for an alpha particle velocity distribution f_α, that undergoes a thermal quench. The derivation was done together with co-author O. Embreus in paper B. Starting point is the isotropic kinetic equation for fusion-born alpha particles (eq. (2.14)), that is used to derive the steady-state solution f_0 (eq. (2.16)). We assume isotropy, motivated by the numerical results presented in section 5.2.1.

From D-T fusion, alpha particles emerge isotropically at a velocity $v_{\alpha 0}$. Its distribution in velocity follows the kinetic equation:

$$\frac{\partial f_\alpha(v,t)}{\partial t} = \frac{1}{v^2 \tau_s}\frac{\partial}{\partial v}\left[\left(v^3 + v_c^3\right) f_\alpha(v,t)\right] + \frac{S_\alpha \delta(v - v_{\alpha 0})}{4\pi v_{\alpha 0}^2}, \tag{5.5}$$

where the birth process is described by the fusion strength S_α and the particle distribution is shaped by the slowing-down time τ_s and the cross-over velocity v_c. As derived in more detail in section 2.1.1, τ_s represents a time-scale for alpha-electron collisions and v_c is a threshold velocity above which alpha-ion collisions dominate. They are given as:

$$v_c^3 = v_{th,e}^3 \frac{3\sqrt{\pi}\, m_e}{4 m_\alpha} Z_1, \tag{5.6}$$

$$\tau_s = \frac{3 m_\alpha m_e}{16\sqrt{\pi}\, Z_\alpha^2 e^4 \ln\Lambda}\frac{v_{th,e}^3}{n_e}, \tag{5.7}$$

$$Z_1 = \sum_i \frac{n_i Z_i^2 m_\alpha}{n_e m_i}, \tag{5.8}$$

where $v_{th,e} \equiv \sqrt{2T_e/m_e}$ is the thermal electron velocity, T_e the electron temperature, m_e the electron mass, m_α the alpha particle mass, Z_α is the alpha particle charge, e the elemental charge, $\ln\Lambda$ is the Coulomb logarithm and n_e is the electron density. Z_1 is a mass-averaged charge quantity, which is obtained through a summation over all background ion species i. The dependencies on global plasma parameters are

$$v_c^3 \propto \frac{T_e^{3/2}\sum_i n_i Z_i}{n_e},$$

$$\tau_s \propto \frac{T_e^{3/2}}{n_e},$$

with a weak dependence on T_e and n_e in $\ln\Lambda$, which is not displayed in the proportionality, but retained for the calculation.

In steady-state, $\partial f_\alpha/\partial t = 0$, this equation is solved by the slowing-down distribution [86]

$$f_0(v) = \frac{S_{\alpha 0}\tau_{s0}}{v^3 + v_{c0}^3}\mathrm{U}(v_{\alpha 0} - v), \tag{5.9}$$

in which we denote the steady-state parameters with an additional subscript 0, indicating that it serves as an initial condition. Doing so assumes that the alpha particles have reached the state f_0 prior to the thermal quench.

The disruption will be modeled with an exponential thermal quench that initiates at $t = 0$, when we also assume a stopping of the fusion process, hence the source strength $S_\alpha = S_{\alpha 0}$ is a constant. Meanwhile, the plasma densities n_e and n_i and charges Z_i are also allowed to change. The alpha distribution becomes explicitly described by v_c and

τ_s, which are functions of plasma parameters (mainly T_e and n_e) evolving in time. In the time-dependent equation, the fusion strength is set to zero and the Fokker-Planck equation now reads

$$\tau_s \frac{\partial f_\alpha(v,t)}{\partial t} - \frac{1}{v^2}\frac{\partial (v^3+v_c^3) f_\alpha(v,t)}{\partial v} = 0,$$

which can be solved utilizing a generic function F

$$\begin{aligned} f_\alpha(v,t) &= \frac{1}{v^3+v_c^3} F\left(\int^t \frac{\mathrm{d}t}{\tau_s} + \int^v \frac{v^2 \mathrm{d}v}{v^3+v_c^3}\right), \\ &= \frac{1}{v^3+v_c^3} F\left(\underbrace{\int^t \frac{\mathrm{d}t}{\tau_s} + \frac{1}{3}\ln(v^3+v_c^3)}_{\equiv G(v,t)}\right). \end{aligned}$$

With the initial condition, $f_\alpha(v,t=0) \overset{!}{=} f_0(v)$, we are able to drop the time-dependency in $G(v,t)$ and express v in terms of $G_0 \equiv G(v,t=0)$,

$$v = (\mathrm{e}^{3G_0} - v_c^3)^{1/3}.$$

Through rearrangement of the initial condition, we obtain $F(G_0)$ as

$$F(G_0) = \tau_{s0} S_{\alpha 0} \frac{v^3+v_c^3}{v^3+v_{c0}^3} \mathrm{U}(v_{\alpha 0} - v) = \frac{\tau_{s0} S_{\alpha 0}}{1 + (v_{c0}^3 - v^3)\mathrm{e}^{-3G_0}} \mathrm{U}(v_{\alpha 0} - v).$$

Restoring the time-integral in $G(v,t)$, a general time-dependent solution yields

$$\begin{aligned} f_\alpha(v,t) &= \frac{1}{v^3+v_{c0}^3} \frac{\tau_{s0} S_{\alpha 0}}{1 + (v_{c0}^3 - v^3)\mathrm{e}^{-3G(v,t)}} \mathrm{U}(v_\alpha - v), && (5.10) \\ &= \frac{\tau_{s0} S_{\alpha 0}}{v^3 + v_c^3(1 - e^{-3\int \tau_s^{-1} \mathrm{d}t}) + v_{c0}^3 e^{-3\int \tau_s^{-1} \mathrm{d}t}} \mathrm{U}(v_\alpha - v). && (5.11) \end{aligned}$$

The “birth” velocity v_α that limits the energetic tail of the velocity distribution is now time-dependent and can be obtained by rearranging $G(v_\alpha, t)$:

$$v_\alpha \equiv \left[(v_{\alpha 0}^3 + v_c^3) e^{-3\int_0^t \tau_s^{-1} \mathrm{d}t} - v_c^3\right]^{1/3}. \qquad (5.12)$$

At the initial point in time, $v_c = v_{c0}$ and $v_\alpha = v_{\alpha 0}$ holds, so we obtain $f_\alpha(v,0) = f_0$ as expected. In a thermal quench,

$$\lim_{t\to\infty} \exp\left(-3\int_0^t \tau_s^{-1}(t) \mathrm{d}t\right) = 0$$

and

$$\lim_{t\to\infty} v_c^3(t) = 0,$$

but because the exponential approaches zero faster, the inside of the bracket $v_\alpha = [\cdot]^{1/3}$ becomes negative and v_α imaginary. As this is unphysical, the model is only valid until v_α reaches zero, from which on the energetic tail has ceased to exist. This behavior can be resolved by absorbing the slowing-down particles into a Maxwellian (of Helium-ash), but is not part of our model as we are interested in the energetic particles only.

Furthermore, we will approximate the unit step function $\mathrm{U}(x)$ with the aid of the complementary Error function $\mathrm{Erfc}(x)$:

$$\mathrm{U}(v_\alpha - v) \longrightarrow \frac{1}{2}\mathrm{Erfc}\left(\frac{v - v_\alpha}{\Delta v}\right). \tag{5.13}$$

where Δv describes the velocity spread at birth and can be calculated from a thermal alpha particle velocity at background electron temperature [88] $\Delta v \equiv \sqrt{2T_e/m_\alpha}$.

Important moments of the velocity distribution yield the alpha density n_α and the alpha pressure p_α:

$$n_\alpha = \int f_\alpha(v,t)\mathrm{d}v, \tag{5.14}$$

$$p_\alpha = \frac{m_\alpha}{3}\int v^2 f_\alpha(v,t)\mathrm{d}v. \tag{5.15}$$

The velocity space model now consists of equations (5.11), (5.12) and (5.13), which depend on the evolution of parameters v_c and τ_s via background quench evolution. It derives from a simplified, isotropic Fokker-Planck collision operator in a uniform plasma. Relativistic effects are not included as the Lorentz factor for alpha particles at birth is $\gamma \equiv 1/\sqrt{1 - v_{\alpha 0}^2/c^2} = 1.0009$. In the following, the model will be applied for an ITER plasma disruption and validated against the numerical code CODION.

5.2.3 Validation and discussion of the analytical model

Present section is dedicated to validation by applying the velocity space model onto an ITER case and a general discussion of the alpha particle slowing-down process. This will also lay the ground for section 5.3.2, where the simulation space of this section is extended further. Since CODION has been equipped with a fusion source (section 4.1), it is a good candidate for a validation of the model. We also want to extend the discussion around the isotropy assumption, which so far has only been explicitly shown to be valid for a specific thermal quench scenario (section 5.2.1).

We use the 15 MA burning ITER scenario, which is introduced in section 5.1 and its plasma parameters are shown in figure 5.1. For the time being, only the inner-most radial point, $r = 0$, is considered. The fusion source magnitude is calculated from the equal D-T densities n_{DT0}

$$S_{\alpha 0} = n_{\mathrm{DT0}}^2 \langle \sigma v \rangle$$

and the D-T fusion cross-section [174]

$$\langle \sigma v \rangle = 3.68 \cdot 10^{-18}\, T_{i0}^{-2/3} \exp\left(-19.94\, T_{i0}^{-1/3}\right)\ \mathrm{m}^{-3}\mathrm{s}^{-1}.$$

A reaction rate for D-D fusion is not included as it is generally two orders of magnitude lower. With this input, one can already establish the steady-state distribution f_0 (eq. (5.9)) and calculate the alpha particle density on axis to be roughly $n_\alpha \approx 0.9 \cdot 10^{-2} n_{e0}$. This value is slightly higher (by $\approx 5\%$) than in ITER predictive studies [19] and is kept constant throughout the simulation.

A thermal quench is modeled with an exponential decay in temperature (eq. (5.1)) and the density is allowed to change according to a step-function increase (eq. (5.2)). For

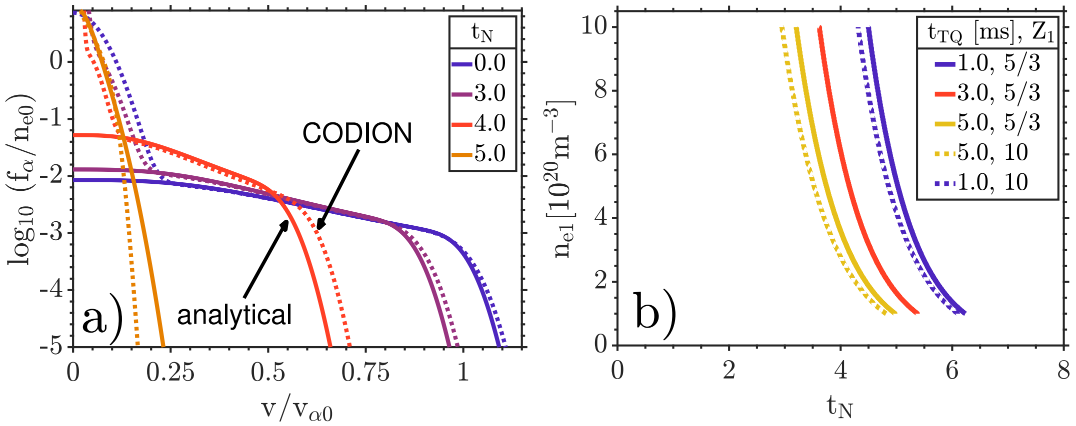

Figure 5.8: a) The evolving isotropic alpha particle distribution function $f_\alpha(v,t)$ for an exponentially cooling ITER core plasma, computed with the analytical model (solid) and compared against a CODION simulation (dotted). Colors indicate time. Note that both solutions conserve particle density (integral), but only CODION includes a Maxwellian. As the temperature decay initiates ($t_{\mathrm{TQ}} = 1\,\mathrm{ms}$), the electron density is raised to $n_{e,1} = 4n_{e,0} = 4{\cdot}10^{20}\,\mathrm{m}^{-3}$ by a singly ionized 50%-50% neon+deuterium injection. b) Figure shows the time-point of the cut-off velocity v_α (eq. (5.12)) reaching zero as a function of $t_N = t/t_{\mathrm{TQ}}$ and the post-disruption density n_{e1}. Colors indicate different quench times. While $Z_1 = 5/3$ represents a pure D-T plasma, the dashed lines yield the solution of a plasma with $Z_1 = 10$.

the validation case, the plasma density is raised by a 50%-50% singly ionized mixture of neon and deuterium to a value of $n_{e1} = 4n_{e0}$. Shown in figure 5.8a) is $f_\alpha(v,t)$ of thermal-quenching plasma with $t_{\mathrm{TQ}} = 1\,\mathrm{ms}$. The analytical results are compared to CODION simulations with a generally good agreement. Note that the CODION distributions include the Maxwellian of background temperature. At the initial time-point $f_\alpha = f_0$, for which the cross-over velocity equates to $v_{c0}/v_{\alpha 0} \approx 0.44$. Because $v_{\alpha 0} \ll v_{th,e}$, velocities even beyond the birth velocity can be reached through collisions with thermal electrons. This energy diffusion effect [88] is represented by Δv in eq. (5.13) and is included in CODION as well.

As the background plasma temperature decays, the cross-over velocity $v_c \propto T_1^{1/2}$ shrinks as does the governing collision time-scale $\tau_s \propto T_1^{3/2}$. This facilitates an initially slow, but accelerated cooling of the energetic alpha tail and is represented by the integral in the expression for the cut-off velocity v_α in equation (5.12). The energetic alphas are able to withstand the deceleration for roughly $t_N = 2 \mathrel{\widehat{=}} 2\,\mathrm{ms}$. Because the density is conserved, the slowed-down particles progressively pile up at lower energies. The EP distribution at $t_N = 5$ is similar in width to the initial Maxwellian of ≈ 21 keV[1], while the actual background temperature has reached approximately 400 eV already.

In order to investigate, how the alpha particle thermalization is affected by the plasma composition and pace of the thermal quench, we create a parameter space $[n_{e1}, Z_1, t_{\mathrm{TQ}}]$ and measure the time-point of v_α (eq. (5.12)) reaching zero. This approximates the complete thermalization of the energetic tail. The parameter Z_1 is used to represent the composition of the plasma. A pure D-T plasma yields $Z_1 = 5/3$, while the validation case raises this value to $Z_1 = 2.6$. Figure 5.8b) shows the results of the parameter space scan. An increase in electron density causes the alpha tail to slow down 'quicker' in

---

[1] Collisions at $v < v_c$ are dominated by alpha-ion collisions, hence the Maxwellian is roughly at the ion temperature.

reference to the background temperature ($t_N \sim T_1$), as more collision targets become available and the slowing-down time τ_s drops. The discrepancy between various thermal quench times comes from a deviation of the elapsed time $t = t_N t_{\mathrm{TQ}}$ to slowing-down time τ_s, the latter of which is independent of t_{TQ}. Essentially, a slower quench leaves the particles more time to collide, before a certain temperature ($\sim t_N$) is reached. We raise the mass-weighted charge Z_1 of the plasma from 5/3 to 10, which for the velocity distribution raises the cross-over velocity $v_c \propto Z_1^{1/3}$. This increases the fraction in velocity space that is dominated by alpha-ion collisions and explains the more effective slowing-down of the alphas.

The isotropy assumption for the velocity distribution has been shown to remain valid (section 5.2.1) for an unmitigated disruption case ($n_{e1} = n_{e0} = 10^{20}\,\mathrm{m}^{-3}$, $t_{\mathrm{TQ}} = 1\,\mathrm{ms}$ and $Z_1 = 5/3$) and can now be discussed for mitigated cases. The anisotropy-inducing electric field develops, as the plasma conductivity $\sigma \propto T_1^{-3/2}$ shrinks. In the simplifying assumption, that the injected material does not affect the temperature evolution in the TQ (i.e. assuming that the heat loss is dominated by MHD losses [104]), the electric field becomes independent of n_{e1} and Z_1 and evolves with t_N, which equates a temperature. The unmitigated case remains isotropic until at least $t = 8t_N$, see figure 5.7. Mitigation systems raise n_{e1} and Z_1 and thereby accelerate the alpha thermalization (figure 5.8b)). Thus, the isotropy assumption is maintained for the mitigated cases and for the thermal quench timescales considered in this work ($t_{\mathrm{TQ}} \geq 1\,\mathrm{ms}$).

We have showed the application of CODION in the calculation of alpha particle distributions for ITER. The general observation [78] is that the alphas remain an EP species distinct from the thermal bulk for a considerable amount of time. Thus an EP mode-driving force during the TQ of the plasma is present. We realized that the disruption-induced electric field has negligible effect on the alphas, hence an analytical model was developed that shows good agreement with the numerical results [79]. In section 5.3 this model will be utilized to cheaply perform parameter space scans and calculate the alpha drive for the TAEs obtained in section 5.1.

5.3 Wave-particle interaction in the post-disruption plasma

This section is dedicated to the calculation of the wave-particle interaction between the alphas and post-disruption TAEs. The mode evolution of a TAE is determined by the competition of damping effects of the bulk plasma and a driving force, that originates from the alpha particle spatial pressure gradient (section 2.4). Approximate analytical formulae exist [46], but we compute the interaction numerically with HAGIS (section 3.5). The required input consists of the plasma equilibrium, the mode eigenfunctions and damping as well as some representation of the energetic particles. As such, the input is a combination of our knowledge gained from the previous sections, i.e. the Alfvén spectrum/damping and equilibrium in section 5.1 and the alpha particle model in section 5.2.

Section 5.3.1 describes the wave-particle evaluation in detail, that is then extended to a parameter space evaluation in section 5.3.2. The parameter space covers the effects of plasma composition, thermal quench times and introduces a diffusive transport model to the alpha particle distributions.

5.3.1 TAE mode evolution during an unmitigated ITER plasma disruption

Again, we use the burning ITER 15 MA scenario, that suffers an unmitigated disruptive event described by an exponential thermal quench with $t_{\mathrm{TQ}} = 1\,\mathrm{ms}$. The plasma is divided into 101 radial points r/a and populated with velocity distributions $f_\alpha(v, r, t)$ calculated by the analytical model established in section 5.2.2. Analogous to how CODION-calculated distributions were transferred (see section 4.2, without the fitting), $f_\alpha(v, r, t)$ is imported into HAGIS for some point in time via

$$f_\alpha(v, r) \to f_{\mathrm{HAGIS}}(v, s) = f(s) f(v), \tag{5.16}$$

$$f(v) = \frac{\mathrm{Erfc}\left[(v - v_\alpha)/\Delta v\right]}{v^3 + v_c^3(1 - e^{-3\int \tau_s^{-1}\mathrm{d}t}) + v_{c0}^3 e^{-3\int \tau_s^{-1}\mathrm{d}t}}, \tag{5.17}$$

$$f(s) = n_\alpha(s)/n_\alpha(0), \tag{5.18}$$

where v_c, v_α, τ_s and Δv are also functions of s. The transformation inherently assumes $r/a \approx s$, i.e. that the plasma described by the flux surface label s is approximately circular. HAGIS is able to use VMEC-generated equilibria and we import the plasma equilibrium established in section 5.1. Mode eigenfunctions M_1 and respective damping levels are transferred from LIGKA simulations of the same section. The beginning timepoint for the HAGIS simulations is chosen to be $t_N = 1.5$ and is justified by the low damping values (see figure 5.5). The Alfvén velocity for the unmitigated ITER plasma is $v_A/v_{\alpha 0} \approx 0.58$ and for TAEs the most fundamental resonances occur at v_A and $v_A/3$ (section 2.4). At $t_N = 1.5$ this velocity space region is well populated by alpha particles at this point in time (see figure 5.7 or figure 5.8).

The modes are perturbations, whose amplitude is measured in $\delta B/B$, where B the local magnetic field strength. Each mode is initialized with $\delta B/B = 10^{-10}$ and the alpha particle distribution is represented by a total of 10^5 markers. The time-integrator is set to conduct 256 time-steps per wave-period which approximates to roughly $5 \cdot 10^{-7}\,\mathrm{s}$ (varies for each toroidally distinct wave). In the simulation the alpha particles interacting with the TAEs are redistributed by HAGIS in both space and energy, but the collisional slowing-down process due to the further shrinking background temperature is not taken into account by the HAGIS model. The mode damping values at $t_N = 1.5$ are taken as constant throughout the simulation. We limit the simulation duration to the point of complete alpha particle slow-down (see figure 5.8b), however, we will see that the growth is strong enough for the modes to saturate well before the alphas thermalize.

The wave-particle interaction is calculated with the M_1 set of modes (section 5.1), which are the even TAEs found in the inner plasma, $0 < s < 0.5$. Figure 5.9a shows the evolution of their amplitudes as driven by the alpha particles against the weakly damping post-disruption plasma. We observe a linear growth phase of $\approx 0.6\,\mathrm{ms}$, at which the growth rate is approximately $\gamma/\omega \approx 1.8\%$ [1/rad]. After the linear phase, the modes show non-linear behavior and saturate at an average amplitude of $\delta B/B \approx 0.1\%$. The non-linearities are due to particle redistribution and are not observed when the simulation is run with a single toroidal mode. Particularly standing out are the $n = 8$ and $n = 9$ modes which are the modes with the lowest - essentially none - damping (figure 5.5a)). These two TAEs briefly reach amplitudes of $\delta B/B \lesssim 1\%$, which requires us to take the result with caution. It is known [183], that due to a lack of *zonal-flow physics* [184] and mode-mode coupling effects, the HAGIS model can overestimate the mode amplitudes. As such, the mode amplitudes are treated as an upper limit. More modest values are observed with a larger set of modes: For computational reasons associated with a parameter scan (and because damping-to-drive ratio increases in the

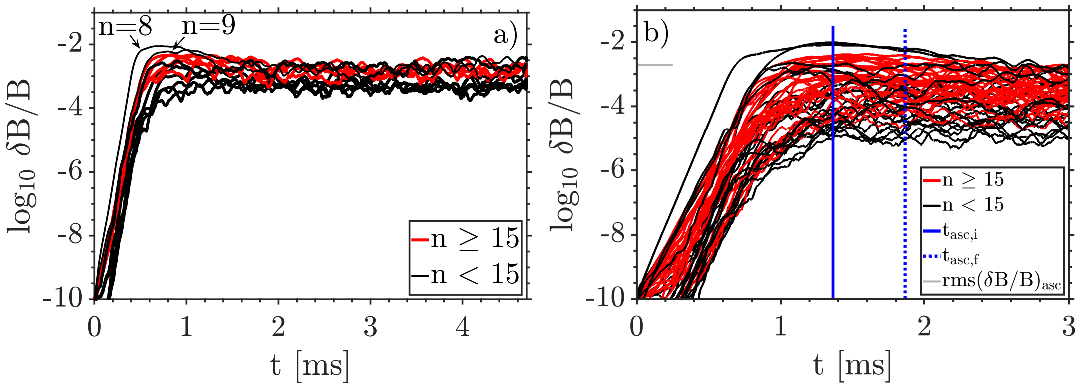

Figure 5.9: Evolution of TAEs with toroidal mode number n in an unmitigated post-disruption ITER plasma as driven by alpha particle population. Figure a) shows the simulation with the mode set M_1 (only inner half of the plasma, even parity), while figure b) shows the same simulation with modes of the entire plasma taken into account (M_2, odd parity added). The end of the simulation in a) corresponds to the time-point of complete alpha slow-down $v_\alpha(s = 0) = 0$. Legend entries with subscript "asc" in figure b) refer to a later usage in section 5.4. All poloidal harmonics are included for the simulation and the displayed data is slightly smoothed for the purpose of illustration.

radial direction outwards), the LIGKA-Eigenmode searcher for M_1 was restricted to the inner half of the plasma and to even parity TAEs. We lift these restrictions and repeat one HAGIS computation with a new set of LIGKA-eigenmodes, M_2, that includes all the TAEs in the plasma. Its modes have toroidal mode numbers ranging $n = 6 - 26$, with some gaps populated with more than one TAE (even, odd), totaling in 62 toroidal modes with up to 17 poloidal mode numbers. The mode evolution of M_2 is depicted in figure 5.9b, showing a balanced distribution of energy among the modes. Because of the particle redistribution, even the newly included modes at $s > 0.5$ receive drive from the alpha particles. The strongest driven mode is still the (even) $n = 8$, however with a slightly reduced growth rate. Part of the low-n branch (black) now saturates at $\delta B/B \approx 10^{-5}$ and consists of odd parity TAEs that receive generally less EP drive.

The large amplitudes of the TAEs suggest, that RE transport is likely [33, 77]. With M_2, the requirement on resolution drastically increases and becomes very demanding on the HAGIS code. With this expanded set of modes we will be conducting a self-consistent simulation of a disrupting plasma in section 5.4. However, due to computational costs the M_1 set of modes will be used for the parameter space evaluation. The strong amplitudes obtained with M_1 and M_2 are treated as an upper limit.

5.3.2 TAE mode evolution in a mitigated ITER plasma disruption and the effects of alpha particle diffusion

The calculations of the previous sections are expanded to learn about the effects that varying quench times, disruption mitigation techniques and alpha particle losses might have on the destabilization of TAEs. For this, the wave-particle interaction simulations are conducted in a parameter space $\mathbf{A} \equiv [D_\alpha, t_{\mathrm{TQ}}, n_{e1}, n_{\mathrm{NE1}}/n_{D1}]$, which covers the thermal quench time t_{TQ}, the post-disruption electron density n_{e1}, the fraction of neon injected n_{NE1}/n_{D1} and where we add an alpha particle diffusion parameter D_α (defined below) in addition to the resonant EP transport in the HAGIS model.

A plasma disruptive event is regularly accompanied by a breaking-up of the confining magnetic flux services. While the plasma surfaces heal again, the high-velocity alpha particles are susceptible to being transported out of the plasma. Precisely quantifying the disruption-induced transport is hard to assess without costly and parameter-rich numerical simulations and will instead be addressed with a diffusion model for the alpha particles.

We return to the alpha particle description and treat the spatial problem of diffusion separately from our velocity space solution. The one-dimensional diffusion equation for the alpha particle density $n_\alpha(r,t)$ states:

$$\frac{\partial n_\alpha(r,t)}{\partial t} = \frac{\partial}{\partial r} D \frac{\partial}{\partial r} n_\alpha(r,t) \approx D(t) \frac{\partial^2 n_\alpha(r,t)}{\partial r^2}, \tag{5.19}$$

where $D(t)$ is a time-dependent diffusion strength, independent of velocity and radius. Boundary conditions are (1) a flat gradient at the core, $\partial n_\alpha(0,t)/\partial r = 0$ and (2) an open boundary at the edge of the plasma, $r = a$, allowing an outflow of alpha particles. Equation (5.19) is solved numerically with the Crank-Nicolson method and applied on the density gradient before the particle distribution is imported into HAGIS. The diffusive process begins at $t = 0$ and runs until the initial point of the wave-particle interaction calculation. For simplicity, we assume that this diffusion only affects the alphas and not the background plasma. The time-dependence of the diffusion strength is introduced to account for a healing of the magnetic flux surfaces. In a recent study on the medium sized ASDEX Upgrade tokamak [185] a healing rate at the time-scale of the thermal quench was successfully used to match experimental data on MMI-injected argon transport, therefore we use

$$D(t) = D_\alpha \mathrm{e}^{-t_N}, \tag{5.20}$$

with an initial diffusion coefficient D_α. The extrapolation from the AUG study assumes the diffusive process to be independent of particle mass and machine size. With a parametrization of the diffusion coefficient D_α we will cover cases where (1) no alpha particles are lost up to cases where (2) the transport renders the wave-particle interaction mechanism increasingly insignificant. The reasoning for (1) originates from evidence of post-disruption EP confinement in the plasma core [186]. Such a strongly confining case is of particular interest, because under such circumstances the (generally faster, core-localized) RE seed electrons are also not expelled and bear a risk of generating a dangerous RE beam. This assessment will be discussed by the end of the section. The magnitudes chosen for (2) are deemed realistic and are taken from our knowledge about current (medium-sized) tokamak experiments [187] (results of discussions with various experts from the disruption community). Furthermore, we require the alpha particle radial profile to be unaffected by transport prior to the disruption occurring. Effects like electrostatic microturbulence can change the general slowing-down shape into “bump-on-tail-like” energy distributions [188], which would also have effects on the wave-particle interaction. An example of the diffusion acting on an alpha particle profile $n_\alpha(r,t)$ is shown in figure 5.10a), besides a simple validation simulation (as the Crank-Nicolson script was written from scratch).

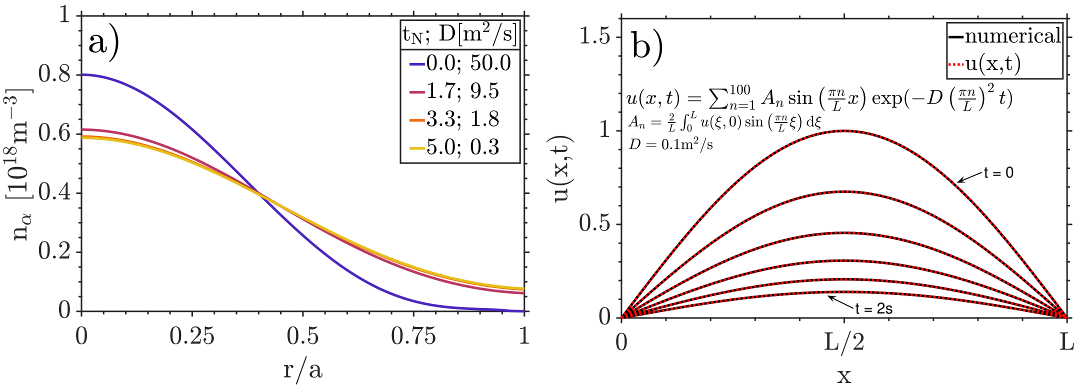

Figure 5.10: a) Example of a diffusion of alpha particles according to eq. (5.20) with an open boundary at the plasma edge, calculated by a Crank-Nicolson method. b) Validation of the Crank-Nicolson implementation against a well-known analytical solution of the 1D diffusion equation. Boundary conditions are $u(0,t) = u(L,t) = 0$ and the initial function is a $2L$-periodic sinus function.

A parameter space $\mathbf{A}$ is defined with values representative of the ITER experiment

$$\begin{aligned} D_\alpha &= [1, 100]\,\mathrm{m}^2/\mathrm{s}, \\ t_{\mathrm{TQ}} &= [1, 3]\,\mathrm{ms}, \\ n_{e1} &= [1, 1.5, 2, 2.5, 3, 3.5, 4]\ n_{e0}, \\ n_{Ne1}/n_{D1} &= [0, 0.1, 1.0], \end{aligned}$$

with singly ionized neon, totalling 84 combinations. Every parameter affects the particles and we obtain distribution functions $f_\alpha(v, r, t, \mathbf{A})$ for each combination in the parameter space. The analytical model is used for the velocity distribution. Damping values obtained through LIGKA stay unaffected by D_α and t_{TQ}, because the initial time-point for the wave-particle calculations remains $t_N = 1.5$, i.e. at the same plasma temperatures. Damping values as a function of electron density n_{e1} and neon composition n_{Ne1}/n_{D1} are found in figure 5.6, while the effect of n_{e1} and t_{TQ} on the alpha slowing-down are illustrated in figure 5.8b).

The wave-particle interaction calculations are conducted with the M_1 set of modes and the numerical setup described in section 5.3.1. The perturbations are evaluated in terms of the maximum (max $\delta B/B$) and root-mean-square values (rms $\delta B/B$) of their amplitudes and are summarized in figure 5.11. Figure 5.12 is part of a sensitivity scan that serves a discussion on the longevity of the perturbations. Its calculations differ through the usage of more thermalized alpha particle distributions, obtained for the time-point $t_N = 3.5$.

Generally we find, that alpha transport and material injection reduces the perturbation amplitudes, especially when neon is involved. We begin a more detailed discussion on the LHS of figure 5.11 (a) and c)). Apparent is an overall drop in perturbation amplitudes, as the post-disruption electron density n_{e1} rises. This can be explained with the damping rate dependencies (figure 5.6), that generally grow with the electron density, but show a local minimum at $n_{e1} = 2n_{e0}$, which in turn causes a local maximum in the perturbation amplitudes for the $D_\alpha = 1\,\mathrm{m}^2/\mathrm{s}$ cases. In addition, the growing electron density affects the alpha velocity distributions, providing more collision targets and cause a faster deceleration of the energetic alpha tail. The influence of this accelerated thermalization can be separated from the damping strength's influence by looking at the simulation results for a different thermal quench time t_{TQ}. The LHS of

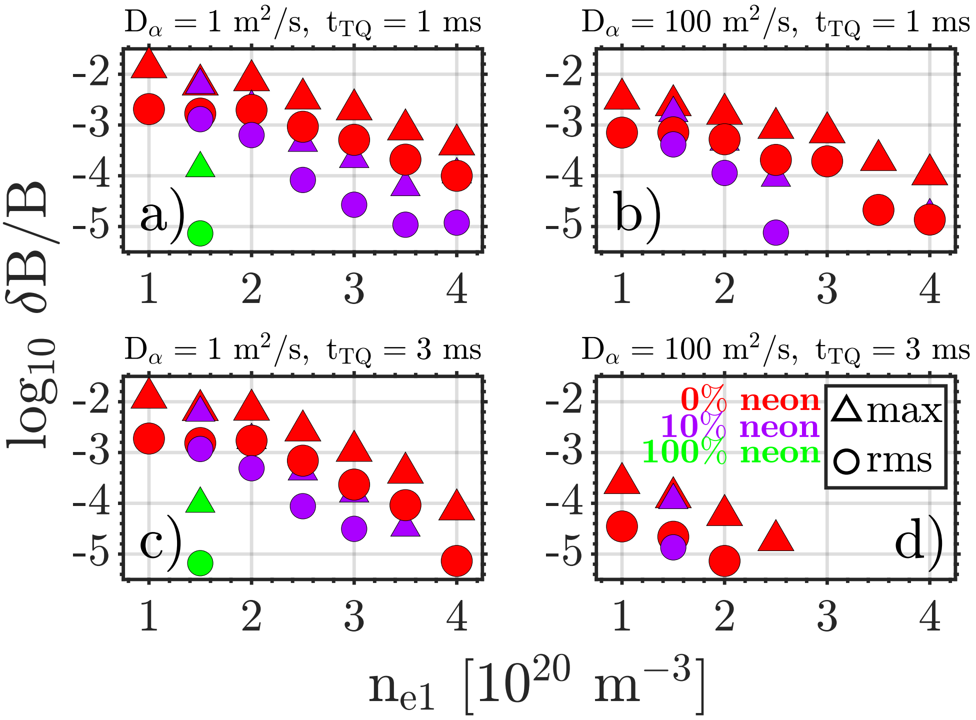

Figure 5.11: Evaluation of maximum (max, triangle) and root-mean-square (rms, circle) of the mode amplitudes $\delta B/B$ reached by post-disruption M_1 TAEs resonating with alpha particles. The mean values are calculated after 3 ms into the simulation. Red, purple and green colors represent 0%, 10% and 100% neon injection, rest deuterium. The simulation is conducted with the HAGIS code where all modes are initialized with an initial perturbation amplitude of $\delta B/B = 10^{-10}$. The initial time-point of the simulation corresponds to a global time of $t_N = 1.5$ after the thermal quench has begun. The energetic alpha particle distributions are also calculated for the time-point $t_N = 1.5$.

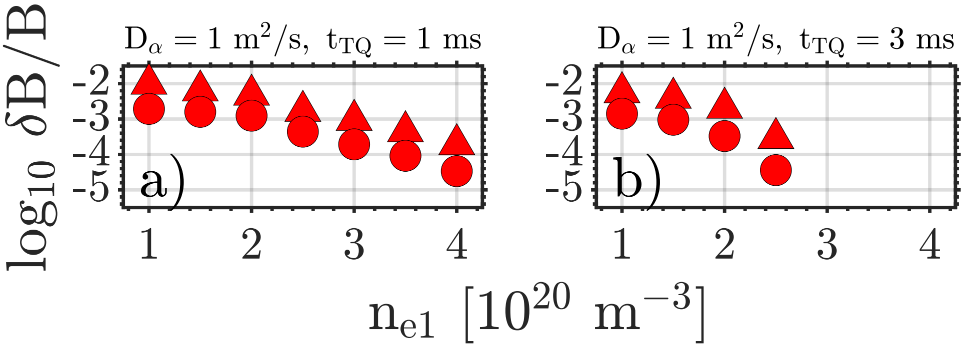

Figure 5.12: Same as figure 5.11, but the energetic alpha particle distributions are calculated for the time-point $t_N = 3.5$.

figure 5.11 represents such a comparison and shows a strong similarity in mode amplitudes for cases where the electron densities are close to the pre-disruption condition. Although the background temperature profile stays the same, a slower decay time t_{TQ} grants the alpha particles more time to decelerate until $t/t_{TQ} \equiv t_N = 1.5$ is reached.

Meanwhile, the damping is a function of temperature and therefore in our simulations is independent of t_{TQ}. The difference between the $t_{\mathrm{TQ}} = 1\,\mathrm{ms}$ and $t_{\mathrm{TQ}} = 3\,\mathrm{ms}$ perturbation amplitudes increases with a rising electron density $n_{e1} \to 4n_{e0}$ and are due to an accelerated slowing-down of the alpha particles.

The amount of neon in the injection modeling is distinguished by colors, where red is 0%, purple 10% and green 100% neon. Adding neon to the plasma increases its mass and affects the alphas via Z_1 (eq. (5.8)), which ranges from $Z_1 = 5/3$ to $Z_1 \approx 3$ for the highest amounts of neon in our simulations. As shown in figure 5.8b, the influence of Z_1 on the EP slow-down is less significant, than the neon effect on the damping (figure 5.6b)). As more neon is added to the plasma its mass density ρ grows and reduces the Alfvén velocity $v_A \propto \rho^{-1/2}$, causing the TAE to now resonate with less energetic particles. These effects cause the observed reduction in perturbation amplitude, from which we conclude that a neon presence is very effective in terminating the alpha-driven TAEs.

Increasing the diffusion strength D_α (RHS of figure 5.11) yields a stronger flattening of spatial alpha particle gradient. As expected, this causes a drop in mode drive and we find, that with $D_\alpha = 100\,\mathrm{m}^2/\mathrm{s}$, $t_{\mathrm{TQ}} = 1\,\mathrm{ms}$ the perturbation levels are overall an order of magnitude lower than without diffusion. With a slower thermal quench our diffusion equation models a slower healing of the confining flux surfaces and the impact of the gradient flattening becomes stronger overall. This effect stacks on top of the quench time influence on the alpha particle deceleration discussed above and even modest amounts of injection have strong impact on $\delta B/B$.

We want to address the fact, that for the duration of the HAGIS simulation a further slowing-down of the alpha population due to the sinking background temperatures cannot be taken into account. Particles are redistributed in space and energy, however, only due to the energy transfer towards the TAEs. For a sensitivity study, part of the parameter space simulations are now repeated with alpha distributions, that are obtained at a later time-point $t_N = 3.5$, hence are further slowed-down and less energetic. The rest of simulation setup remains the same. The results are shown in figure 5.12. Compared to the prior simulations, the alpha particles had an additional 2 ms (for $t_{\mathrm{TQ}} = 1\,\mathrm{ms}$) and 6 ms (for $t_{\mathrm{TQ}} = 3\,\mathrm{ms}$) to slow down. Note that the saturation of mode amplitudes (in the strongest driving, unmitigated case) takes approximately 1 ms (figure 5.9a)). Overall, for the parameter space of good confinement ($D_\alpha \approx 0$), the mode amplitudes are now reduced by a factor of 5, but remain significant. As seen in figure 5.8b, the alpha particles for $t_N = 3.5$ and $t_{\mathrm{TQ}} = 3\,\mathrm{ms}$ are very close to a complete thermalization and as such become increasingly unable to drive the TAEs.

We have collected information on the alpha particle driven TAEs and how their perturbation amplitudes are influenced by the injection of material, alpha particle diffusion and varying thermal quench times. The unmitigated and strongly confining case $\mathbf{A} = (D_\alpha = 1\,\mathrm{m}^2/\mathrm{s}, t_{\mathrm{TQ}} = 1\,\mathrm{ms}, n_{e1} = n_{e0}, n_{\mathrm{NE1}} = 0)$ yields the highest TAE amplitudes for the proposed mechanism. Disruption mitigation systems, which inject material into the plasma reduce the perturbation strengths, mainly by raising the damping of the bulk plasma. Neon proves especially effective in doing so. Our modeling assumes, that the material is deposited uniformly and instantly at the onset of the thermal quench. Should the inner plasma ($s \lesssim 0.5$) however remain close to its pre-disruption condition - hence also with strong alpha particle presence - one can expect significant TAE mode activity during the thermal quench. Certain scenarios of material deposition could even enhance the alpha mode drive: Because the energy is drawn from a radial gradient in the alpha particle pressure, a cold front that slowly moves inwards or does not penetrate all the way, could potentially raise the gradient. While this has not be considered here, the model presented in section 5.2.2 would allow an effective analysis.

The mechanism is sensitive to the transport of alpha particles. A disruption-induced destruction of the confining magnetic flux surfaces can cause losses of EPs. Intolerable heat loads onto plasma facing material is one of the dangers accompanied by disruptions [6]. Up to this date, quantifying the post-disruption transport remains an unsolved problem. However, a study suggest [186], that the stochastic transport during the thermal quench decreases fast with the size of the machine and a confinement of EPs in the core can be maintained for ITER-sized tokamaks. This however remains to be confirmed. Core confinement of a RE beam for up to 1 s has been observed [189] at the TCV tokamak [190]. While a core confinement of REs during the thermal quench is detrimental to MMI-based RE mitigation attempts, it bodes well for the alpha-driven TAEs.

With D_α close to zero, we considered a case of near perfect post-disruption confinement of the core plasma. While this seems possible [186], it is not a given situation and a breakup of magnetic surfaces may cause strong transport of the alpha particles and reduce the TAE perturbation strengths. However, the relevance of the alpha-TAE interaction we research in this work, ultimately comes down to the TAE interaction with REs (section 5.4). Runaway electrons and alpha particles share a common trait, which is their high velocity making them susceptible to losses. As REs posses speeds that are even larger the alpha particles, it can be assumed that if the breakup of magnetic surfaces is sufficiently strong for a sufficiently long time, the runaway electron seed losses will be even larger than the alpha particle losses. In cases where the alpha particles are lost, the generation of a RE beam becomes less likely, although the RE seed population may be replenished by the constant source of Compton scattering and tritium decay (see section 5.4). The necessity for RE mitigating effects, which we study in the next section, becomes less likely in scenarios where the alpha particles population is diminished.

In the following section, a disruption simulation is performed, where effects of the established TAEs on RE generation are studied. Because the mechanism evolves naturally in the plasma and without external influence, it is an inherent and passive effect and could possibly aid RE mitigation attempts. For the reasons mentioned above, we consider a scenario, where the healing of the broken up flux surfaces is fast enough to keep both the alpha particles and runaway electrons well confined, as this is the most relevant case for the TAE-RE interaction. We further consider the worst-case scenario, by looking at an unmitigated disruption, which we found to yield the highest perturbation amplitudes.

5.4 Self-consistent simulation of an unmitigated plasma disruption under the influence of alpha-driven TAEs

In the previous section we have established that when a D-T ITER plasma disrupts, it is able to utilize the energy of its lingering alpha particles to destabilize Alfvénic modes in the cooling plasma. The strengths of these perturbations were found to be significant enough to merit further investigation [33, 77, 78]. The perturbations develop in a highly dynamic phase of the plasma, during which also the generation of runaway electrons occurs. In this section we will compute how the TAEs of the unmitigated simulation, $\mathbf{A} = (D_\alpha = 1\,\mathrm{m}^2/\mathrm{s},\ t_{\mathrm{TQ}} = 1\,\mathrm{ms},\ n_{e1} = n_{e0},\ n_{\mathrm{NE1}} = 0)$, affect the generation process.

The first step consists of calculating the RE transport caused by the perturbations and a code, that is suitable for the task, is ASCOT5 (section 3.6). In a second step, the DREAM tool (section 3.7) will be applied. It calculates runaway electron dynamics in a disruption and - crucial for its application here - has the ability to include particle diffusion effects into the RE generation equations. The code application itself was performed by co-authors of paper B [79] K. Särkimäki (ASCOT5) and I. Pusztai (DREAM), while I provided the inputs and conducted the analysis of the outputs.

Markers, which are initially located at the same radial position are traced and their radial spreading in time is used to estimate the transport in form of a diffusion [167]. The diffusion coefficient is evaluated at various radial positions, where each position is initially populated by 500 markers, which are distributed uniformly toroidally and poloidally along a drift surface. The markers are chosen to represent REs and therefore are strongly passing with a pitch $\xi = p_\parallel/p = 0.99$. The simulation is repeated for electron energies [0.1,1,10] MeV. Neither the induced electric field nor Coulomb collisions are present in the simulation, so that all the observed transport is solely due to the magnetic field perturbations.

For the simulation, we use the M_2 set of TAEs and their perturbation strengths obtained for the unmitigated case $\mathbf{A} = (1, 1, 1, 0)$, which is the strongest driving case in our simulations. As it is also a case with $D_\alpha \approx 0$, we ignore our diffusion post-disruption transport model, that would otherwise also affect the REs. The plasma equilibrium used is the one obtained for the LIGKA and HAGIS simulations (section 5.1) and is converted into a suitable input for ASCOT using the code CHEASE [144]. It forms a $\kappa = 1.46$ elongated plasma, with $R_0 = 6.2\,\mathrm{m}$, $a = 2.06\,\mathrm{m}$ inside a vessel with a wall radius $b = 3.72\,\mathrm{m}$ and at a vertical displacement $Z = 0$. From the mode evolution of M_2 the root-mean-square amplitudes of $\delta B/B$ in the time-frame $t = t_{\mathrm{asc,i}} - t_{\mathrm{asc,f}}$ are calculated and displayed in the previous mode-evolution (figure 5.9b)). This specific time-frame is chosen, because at $t_{\mathrm{asc,i}} = 1.38\,\mathrm{ms}$ the $\mathrm{rms}(\delta B/B)$ has its maximum and the simulation is performed for 0.5 ms to allow particle orbits to become de-correlated. Eigenfunctions of M_2 are set to be constant for the duration of the ASCOT simulation.

The resulting perturbed plasma equilibrium is shown on the RHS of figure 5.13. The perturbation amplitude $\delta B/B$ is calculated locally at each grid point, with δB being the toroidal maximum of the strength of the 3D MHD-perturbation. Both the axis-symmetric field B and δB are calculated with all their components, i.e. toroidal, poloidal and radial contribution. One can see the most pronounced TAEs to reside in the inner half of the plasma, where TAE-driving alpha particles are most present. The perturbations are stronger on the low-field-side of the plasma, which is both due to the radial dependence of the toroidal magnetic field strength and due to the dominant TAEs being of even parity.

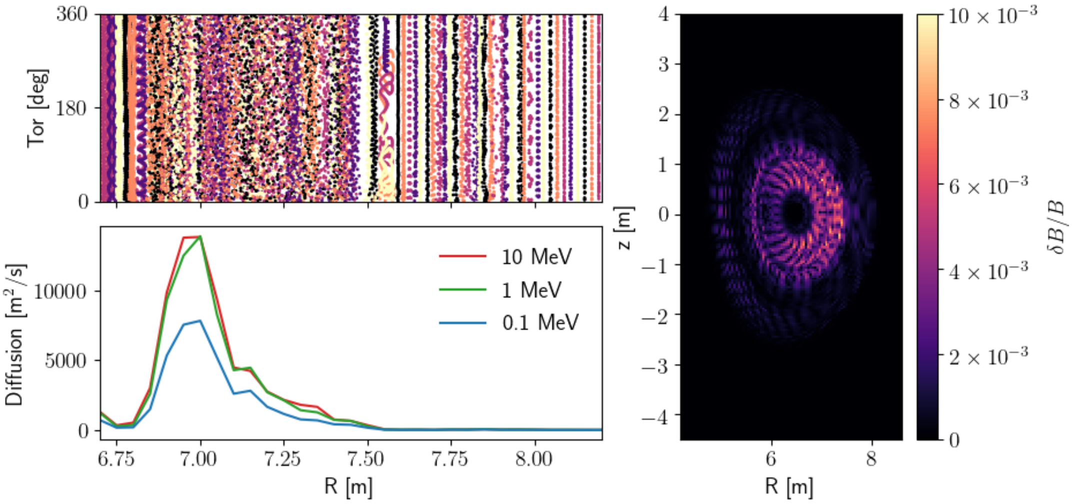

Figure 5.13: The plasma equilibrium (RHS) perturbed by M_2 Alfvénic modes, the Poincare plot (top left) for a 100 keV electron and the diffusion calculations (bottom left) for test-particles inside these perturbed flux surfaces.

Runaway electrons are launched parallel to the magnetic field line trajectories with kinetic energies $[0.1, 1, 10]$ MeV and are tracked throughout their motion in the plasma. Energy values and the parallel velocity direction is representative of a runaway electron accelerated by an induced electric field. Figure 5.13 (top left) shows a Poincare plot of the 100 keV electron, from which we expect increased transport in the region $R \approx 6.8 - 7.4\,\mathrm{m}$. A diffusion strength is calculated as a function of the particle momentum and radial position and displayed in figure 5.13 (bottom left). It peaks at $R \approx 7\,\mathrm{m}$ at value of $D = 13886\,\mathrm{m}^2/\mathrm{s}$. Using first principles [191] and an average perturbation strength of $\mathrm{rms}(\delta B/B) = 0.003$ one can estimate the diffusion of a fully stochastic magnetic field at the amplitude, yielding $D_{\mathrm{RR}} \approx R_0 c (\delta B/B)^2 = 16740\,\mathrm{m}^2/\mathrm{s}$. This analytical estimate is known [166] to significantly overestimate the transport in regions, where magnetic islands occur. As no major islands can form, the analytical and numerical value serve a good sanity check.

Until now, the disruption analysis in the previous sections has been conducted using multiple codes and models. In the following we will apply a single tool - DREAM - that is able to calculate the evolution of the background plasma, the induced electric field as well as runaway electron generation including their radial transport. We employ DREAM in its fully fluid mode, which often provides adequate results at significantly reduced computational cost [168]. Instead of resolving for entire phase-space RE distribution functions, the runaway current density j_{RE} is used to characterize the runaway species.

The bulk ion plasma is a pure 50-50 D-T plasma. The electron background is characterized by its density n_e, its temperature T_e and Ohmic current density j, of which the initial profiles are laid out in figure 5.1 and figure 5.2b). The initial temperature profile is evolved with the exponential temperature drop in eq. (5.1) at a quench time of $t_{\mathrm{TQ}} = 1\,\mathrm{ms}$, no material injection is performed and the current density is evolved self-consistently by DREAM. The geometric parameters R_0, a, b and κ are used to describe the magnetic field structure[2]. We assume zero triangularity and no Shafranov shift.

The ASCOT-obtained transport coefficients are given as functions of radius, normalized relativistic momenta $p \equiv \gamma v/c = (0.66, 2.78, 20.5)$ and are calculated for $p_{\|}/p \equiv \xi = 0.99$. These values are scaled for the DREAM simulation as follows: For particle momenta below $p = 0.66$, a linear scaling is assumed with $D = 0$ for electrons with $p = 0$. Above $p = 20.5$ the transport is assumed to remain constant, justified by the expected dependency $D \propto p/\sqrt{p^2+1}$ [192]. Consistent with the Rechester-Rosenbluth diffusion model [191] we assume a pitch-depend diffusivity $D \propto |\xi|$.

In order to account for momentum and pitch-dependent diffusivities, we have to assume some distribution function for the runaway electron species, as noted in section 3.7. As in the work by P. Svensson [9] we assume

$$
\begin{aligned}
f(r, p, \xi, t) &= \frac{A(p)}{2\sinh(A(p))} \mathrm{e}^{A(p)\xi} F(r, p, t), \\
F(r, p, t) &= n_{\mathrm{RE}}(r, t) \frac{\Gamma_{\mathrm{av}}\tau}{E - E_c} \mathrm{e}^{-\Gamma_{\mathrm{av}}\tau(p - p_{\mathrm{crit}})/(E - E_c)},
\end{aligned}
$$

where $A(p)^{-1} \equiv (p\nu_D\tau)/2E$ determines the extent of the distribution function in pitch ξ, ν_D is the pitch-angle collision frequency, $\tau \equiv m_e c/(eE_c)$ is the relativistic collision time between electrons, Γ_{av} is the avalanche source term computed by the DREAM model, E_c and p_{crit} are the critical electric field and critical momentum respectively, both accounting for partial ionization effects as in reference [107] (for p_{crit}) and reference [93] (for E_c). The above function $f(r, p, \xi, t)$ corresponds to a strongly forward beamed particle distribution (at large momenta p) that is dominated by avalanche and is a good approximation for avalanche generated beams [9, 77].

With the pitch-distribution of $f(r, p, \xi, t)$ the ASCOT-obtained diffusivities $D(p, \xi)$ are pitch-averaged

$$
\langle D \rangle_\xi(p) = \int_{-1}^{1} D(p, \xi) \frac{A\mathrm{e}^{A\xi}}{2\sinh A} \mathrm{d}\xi,
$$

and used to calculate the radial RE flux $\mathcal{F}$

$$
\mathcal{F} = \int_{p_{\mathrm{crit}}}^{\infty} \langle D \rangle_\xi(p) \, \frac{\partial}{\partial r} \, F \mathrm{d}p.
$$

The total runaway density evolves as

$$
\frac{\partial \langle n_{\mathrm{RE}} \rangle}{\partial t} = \left(\frac{\partial \langle n_{\mathrm{RE}} \rangle}{\partial t} \right)_{\mathrm{fluid}} + \frac{1}{V'} \frac{\partial}{\partial r} \left[V' \mathcal{F} \right], \tag{5.21}
$$

where $(\cdot)_{\mathrm{fluid}}$ contains all the model RE generation mechanisms that are described in section 3.7. Equation (5.21) corresponds to equation (3.17) without the advection terms. While the ASCOT code calculates advection as well it is neglected for the DREAM simulation.

The diffusion coefficients D for the REs are now only radially varying and kept constant in time for the entire simulation. This represents an upper limit on the effect of the transport, as the magnetic perturbation amplitudes would decay over time in the experiment. An amplitude scan for the diffusion is conducted, with $D \times [d_{1000}, d_{10}, x_1, x_3, x_{10}] = [1/1000, 1/10, 1, 3, 10]$ scaled, where x_1 is the non-scaled, baseline scenario.

---

[2] Note that b is not the radius of the first wall, but rather that of the closest toroidally closed conducting structural element.

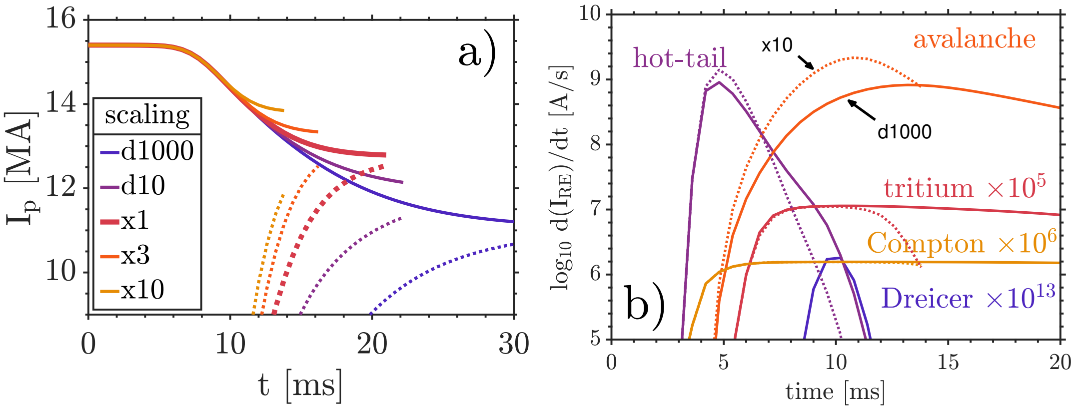

Figure 5.14: DREAM simulation of an ITER plasma disruption (at $t = 0$), that is under the influence of alpha-driven TAEs and the RE transport that the TAEs cause. The diffusive transport strength is uniformly scaled up (x) by factors 3 and 10, and scaled down (d) by factors of 10 and 1000, while *x1* is the baseline scenario. a) Evolution of the total plasma current I_p (solid) and the total runaway current I_{RE} (dotted). b) RE generation rates $\mathrm{d}(I_{\mathrm{RE}})/\mathrm{d}t$ of individual generation mechanisms for up-scaled transport (*x10*, dashed) and down-scaled transport (*d1000*, solid). Note that the up-scaled simulation does not extent all the way until full conversion, details see text.

DREAM outputs a runaway rate $\Gamma \equiv \mathrm{d}(\langle n_{\mathrm{RE}} \rangle)/\mathrm{d}t$ for every generation mechanism individually, from which we obtain the individual runaway current density rate $\mathrm{d}(j_{\mathrm{RE}})/\mathrm{d}t = \Gamma ec$. At each flux surface, j_{RE} can be integrated into the runaway current rate $\mathrm{d}(I_{\mathrm{RE}})/\mathrm{d}t$ of the entire device via

$$\frac{\mathrm{d}I_{\mathrm{RE}}}{\mathrm{d}t} = \frac{1}{2\pi} \int_0^a \mathrm{d}r \; V' \left\langle \frac{R_0^2}{R^2} \right\rangle \frac{G_{R0}}{B_{\min}} \frac{\mathrm{d}j_{\mathrm{RE}}}{\mathrm{d}t}, \tag{5.22}$$

where $\langle \cdot \rangle$ denotes a flux-average value, R is the major radius at any given point, $G_{R0} \equiv (R/R_0)B_\zeta$, where B_ζ is the toroidal magnetic field and $B_{\min}$ is the minimum magnetic field strength on the corresponding flux surface. With the same formula on Ohmic current density j_Ω, the Ohmic plasma current I_Ω is calculated by DREAM.

Figure 5.14a) shows the evolution of the total plasma current ($I_p = I_\Omega + I_{\mathrm{RE}}$, solid) and the total runaway current (I_{RE}, dashed) for the scaled transport simulations. It is observed in the simulations that increasing the RE-transport leads to a higher and faster conversion[3] of Ohmic current into runaway current.

For an explanation of the result, we will closely compare the increased transport case (*x10*) with the reduced transport case (*d1000*), which is essentially unperturbed. Depicted in figure 5.14b) are the individual runaway current rates $\mathrm{d}(I_{\mathrm{RE}})/\mathrm{d}t$ of every generation mechanism as a function of time. Note the logarithmic scale on the y-axis and the different time-scales of RE current conversion (figure 5.14a)). Hot-tail and avalanche are dominating over the other processes that are generally many orders of magnitudes weaker. Both dominant runaway processes increase by transport. Tritium decay of the high-transport case eventually drops below the low-transport simulation levels: In the beta-decay process of the tritium, a photon with an energy of 18.6 keV is released and

---

[3] The simulation data may end before a full conversion, because of a local electric field sign change, that cannot be handled in the fluid DREAM simulations and is not solved by increasing resolution parameters.

is able to generate a RE seed particle when the photon energy is enough to push a thermal electron beyond the critical momentum p_{crit} (eq. 2.19) for RE generation. This critical momentum scales with the electric field as $p_{\mathrm{crit}} \propto (E/E_c)^{-1/2}$, which is affected by the transport in a way (discussed below), that (locally) raises the critical momentum beyond what can be reached by a thermal electron hit by a tritium decay photon.

The mechanism that is most significantly altered by the RE transport is the avalanche generation. In order to understand this, we take a closer look at the runaway current density $j_{\mathrm{RE}} \propto \langle n_{\mathrm{RE}} \rangle$, which in for $t \lesssim 5\,\mathrm{ms}$ is a good approximation for the RE seed population, that will be multiplied by the avalanche (see figure 5.14b)). In figure 5.15a) we can see the REs being distributed by the perturbations in the thermal quench. While these perturbations - hence diffusion - do not extend all the way towards $r = 0$ (see figure 5.13), a significant portion of the core-localized seed electrons is transported towards $r \approx 1\,\mathrm{m}$, the half-plane of the plasma. This has crucial implications: As illustrated in figure 5.15b), the runaway electron seed has been dragged into regions of generally stronger electric field fractions E/E_c, which is a defining factor for the avalanche mechanism and increases the multiplication. As time progresses, the diffusion that is held constant for the simulation, keeps distributing runaway electrons. Meanwhile, the induced electric field grows, as seen in figure 5.15b), and is increasing towards the edge of the plasma.

We can also see the electric field profile undergoing transport-induced changes for $t = 6.5\,\mathrm{ms}$. The *x10* case decreases E/E_c at $r \approx 1\,\mathrm{m}$ but increases it for $r \lesssim 0.5\,\mathrm{m}$. We see this happening, because the electric field induction is tied to changes of the (local) current. The high-transport case has increased $j_{\mathrm{RE}}(r \approx 1\,\mathrm{m})$, hence the local total current decay is decelerated, resulting in a weaker local electric field E. By analogy, the opposite is true, where the current density j_{RE} has decreased because of the transport.

The transport-induced spatial rearrangement was shown to broaden the runaway electron profile and pushing REs into regions that are (a) more favorable for avalanching and (b) would otherwise not be populated by RE particles. The net effect is illustrated in figure 5.15c), which depicts the avalanche source term Γ_{av} in its radial profile. Note that the time-points shown not only reflect on a time of significant avalanching, but is also within the lifetime of the energetic alpha particles (figure 5.8b)), which are (indirectly) the reason for the transport in the first place. The RE diffusion indeed reduces Γ_{av} in the plasma core, $r < 0.6\,\mathrm{m}$, but this reduction is overcompensated by an increase in Γ_{av} for $r > 0.6\,\mathrm{m}$. The consequence of the stronger avalanching shows in an increase of the runaway current conversion (figure 5.14a)).

For the unmitigated and unperturbed ITER disruption, we find (figure 5.14a), *d1000*) that roughly 70% of the original pre-disruption current is converted into runaway current by the end of the CQ. We include the effects of the alpha particles destabilizing TAEs in the TQ (section 5.3) in the form of a diffusion coefficient for the perturbation-induced transport on REs. The diffusion correlates with the spatial location of the alpha particles, and as such is most significant in the inner half of the plasma (see figure 5.13). Because of this, REs cannot become lost and the distribution of core-localized RE seed particles ultimately increases the avalanche growth. For the TAE perturbation strengths established for the worst-case disruption scenario (unmitigated, well-confining) we find that the current conversion fraction increases to an estimated 85% and a ≈ 12.5 MA RE beam. In summary, the RE mitigating effects that were hypothesised for the alpha-TAE drive (see section 1.1) may end up increasing the runaway current in the absence of further transport from mid-radius towards the edge.

We have conducted the DREAM simulation without material injection, which not only provides the strongest perturbation amplitudes, but also isolates the effect of the

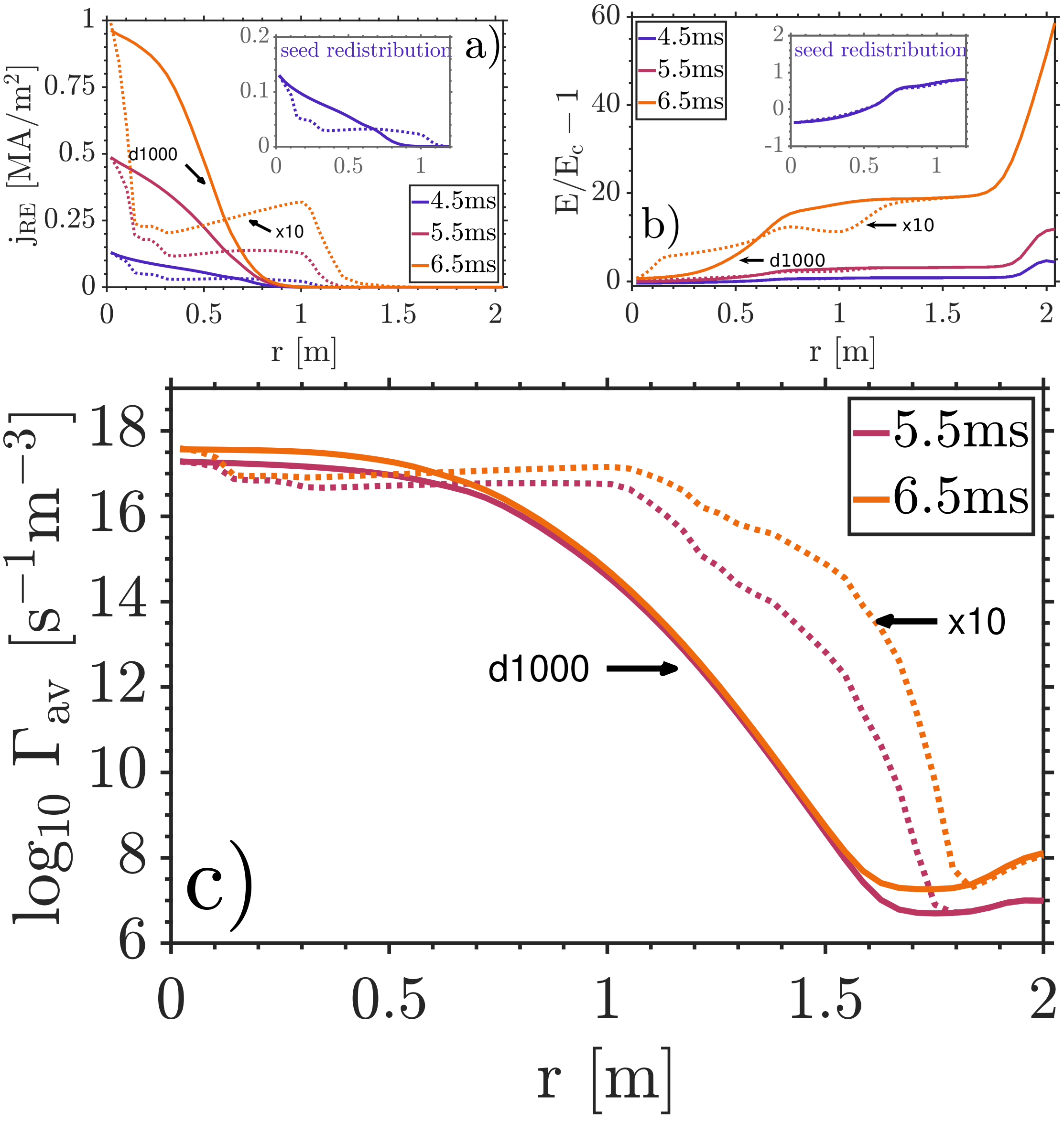

Figure 5.15: DREAM simulation of an ITER plasma disruption (at $t = 0$), that is under the influence of alpha-driven TAEs and the RE transport that the TAEs cause. Only the up-scaled RE transport (*x10*, dotted) and down-scaled RE transport (*d1000*, solid) is shown here for emphasis. Figure a) displays the runaway current density j_{RE} b) the electric field value $E/E_c - 1$ and c) the avalanche source term Γ_{av}. The time-point $t = 4.5\,\mathrm{ms}$ approximates the RE seed as it is chosen prior to RE avalanching (see figure 5.14b)) and is additionally zoomed in in a) and b) for emphasis on the seed.

TAEs on the RE generation. Considering the effects of material injection on the TAE amplitudes (see figure 5.11), a rough estimate can be made: With a reduction of average perturbation amplitude $\delta B/B$ by two orders of magnitude, the Rechester-Rosenbluth diffusion model [191] predicts the diffusion to scale down by a factor of 1000, corresponding to the *d1000* simulation conducted. The TAEs used for the unmitigated simulation have an average amplitude of $\mathrm{rms}(\delta B/B) \approx 3 \cdot 10^{-3}$, and was shown (figure 5.11) to be reduced to $\approx 10^{-5}$, for either high amounts of deuterium injection ($n_{e1} > 4n_{e0}$), alpha particle diffusion of the order of $D_\alpha = 100\,\mathrm{m}^2/\mathrm{s}$ and slow thermal quenches ($t_{\mathrm{TQ}} = 3\,\mathrm{ms}$) in various combinations. Actual predictions however are non-trivial and would require extended parameter scans and a self-consistent simulation like it has been done in this section with DREAM. For example: While the alpha particle diffusion (D_α) reduces the perturbation amplitudes by flattening its pressure gradient, it also causes the alpha particles to reach further towards the edge of the plasma. The average amplitude of the TAEs becomes lower, but modes closer to the plasma edge may become more pronounced. A transport channel for the REs that reaches the edge, may finally cause loss of runaway electrons and ultimately reduce the runaway current.

Similarly, one could think about exploiting the inherent core-transport with external efforts. In a recent study [105], mitigated ITER disruptions under the presence of magnetic perturbations have been found to have substantial effect on the RE dynamics. For the simulation study, resonant magnetic perturbations have been applied in the edge region ($0.6 < r/a < 1.0$). Depending on the mitigation scenario and perturbation amplitudes, the RMPs - in combination with various injection schemes - would sometimes increase the runaway current. The conclusion of the study was, that an effective dissipation of the runaway electrons is difficult without significant transport in the center [105]. In this context, the mechanism investigated in this work could provide synergy effects with externally applied perturbations by extending the stochastic regions from the core plasma all the way towards the edge. External perturbations methods like RMPs are planned for ITER disruption mitigation systems and could benefit strongly from the alpha-TAE drive investigated throughout this thesis.

6 Summary and outlook

Multiple post-disruption phenomena were researched in the course of this prediction study for the 15 MA ITER scenario.

In section 5.1, we reconstructed a plasma equilibrium valid for the thermal quench and investigated it about the modes supported by the system, showing a wide range of TAEs with toroidal mode numbers $n = 6 - 26$. These are calculated to receive strongly decreasing damping as the temperature decays, dropping from levels of $\gamma/\omega \approx 4\%$ down to 0.1/0.2% (for $n = 8, 9$) only $t_N = 1.5 t_{\mathrm{TQ}}$ into the thermal quench. Disruption scenarios are considered, where mitigation systems might inject various mixtures of deuterium and neon, whose inclusion generally raises the damping rate, especially for mixtures containing neon.

Section 5.2 dealt with collisional alpha particle dynamics in the thermal quench. For the initial, numerical treatment a fusion alpha source was implemented into CODION (section 4.1) and simulations on various unmitigated scenarios ($n_e = 10^{20}\,\mathrm{m}^{-3}$) conducted. A general observation was, that the alpha particles' insufficient collisional slowing-down allows them to stay energetic for several milliseconds despite strong background cooling. More specifically, the alphas thermalize after approximately $6t_N$ following the disruption, allowing for resonant interaction with TAEs in the meantime. Simulations including the self-induced electric field show that the alpha particle velocity distribution remains isotropic during the slowing-down process. This led to the creation of an analytical model for a time-dependent alpha slowing-down distribution, which was used to include the effects of MMI. We found, that raising the density of the plasma accelerates the thermalization, with the electron density playing a more significant role that the ion composition. At a post-disruption electron density of $10^{21}\,\mathrm{m}^{-3}$ the alphas thermalize at $\approx 4.5t_N$ (for $t_{\mathrm{TQ}} = 1\,\mathrm{ms}$). Whether this elevated electron density was achieved by pure deuterium injection or with the inclusion of heavier mass ions is found unimportant. Slower thermal quenches leave the alphas more time to decelerate before a certain temperature ($\sim t_N$) is reached. This is important for the alpha-TAE drive because the damping is generally a function of temperature. At quenches as slow as $t_{\mathrm{TQ}} = 5\,\mathrm{ms}$ the alphas thermalize already at $5t_N$ ($n_e = 10^{20}\,\mathrm{m}^{-3}$) and at $3.25t_N$ ($n_e = 10^{21}\,\mathrm{m}^{-3}$).

The knowledge about alpha particles and TAEs previously gained was joined in section 5.3, whose subject is wave-particle interaction simulations. For the unmitigated case, the alpha particles were shown to resonantly drive the TAEs unstable. The simulations begin at $t_N = 1.5$ due to the low damping rates calculated before. A saturation is reached after an additional $t_N = 1.5$, with average perturbation amplitudes reaching $\delta B/B \approx 10^{-3}$. For further wave-particle interaction simulations, a parameter space was created, which covers the effects of density/neon injection, thermal quench time and disruption-induced alpha particle transport. The latter is modelled with a diffusion equation at the onset of the disruption and parameterized with the diffusion coefficient D_α. The general observation was, that the unmitigated, well-confining ($D_\alpha \approx 0$) case yields the highest perturbation amplitudes. Addition of material overall decreases the TAE amplitudes, both due to an increase in background damping and due to accelerated alpha slowing-down. The diffusion of alpha particles flattens the spatial gradient, from which the energy in the resonant interaction is drawn, yielding generally lower perturbation strengths (up to an order of magnitude less for $D_\alpha = 100\,\mathrm{m}^2/\mathrm{s}$, $t_{\mathrm{TQ}} = 1\,\mathrm{ms}$). For slower thermal quenches the alphas are less energetic at $t_N = 1.5$, resulting in slightly lower average $\delta B/B$.

For section 5.4, the impact of the alpha-driven TAEs on RE transport and RE generation was calculated. It focuses on the unmitigated, well-confining disruption, which is argued to be the most relevant case for our simulation, as it is the worst-case scenario for RE generation. With a particle-following code, the RE transport is estimated with as a diffusion in the perturbed ITER equilibrium, yielding a diffusion strength of up to $D_{\mathrm{RE}} \approx 14000\,\mathrm{m}^2/\mathrm{s}$ in the inner half of the plasma. Disruption simulations were performed, taking into account the influence of variously scaled D_{RE} on generation mechanisms. The RE diffusion is found to generally increase the final runaway current, with a 15% increase in the unscaled simulation ($I_{\mathrm{RE}} \approx 13\,\mathrm{MA}$) compared to the down-scaled situation ($D_{\mathrm{RE}}/1000$, $I_{\mathrm{RE}} \approx 11\,\mathrm{MA}$). The reason is found to be the spatial rearrangement of the runaway electron seed particles, that are eventually multiplied by the avalanche mechanism. The RE seed is diffused into regions which would otherwise not been populated and are generally more favorable for avalanche, because of the electric field profile. Losses of RE particles are not invoked since the D_{RE} is most dominant in the plasma core and does not extent all the way towards the plasma edge. The reason for that is ultimately the central location of the TAE-driving alpha population.

With the ITER disruption research in this work, we have learned about an indirect interaction mechanism between fusion-born alpha particles and runaway electrons, with the mediator being TAEs. While the perturbations were found to increase the runaway electron generation, it bears an interesting opportunity for disruption mitigation systems. Systems like RMPs or passive helical coils apply externally generated perturbations in order to enhance RE transport. Both systems would benefit from the core-transport mechanisms presented in this thesis. The next logical step therefore is, to include such externally generated perturbations into our disruption simulations. In combination with the core-localized TAEs, a synergy effect in reducing the final RE current seems promising.

Bibliography

[1] J. Wesson et al. *Tokamaks.* International series of monographs on physics. Clarendon Press (2004).

[2] M. Shimada et al. Nuclear Fusion, **47** (6):S1 (2007).

[3] *ITER tokamak official website.* `https://www.iter.org/`. Accessed: 2022-10-19.

[4] A. H. Boozer. Nuclear Fusion, **58** (3):036006 (2018).

[5] B. N. Breizman et al. Nuclear Fusion, **59** (8):083001 (2019).

[6] A. H. Boozer. Physics of Plasmas, **19** (5):058101 (2012).

[7] E. Strait et al. Nuclear Fusion, **59** (11):112012 (2019).

[8] M. Lehnen et al. Journal of Nuclear Materials, **463**:39 (2015).

[9] P. Svensson et al. Journal of Plasma Physics, **87** (2):905870207 (2021).

[10] O. Vallhagen et al. Nuclear Fusion, **62** (11):112004 (2022).

[11] C. Reux et al. Nuclear Fusion, **55** (9):093013 (2015).

[12] G. F. Matthews et al. Physica Scripta, **T167**:014070 (2016).

[13] V. Kiptily et al. Nuclear Fusion, **61** (11):114006 (2021).

[14] S. Zweben et al. Nuclear Fusion, **40** (1):91 (2000).

[15] *Tokamak schematic.* `https://www.ipp.mpg.de/14869/tokamak`. Accessed: 2022-10-21.

[16] I. T. Chapman. Plasma Physics and Controlled Fusion, **53** (1):013001 (2010).

[17] K. L. Wong et al. Phys. Rev. Lett., **85**:996 (2000).

[18] A. W. Leonard. Physics of Plasmas, **21** (9):090501 (2014).

[19] A. Polevoi et al. J. Plasma Fusion Res. Series, **5**:82 (2002).

[20] H. Alfvén. Nature, **150**:405 (1942).

[21] L. D. Landau. J. Phys. (USSR), **10**:25 (1946).

[22] S. D. Pinches et al. Physics of Plasmas, **22** (2):021807 (2015).

[23] P. Helander et al. *Collisional Transport in Magnetized Plasmas.* Cambridge Monographs on Plasma Physics. Cambridge University Press (2005).

[24] H. M. Smith et al. Plasma Physics and Controlled Fusion, **51** (12):124008 (2009).

[25] A. H. Boozer. Physics of Plasmas, **22** (3):032504 (2015).

[26] E. M. Hollmann et al. Physics of Plasmas, **22** (2):021802 (2015).

[27] E. Nardon et al. Nuclear Fusion, **57** (1):016027 (2016).

[28] M. Lehnen et al. Phys. Rev. Lett., **100**:255003 (2008).

[29] K. Finken et al. Nuclear Fusion, **47** (2):91 (2007).

[30] H. M. Smith et al. Physics of Plasmas, **20** (7):072505 (2013).

[31] D. Weisberg et al. Nuclear Fusion, **61** (10):106033 (2021).

[32] V. Riccardo et al. Plasma Physics and Controlled Fusion, **52** (12):124018 (2010).

[33] G. Papp et al. Journal of Plasma Physics, **81** (5):475810503 (2015).

[34] P. Heinrich. *Investigations of Alfvénic activity during the current quench in ASDEX Upgrade*. master thesis, Technische Universität München, München (2021). `https://pure.mpg.de/rest/items/item_3332803_2/component/file_3332804/content`.

[35] H. Meyer et al. Nuclear Fusion, **59** (11):112014 (2019).

[36] U. Stroth et al. Nuclear Fusion, **62** (4):042006 (2022).

[37] L. Horvath et al. Nuclear Fusion, **56** (11):112003 (2016).

[38] P. Lauber. *Strongly non-linear energetic particle dynamics in ASDEX Upgrade scenarios with core impurity accumulation* (2018). In proceedings of the 27th IAEA Fusion Energy Conference. Available at `https://conferences.iaea.org/event/151/contributions/6094/`.

[39] P. Lauber. *NLED data and the ASDEX test case description*. `https://pwl.home.ipp.mpg.de/NLED_AUG/data.html`. Accessed: 2022-08-17.

[40] P. Lauber. *Energetic particle dynamics induced by off-axis neutral beam injection on ASDEX Upgrade, JT-60SA and ITER* (2021). In proceedings of the 28th IAEA Fusion Energy Conference. Available at `https://conferences.iaea.org/event/214/contributions/17169/`.

[41] F. Vannini et al. Physics of Plasmas, **27** (4):042501 (2020).

[42] I. Novikau et al. Physics of Plasmas, **27** (4):042512 (2020).

[43] G. Vlad et al. Nuclear Fusion, **61** (11):116026 (2021).

[44] L. Horváth et al. Nuclear Fusion, **56** (11):112003 (2016).

[45] P. Lauber. *Strongly non-linear energetic particle dynamics in ASDEX Upgrade scenarios with core impurity accumulation* (2018). In proceedings of the 27th IAEA Fusion Energy Conference. Available at `https://nucleus.iaea.org/sites/fusionportal/Shared%20Documents/FEC%202018/fec2018-preprints/preprint0319.pdf`.

[46] G. Y. Fu et al. Physics of Fluids B: Plasma Physics, **1** (10):1949 (1989).

[47] L. Zeng et al. Phys. Rev. Lett., **110**:235003 (2013).

[48] A. Lvovskiy et al. Plasma Physics and Controlled Fusion, **60** (12):124003 (2018).

[49] C. Paz-Soldan et al. Nuclear Fusion, **61** (11):116058 (2021).

[50] C. Reux et al. Plasma Physics and Controlled Fusion, **64** (3):034002 (2022).

[51] J. Mailloux et al. Nuclear Fusion, **62** (4):042026 (2022).

[52] T. Fülöp et al. Physics of Plasmas, **21** (8):080702 (2014).

[53] O. Embreus et al. Physics of Plasmas, **22** (5):052122 (2015).

[54] P. Helander et al. Phys. Rev. Lett., **89**:235002 (2002).

[55] C. Liu et al. Nuclear Fusion, **61** (3):036011 (2021).

[56] M. E. Fenstermacher et al. Nuclear Fusion, **62** (4):042024 (2022).

[57] M. Schneller et al. Plasma Physics and Controlled Fusion, **58** (1):014019 (2016).

[58] T. Fülöp et al. Physics of Plasmas, **13** (6):062506 (2006).

[59] G. Pokol et al. Plasma Physics and Controlled Fusion, **50** (4):045003 (2008).

[60] T. Fülöp et al. Physics of Plasmas, **16** (2):022502 (2009).

[61] A. Kómár et al. Journal of Physics: Conference Series, **401**:012012 (2012).

[62] A. Kómár et al. Physics of Plasmas, **20** (1):012117 (2013).

[63] G. I. Pokol et al. Physics of Plasmas, **21** (10):102503 (2014).

[64] P. Aleynikov et al. Nuclear Fusion, **55** (4):043014 (2015).

[65] C. Liu et al. Phys. Rev. Lett., **120**:265001 (2018).

[66] G. Papp et al. *Interaction of runaway populations with fast particle driven modes*. *ECA*, vol. 38F, P2.032 (2014).

[67] C. Liu et al. Nuclear Fusion, **58** (9):096030 (2018).

[68] W. W. Heidbrink et al. Plasma Physics and Controlled Fusion, **61** (1):014007 (2018).

[69] D. A. Spong et al. Phys. Rev. Lett., **120**:155002 (2018).

[70] A. Lvovskiy et al. Nuclear Fusion, **59** (12):124004 (2019).

[71] R. Yoshino et al. Nuclear Fusion, **39** (2):151 (1999).

[72] R. Gill et al. Nuclear Fusion, **42** (8):1039 (2002).

[73] T. Kudyakov et al. Nuclear Fusion, **52** (2):023025 (2012).

[74] O. Neubauer et al. Fusion Science and Technology, **47** (2005).

[75] M. Hron et al. Nuclear Fusion, **62** (4):042021 (2022).

[76] O. Ficker et al. Nuclear Fusion, **57** (7):076002 (2017).

[77] P. Helander et al. Physics of Plasmas, **7** (10):4106 (2000).

[78] A. Lier et al. Nuclear Fusion, **61** (8):086003 (2021).

[79] A. Lier et al. Submitted, Dec. 2022.

[80] L. Boltzmann. *Weitere Studien über das Wärmegleichgewicht unter Gasmolekülen*, 115–225. Vieweg+Teubner Verlag, Wiesbaden (1970).

[81] A. J. Brizard et al. Rev. Mod. Phys., **79**:421 (2007).

[82] A. D. Fokker. Annalen der Physik, **348** (5):810 (1914).

[83] M. Planck. *Über einen Satz der statistischen Dynamik und seine Erweiterung in der Quantentheorie*. Sitzungsberichte der Königlich-Preussischen Akademie der Wissenschaften zu Berlin. Reimer (1917).

[84] O. Embréus. *Kinetic modelling of runaways in plasmas.* Dissertation (2019).

[85] O. Embréus et al. New Journal of Physics, **18** (9):093023 (2016).

[86] J. D. Gaffey. Journal of Plasma Physics, **16** (2):149 (1976).

[87] A. Fasoli et al. Nuclear Fusion, **47** (6):S264 (2007).

[88] H. Brysk. Plasma Physics, **15** (7):611 (1973).

[89] D. Reiter et al. Plasma Physics and Controlled Fusion, **33** (13):1579 (1991).

[90] A. Stahl. *Momentum-space dynamics of runaway electrons in plasmas.* Dissertation (2017).

[91] A. Stahl et al. Phys. Rev. Lett., **114**:115002 (2015).

[92] J. Connor et al. Nuclear Fusion, **15** (3):415 (1975).

[93] L. Hesslow et al. Plasma Physics and Controlled Fusion, **60** (7):074010 (2018).

[94] L. Hesslow et al. Nuclear Fusion, **59** (8):084004 (2019).

[95] H. Dreicer. Phys. Rev., **115**:238 (1959).

[96] H. Dreicer. Phys. Rev., **117**:329 (1960).

[97] B. Coppi et al. Nuclear Fusion, **16** (2):309 (1976).

[98] A. Stahl et al. Journal of Physics: Conference Series, **775**:012013 (2016).

[99] L. Hesslow et al. Journal of Plasma Physics, **85**:475850601 (2019).

[100] K. Insulander Björk et al. Journal of Plasma Physics, **86** (4):855860401 (2020).

[101] R. W. Harvey et al. Physics of Plasmas, **7** (11):4590 (2000).

[102] P. Helander et al. Physics of Plasmas, **11** (12):5704 (2004).

[103] H. Smith et al. Physics of Plasmas, **12** (12):122505 (2005).

[104] H. M. Smith et al. Physics of Plasmas, **15** (7):072502 (2008).

[105] I. Svenningsson et al. Phys. Rev. Lett., **127**:035001 (2021).

[106] J. Martín-Solís et al. Nuclear Fusion, **57** (6):066025 (2017).

[107] O. Vallhagen et al. Journal of Plasma Physics, **86** (4):475860401 (2020).

[108] Y. A. Sokolov. JETP Lett. (USSR) (Engl. Transl.); (United States), **29:4** (1979).

[109] M. Rosenbluth et al. Nuclear Fusion, **37** (10):1355 (1997).

[110] O. Embréus et al. Journal of Plasma Physics, **84** (1):905840102 (2018).

[111] L. Hesslow et al. Nuclear Fusion, **59** (8):084004 (2019).

[112] H. W. Lu et al. Physica Scripta, **87** (5):055504 (2013).

[113] M. Cheon et al. Nuclear Fusion, **56** (12):126004 (2016).

[114] A. Gibson. Nature, **183** (4654):101 (1959).

[115] P. Helander et al. Phys. Rev. Lett., **90**:135004 (2003).

[116] T. Fülöp et al. Phys. Rev. Lett., **108**:225003 (2012).

[117] O. Embréus et al. Journal of Plasma Physics, **84** (5):905840506 (2018).

[118] T. Hender et al. Nuclear Fusion, **47** (6):S128 (2007).

[119] J. P. Freidberg. *Plasma Physics and Fusion Energy.* Cambridge University Press (2007).

[120] L. R. Baylor et al. IEEE Transactions on Plasma Science, **44** (9):1489 (2016).

[121] L. Baylor et al. Nuclear Fusion, **61** (10):106001 (2021).

[122] R. Raman et al. Nuclear Fusion, **60** (3):036014 (2020).

[123] G. Papp et al. Nuclear Fusion, **51** (4):043004 (2011).

[124] G. Papp et al. Plasma Physics and Controlled Fusion, **54**:125008 (2012).

[125] Y. Liu et al. Nuclear Fusion, **62** (6):066026 (2022).

[126] R. Tinguely et al. Nuclear Fusion, **61** (12):124003 (2021).

[127] V. Izzo et al. Nuclear Fusion, **62** (9):096029 (2022).

[128] T. Hayward-Schneider. *Global nonlinear fully gyrokinetic and hybrid treatments of Alfvénic instabilities in ITER.* Dissertation, Technische Universität München, München (2020).

[129] W. W. Heidbrink. Physics of Plasmas, **15** (5):055501 (2008).

[130] P. Lauber. Physics Reports, **533** (2):33 (2013).

[131] J. Tataronis et al. Zeitschrift fur Physik, **261** (3):203 (1973).

[132] C. Cheng et al. Annals of Physics, **161** (1):21 (1985).

[133] C. Z. Cheng et al. The Physics of Fluids, **29** (11):3695 (1986).

[134] S. Pinches. *Nonlinear Interaction of Fast Particles with Alfvén Waves in Tokamaks.* Dissertation (1996).

[135] L. Chen et al. Nuclear Fusion, **28** (3):389 (1988).

[136] A. B. Mikhailovskii. Journal of Experimental and Theoretical Physics, **41** (5) (1975).

[137] M. N. Rosenbluth et al. Phys. Rev. Lett., **34**:1428 (1975).

[138] H. Duong et al. Nuclear Fusion, **33** (5):749 (1993).

[139] R. B. White et al. Physics of Plasmas, **2** (8):2871 (1995).

[140] J. Candy. Plasma Physics and Controlled Fusion, **38** (6):795 (1996).

[141] N. N. Gorelenkov et al. Physica Scripta, **45** (2):163 (1992).

[142] R. R. Mett et al. Physics of Fluids B: Plasma Physics, **4** (9):2885 (1992).

[143] G. Huijsmans. *External Resistive Modes in Tokamaks.* Dissertation, Utrecht (1991).

[144] H. Lütjens et al. Computer Physics Communications, **97** (3):219 (1996).

[145] O. Embreus. *Ion runaway in magnetized plasmas.* master thesis, Chalmers University, Gothemburg (2014). `https://ft.nephy.chalmers.se/files/publications/5dc817a40945b.pdf`.

[146] T. Fehér et al. Plasma Physics and Controlled Fusion, **53** (3):035014 (2011).

[147] G. Papp et al. Nuclear Fusion, **53** (12):123017 (2013).

[148] H. Smith et al. Physics of Plasmas, **13** (10):102502 (2006).

[149] S. Hirshman et al. Computer Physics Communications, **43** (1):143 (1986).

[150] S. P. Hirshman et al. The Physics of Fluids, **26** (12):3553 (1983).

[151] P. Lauber et al. Journal of Computational Physics, **226** (1):447 (2007).

[152] P. Lauber et al. Journal of Physics: Conference Series, **1125**:012015 (2018).

[153] H. Qin. *Gyrokinetic theory and computational methods for electromagnetic perturbations in tokamaks.* Dissertation, Princeton University, New Jersey (1998).

[154] A. Bierwage et al. Nuclear Fusion, **57** (11):116063 (2017).

[155] P. W. Lauber. *Linear gyrokinetic description of fast particle effects on the MHD stability in tokamaks.* Dissertation (2003).

[156] M. S. Schneller. *Transport of super-thermal particles and their effect on the stability of global modes in fusion plasmas.* Dissertation, Technische Universität München, München (2013).

[157] F. Imbeaux et al. Nuclear Fusion, **55**:123006 (2015).

[158] S. Pinches et al. Computer Physics Communications, **111** (1):133 (1998).

[159] R. G. Littlejohn. Journal of Plasma Physics, **29** (1):111–125 (1983).

[160] A. H. Boozer. The Physics of Fluids, **24** (11):1999 (1981).

[161] R. Grimm et al. Journal of Computational Physics, **49** (1):94 (1983).

[162] J. Varje et al. arXiv (2019). `https://arxiv.org/abs/1908.02482`.

[163] S. D. Scott et al. Journal of Plasma Physics, **86** (5):865860508 (2020).

[164] K. Särkimäki. *Modelling and understanding fast particle transport in non-axisymmetric tokamak plasmas.* Dissertation, School of Science (2019).

[165] A. H. Boozer et al. The Physics of Fluids, **24** (5):851 (1981).

[166] K. Särkimäki et al. Plasma Physics and Controlled Fusion, **58** (12):125017 (2016).

[167] K. Särkimäki et al. Nuclear Fusion, **60** (12):126050 (2020).

[168] M. Hoppe et al. Computer Physics Communications, **268**:108098 (2021).

[169] E. M. Hollmann et al. Physics of Plasmas, **28** (7):072501 (2021).

[170] R. L. Miller et al. Physics of Plasmas, **5** (4):973 (1998).

[171] L. Hesslow et al. Journal of Plasma Physics, **84** (6):905840605 (2018).

[172] A. Redl et al. Physics of Plasmas, **28** (2):022502 (2021).

[173] H. P. Summers. *The ADAS User Manual, version 2.6.* Tech. rep. (2004).

[174] D. L. Book. *NRL (Naval Research Laboratory) plasma formulary.* Tech. rep. (2018).

[175] G. Papp et al. Plasma Physics and Controlled Fusion, **53** (9):095004 (2011).

[176] G. Papp et al. Plasma Physics and Controlled Fusion, **54** (12):125008 (2012).

[177] A. Polevoi. *ITER plasma data for scenario 2 (during burn) code ASTRA and code PET*. Tech. Rep. 22KZK3, ITER Documentation System (IDM) (2002).

[178] D. Ward et al. Nuclear Fusion, **32** (7):1117 (1992).

[179] P. Lauber et al. Plasma Physics and Controlled Fusion, **51** (12):124009 (2009).

[180] A. D. Turnbull et al. Physics of Fluids B: Plasma Physics, **5** (7):2546 (1993).

[181] W. Kerner et al. Journal of Computational Physics, **142** (2):271 (1998).

[182] D. Moseev et al. Physics of Plasmas, **26** (2):020901 (2019).

[183] M. Schneller et al. Nuclear Fusion, **53** (12):123003 (2013).

[184] P. H. Diamond et al. Plasma Physics and Controlled Fusion, **47** (5):R35 (2005).

[185] O. Linder et al. Nuclear Fusion, **60** (9):096031 (2020).

[186] V. Izzo et al. Nuclear Fusion, **51** (6):063032 (2011).

[187] M. Hoelzl et al. Nuclear Fusion, **61** (6):065001 (2021).

[188] G. J. Wilkie. Journal of Plasma Physics, **84** (6):745840601 (2018).

[189] J. Decker et al. Nuclear Fusion, **62** (7):076038 (2022).

[190] M. A. Henderson et al. Physics of Plasmas, **10** (5):1796 (2003).

[191] A. B. Rechester et al. Phys. Rev. Lett., **40**:38 (1978).

[192] T. Hauff et al. The Astrophysical Journal, **711** (2):997 (2010).